Aqueous systems from first-principles: structure, dynamics and electron-transfer reactions

by

Patrick Hoi Land Sit

MPhys. in Physics, University of Oxford, UK. 2000

Submitted to the Department of Physics
in partial fulfillment of the requirements for the degree of

Doctor of Philosophy in Physics

at the

MASSACHUSETTS INSTITUTE OF TECHNOLOGY

July 2006
[September 2006]

Author .....
Department of Physics
July, 2006

Certified by .....
Nicola Marzari
Associate Professor, Department of Materials Science and Engineering
Thesis Supervisor

Accepted by .....
Thomas J. Greytak
Professor of Physics
Associate Department Head for Education

Aqueous systems from first-principles: structure, dynamics and electron-transfer reactions

by

Patrick Hoi Land Sit

Submitted to the Department of Physics
on July, 2006, in partial fulfillment of the
requirements for the degree of
Doctor of Philosophy in Physics

Abstract

In this thesis, we show for the first time how it is possible to calculated fully from first-principles the diabatic free-energy surfaces of electron-transfer reactions. The excitation energy corresponding to the transfer of an electron at any given ionic configuration (the Marcus energy gap) is accurately assessed within ground-state density-functional theory via a novel penalty functional for oxidation-reduction reactions that appropriately acts on the electronic degrees of freedom alone. The self-interaction error intrinsic to common exchange-correlation functionals is also corrected by the same penalty functional. The diabatic free-energy surfaces are then constructed from umbrella sampling on large ensembles of configurations. As a paradigmatic case study, the self-exchange reaction between ferrous and ferric ions in water is studied in detail.

Since the solvent plays an central role in mediating the process, studying electron-transfer reactions requires us to first understand the structure and dynamics of the solvent molecules (water molecules in our case). Therefore, we have also studied the static and dynamical properties of (heavy) water at ambient conditions with extensive first-principles molecular-dynamics simulations in the canonical ensemble, with temperatures ranging between 325 K and 400 K. Density-functional theory, paired with a modern exchange-correlation functional (PBE), provides an excellent agreement for the structural properties and binding energy of the water monomer and dimer. On the other hand, contrary to a long-standing belief, the structural and dynamical properties of the bulk liquid show a clear enhancement of the local structure compared to experimental results; a distinctive transition to liquid-like diffusion occurs in the simulations only at the elevated temperature of 400 K.

The local coordination and structure of water is still a very debated matter and in collaboration with experimentalists at the European Synchrotron Radiation Facility in Grenoble, we have characterized the structure and the local environment in water with a combination of inelastic X-ray scattering and first-principles calculations, under conditions ranging from the normal state to the supercritical regime. The same temperature dependence of the Compton profile is observed in experiment and simulation. A well-defined linear correlation is identified between Compton pro-

file differences and changes in the number of hydrogen bonds per molecule, that is consistent with well-established structural models, and that confirms the prevailing picture of hydrogen bonding under normal conditions. While close to the critical point we observe a clear signature of density fluctuations, supercritical water is characterized by a sharp increase in under-coordinated clusters, with a significant number of dimers and trimers.

Last, we implemented a Hubbard U correction in our first-principles molecular dynamics to improve the hybridization between a transition metal ion and its surroundings. The implementation has been tested for ferrous and ferric ions solvation in water. The effects of the Hubbard U correction on the electron-transfer reaction is also studied.

Thesis Supervisor: Nicola Marzari
Title: Associate Professor, Department of Materials Science and Engineering

Acknowledgments

During my time at MIT, I am fortunate enough to have met so many great people from whom I have learned much and with whom I have spent many enjoyable times. First and foremost, I would like to express my deepest gratitude to my thesis advisor, Prof. Nicola Marzari, for his support and guidance throughout my research. He is the one who first introduced me to the study of water and the complexity of aqueous systems, with which I have been enchanted with ever since. Nicola has shown me how to think like a scientist and how to effectively deliver scientific messages through presentations and writing. Without his patience and enthusiasm, this research would never have been possible.

I am also grateful for having the opportunity to work with all of the exciting people in the group. I am thankful for all the help I have received throughout the years. I am happy to thank Matteo for his help on LDA+U implementation in Car-Parrinello molecular dynamics and his advice on the electron-transfer study, and Damian for all his patience in answering my naïve chemistry and computer questions. I am also grateful to Young-Su for all her help both scientific and in making our office a nice working environment, Brandon for all his help whenever English was involved, and Ismaila for always making the office a happy place to work. Also, thanks to other past and present group members, including Paolo, Nicola B., Arash, Boris, Nicholas, Nicolas, Heather, Mike, Francesca, Manu, Mikael, and Mayeul for all of their efforts in making the group an enjoyable place to work, from setting up and maintaining computer clusters to preparing food for group meetings.

Throughout my academic career, I am lucky to have met so many great teachers and researchers. My interest in ab-initio methods started when I took the exceptional class on the theory of solids given by Prof. John Joannopoulos. John is an excellent teacher who gave me a lot of help both inside and outside the classroom. Being my academic advisor, he gave me valuable advice when I was looking for a research group and agreed to become my co-supervisor in the Physics Department. Also, thanks to Prof. Patrick Lee for his guidance on a summer project during my first year. It was

a privilege for me to have the opportunity to work with him, albeit for only a brief duration. I also want to thank my collaborators, namely, Dr. Bernardo Barbiellini, Dr. Abhay Shukla and Dr. Christophe Bellin. In particular, thanks to Bernardo for all his help in the calculations of Compton profiles, and Abhay and Christophe for carrying out all the delicate experiments. I am also thankful for the teachers I met at Oxford, namely, Dr. Brooker, Dr. Sukumar and Prof. Ross. Without them, I would not have been able to come to MIT to pursue my Ph.D.

My life at MIT would not have been as enjoyable had I not been surrounded by all my fantastic friends in Boston. Every moment-from spending evenings at dinner and a movie to weekend getaways was always memorable. Most importantly, I owe the deepest gratitude to my father, mother, and brother, who encouraged me to study overseas when I was offered the opportunity. They have always been my support and my shelter during ups and downs in all these years, and have provided me all the luxury of pursuing my ambitions free of any external concerns. I am deeply indebted to them. Special thanks is given to my grandma, who took care of me during my childhood. She is the one who shaped my personality and still cares for me the most.

Contents

THIS PAGE INTENTIONALLY LEFT BLANK

List of Figures

List of Tables

Chapter 1

Introduction

Electron-transfer reactions are one of the most ubiquitous processes in organic and inorganic redox reactions. They cover processes and applications as diverse as solar-energy conversion in the early steps of photosynthesis, oxidation-reduction reactions between a metallic electrode and solvated ions, and the I-V characteristics of molecular-electronics devices [1]. According to the seminal work by Marcus [2], fluctuations of the environment (solvent) are crucial in mediating the transfer of an electron from the reactants to the products. The central role played by the structure and dynamics of the solvent (water in our case) requires also an extensive first-principles characterization of water and aqueous systems.

Water, due to its abundance on the planet and its role in many chemical reactions, has been widely studied both experimentally [3, 4] and theoretically. Despite the effort devoted to this, many questions remain unanswered or controversial down to the average number of hydrogen bonds or the radial distribution functions of liquid water. The peculiar interplay of hydrogen bonding, glassy behavior, electronic structure, and of quantum-mechanical effects on the dynamics of the atomic nuclei make computer simulations challenging, and a great effort has been expended to build a comprehensive and consistent microscopic picture, and a link with observed macroscopic properties [5–22].

Computational studies based on molecular dynamics simulations have a long history in the field. Simulations using force-fields models [5–10] have been successful at

reproducing many structural and dynamical properties of liquid water. However, empirical models rely on parameters which are determined by fits to known experimental data, or occasionally to ab-initio results. Their transferability to different environments, or the ability to reproduce faithfully the microscopic characteristics of hydrogen bonding, are often in question. Due to development of novel techniques [23–25] and the ever-increasing improvement in computational power, extensive molecular-dynamics simulations from first-principles are now possible. The increased accuracy and predictive power of these simulations allow studies of many systems with excellent quantitative accuracy, which had not been feasible before.

In this thesis, we first carry out extensive studies of the structural, dynamical and electrochemical properties of water and of aqueous systems using first-principles methods. The structural properties and binding energy of the water monomer and dimer are studied in details using density-functional theory, paired with a modern exchange-correlation functional (PBE). Although there has been a long-standing belief that the structural and dynamics from first-principles molecular simulations of water at ambient conditions are in excellent agreements with experiments, this picture has recently been revised by a number of investigations [26, 27] including our own [28].

Our efforts have not been confined to studying water at ambient conditions. Due to the potential applications of water at supercritical regime (e.g. as a solvent in organic waste disposal), the microscopic properties of supercritical water are also of central interest. Despite numerous efforts, the hydrogen bonding structure of water at supercritical regime is also controversial. Neutron diffraction results have been interpreted differently: some authors [29,30] conclude that $n_{HB} \sim 0$ above the critical point whereas others conclude that n_{HB} is still sizable [31, 32]. Other experimental techniques, such as X-ray diffraction [33], infrared spectroscopy [34], or NMR [35] point to a persistence of hydrogen bonds in supercritical water (SCW).

We combine here theoretical and experimental efforts to derive a robust measure of the hydrogen bonding structures from the ground-state electronic structure of the system, not from the ionic structure as it is done in the neutron and X-ray

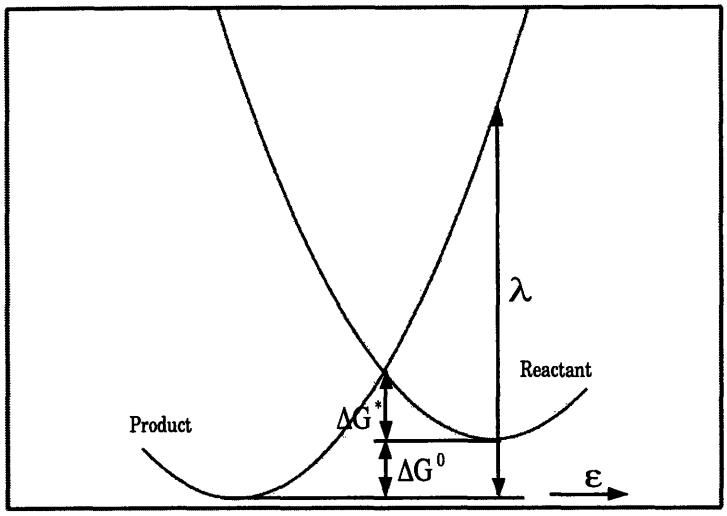

Figure 1-1: Diabatic free-energy surfaces for a typical electron-transfer reaction.

diffractions. The electronic ground state can be unambiguously accessed in X-ray inelastic (Compton) scattering experiments and straight-forwardly calculated from our first-principles methods.

With these understandings of structure and dynamics of water, we then proceed to study electron-transfer reactions in aqueous environments. The key quantities of interest are the reaction rates (or, equivalently, the conductance) and the reaction pathways. Reaction rates, in the general scenario of Marcus theory [19,36,37], have a thermodynamic contribution (the classical Franck-Condon factor, broadly related to the free energy cost of a nuclear fluctuation that makes the donor and the acceptor levels degenerate in energy), and an electronic-structure, tunneling contribution (the Landau-Zener term, related to the overlap of the initial and final states).

According to the Marcus theory of electron transfer, which we will discuss in details in Chapter 5, electron tunneling would occurs only when the system is at the crossing point of the two free energy surfaces. As indicated in Fig. 1-1, a free energy barrier of ΔG^* has to be overcome to reach the crossing point. In the limit of small

tunneling matrix element (diabatic limit), the reaction rate can be treated according to Fermi's golden rule,

$$k_{ET} = \frac{2\pi}{\hbar}|H_{DA}|^2 FC \tag{1.1}$$

where H_{DA} is the electronic coupling matrix element between the donor and the acceptor and FC is the Franck-Condon factor [36],

$$FC = \frac{exp(-(\Delta G^0 + \lambda)^2/4\lambda k_B T)}{(4\pi\lambda k_B T)^{1/2}}, \tag{1.2}$$

where λ and ΔG^0 are the reorganization energy and the free energy of reaction as indicated in Fig. 1-1. From the above equation, we can see that there are three parameters defining the electron-transfer rate in the diabatic limit, namely H_{DA}, λ and ΔG^0

There have been numerous studies of electron-transfer reactions in the context of Marcus theory. Most studies provide the correct qualitative picture but fail to describe the reactions with quantitative accuracy. This discrepancy is due to the inaccuracy of classical potentials in dealing with processes where there is a significant change in the electronic structure. In order to provide a better quantitative picture of electron-transfer reactions, we develop a novel approach to allow the study of electron-transfer reactions from first-principles molecular dynamics. Our approach involves extensive umbrella sampling of the solvent phase space and the introduction of a novel energy functional to calculate accurately both the ground and first excited state of electron-transfer reactions. With aqueous ferrous-ferric self-exchange as a paradigmatic example, we show how accurate the diabatic free energy surfaces can be obtained with excellent agreement with the experiments.

Last, in the appendix, we discuss a DFT + Hubbard U [38,39] approach targeted at correcting the over hybridization of localized orbitals that takes place at standard density-functional theory.

The thesis is organized as follows:

- Chapter 2, We describe the general computational techniques used in this research.

- Chapter 3, We present in details the simulations procedure and results of first-principles studies of water at ambient conditions.

- Chapter 4, X-ray inelastic scattering study of water at ambient and supercritical conditions are presented. We also derive a robust measure of the hydrogen bonding structure so that the average number of hydrogen bonds per molecule can be easily obtain from Compton scattering spectra of water in experiments.

- Chapter 5, We present our approach to study electron-transfer reactions from first-principles molecular dynamics. Using aqueous ferrous-ferric self-exchange as a paradigmatic example, we present the full diabatic free-energy surfaces calculations from first-principles.

- Chapter 6, The works are summarized in the conclusions.

- Appendix A, We discuss the DFT + Hubbard U studies of strongly correlated systems and its implementation in Car-Parrinello molecular dynamics. We also study the effects of the Hubbard U corrections on the ferrous and ferric ions solvation in water.

THIS PAGE INTENTIONALLY LEFT BLANK

Chapter 2

Computational techniques

2.1 Introduction

In this chapter, we will provide a brief review of the theoretical approaches and the approximations used in this research. Our work is based on the study of the properties of matters from first-principles. A calculation is said to be from first-principles if it relies on basic and established laws of nature without additional assumptions or special models. In studying the electronic properties of matters, the established law of nature is the Schroedinger's equation. Although the exact form of the Schroedinger's equation is known, getting the exact solution is almost impossible in realistic systems, due to the interactions between electrons. Many techniques have been developed to solve this equation via various approximations. Density-functional theory (DFT), which has become one of the most widely used first-principles techniques to efficiently solve the Schroedinger's equation, will be discussed in this Chapter. Although density-functional theory is, in principle, exact, in practice, its ability to describe correctly the properties depends on the accuracy of the exchange-correlation functionals used. the ability of the theory to correctly describe electronic properties of matters depends on the accuracy of the exchange-correlation functional. We will review briefly the more common approximations available.

In actual calculations, the wavefunctions have to be expanded in a basis set. One of the set most commonly used is the plane-wave basis set and we will discuss its use

and its advantages over others. The concepts of norm-conserving pseudopotentials and ultrasoft pseudopotentials to lower the computational costs in simulations will also be explained. We will then review the Car-Parrinello method, which greatly reduces the computational cost for finite temperature studies from first-principles molecular dynamics. Moreover, we will mention an extension to the technique to allow molecular dynamics at constant temperature.

2.2 Density-functional theory

In studying the electronic properties of matter, solving exactly the Schroedinger's equation is all we would need. A physical observable ($\mathcal{O}$) can be calculated from the expectation value of a corresponding operator ($\hat{\mathcal{O}}$) through the relation, $\mathcal{O} = \langle\Psi|\hat{\mathcal{O}}|\Psi\rangle$, where Ψ is the many-body eigenfunction of the Schroedinger's equation. For an isolated N-electron and M-atom system, the electronic wavefunctions can be calculated and all the physical properties can be described by the Schroedinger's equation,

$$\hat{H}(\{r_i\})\Psi(\{r_i\}) = E\Psi(\{r_i\}), \tag{2.1}$$

$$\hat{H}(\{r_i\}) = \hat{T} + \hat{V}_{ne} + \hat{V}_{ee} = \sum_i^N (-\frac{1}{2}\nabla_i^2) + \sum_i^N \sum_I^M \frac{-Z_I}{|r_i - R_I|} + \sum_{i\neq j}^N \frac{1}{r_{ij}}. \tag{2.2}$$

$\hat{H}$ is the many-body Hamiltonian and Ψ is antisymmetric due to fermion spin statistics. The ground-state wavefunction is the one that minimizes the energy and the corresponding energy is the ground-state energy. Although the above equation can, in principle, be solved exactly, the problem becomes practically unsolvable as the number of electrons increases. A very successful reformulation of the problem was introduced in 1964-65 by Hohenberg, Kohn and Sham [40,44] that provides a tractable approach to deal with the many-electron problem.

In particular, the first Hohenberg-Kohn theorem [40] states that if the ground state electronic density, $n_0(\vec{r})$, is known, the external potential acting on the electrons (i.e. the potential due to the electrostatic interaction with the ions) is also

uniquely determined, at least for the case with non-degenerate ground state. Since $n_0(\vec{r})$ also determines the number of electrons in the system, the ground state many-body wavefunction, Ψ_0 is then uniquely defined, in principle, from any given $n_0(\vec{r})$. Therefore, the total energy, besides being a functional of the ground state wavefunction, can be written as a functional of the electronic density itself. Hohenberg and Kohn then introduced,

$$F[n(\vec{r})] \equiv \langle \Psi | \hat{T} + \hat{V}_{ee} | \Psi \rangle, \tag{2.3}$$

$$E^{\nu}[n(\vec{r})] \equiv \int v(\vec{r}) n(\vec{r}) dr + F[n(\vec{r})], \tag{2.4}$$

where $F[n(\vec{r})]$, which is an universal functional independent of the external potential, contains the kinetic energy and the electron-electron interaction term, and $E^{\nu}[n(\vec{r})]$ is the total energy functional with the external potential included. In the above formula, $F[n(\vec{r})]$ is defined only with ν-representable charge densities. A density is ν-representable if it is the density associated with the antisymmetric ground-state wavefunction of the interacting Hamiltonian (Eq. 2.2) with some external potential. The second Hohenberg-Kohn theorem [40] provides a variational principle,

$$E_0 \leq E^{\nu}[\tilde{n}(\vec{r})], \tag{2.5}$$

for any trial ν-representable electronic density such that $\int \tilde{n}(\vec{r}) dr = N$.

Note that many "reasonable" densities are not ν-representable, but, as proposed by Levy [41,42] and Lieb [43], density-functional theory can be reformulated so that the electronic densities satisfy a weaker condition, of N-representability. A density is N-representable if it can be obtained from some antisymmetric wavefunction (not necessarily the ground state wavefunction in some external potential). N-representability is satisfied for any reasonable density. With the Levy-Lieb constrained-search definition,

$$F[n(\vec{r})] \equiv \min_{\Psi \to n(\vec{r})} \langle \Psi | \hat{T} + \hat{V}_{ee} | \Psi \rangle. \tag{2.6}$$

The universal functional $F[n(\vec{r})]$ is now defined for any N-representable charge den-

sity. Note that there can be many Ψ's that give the same N-representable $n(\vec{r})$ and $F[n(\vec{r})]$ is defined as the minimum expectation value of $\hat{T}+\hat{V}_{ee}$ searching over all the antisymmetric wavefunctions that integrate to $n(\vec{r})$.

The determination of the ground state is in principle greatly simplified by Eq. 2.5; instead of minimizing the energy functional with respect to the many-body wavefunction, we can now minimize the energy functional with respect to the electronic density. However, the universal functional $F[n(\vec{r})]$ is unknown in practice and this prevents any real applications. Kohn and Sham [44] provided a practical solution by introducing the concept of a noninteracting-electron reference system,

$$\hat{H}_s = \sum_i^N (-\frac{1}{2}\nabla_i^2) + \sum_i^N v_s(r_i), \tag{2.7}$$

where the potential $v_s(r_i)$ is such that the ground state density is exactly the same as the interacting system. For the noninteracting system, the exact ground state wavefunction is the Slater determinant,

$$\Psi_s = \frac{1}{\sqrt{N!}}\det[\psi_1\psi_2\ldots\psi_N], \tag{2.8}$$

where the ψ_i are the N lowest eigenstates of the noninteracting Hamiltonian. Therefore, the problem is now shifted from finding the correct $n(\vec{r})$ to finding the correct noninteracting Hamiltonian. We can rewrite the universal energy functional as,

$$F[n(\vec{r})] = T_s[n(\vec{r})] + E_H[n(\vec{r})] + E_{xc}[n(\vec{r})], \tag{2.9}$$

where

$$E_{xc}[n(\vec{r})] \equiv T[n(\vec{r})] - T_s[n(\vec{r})] + V_{ee}[n(\vec{r})] - E_H[n(\vec{r})], \tag{2.10}$$

with $T[n(\vec{r})]$ the kinetic energy of the independent electrons Hamiltonian, $E_H[n(\vec{r})]$ the Hartree energy and $E_{xc}[n(\vec{r})]$ the exchange-correlation energy that contains the difference between T and T_s (presumably fairly small), and the non-classical part of $V_{ee}[n(\vec{r})]$. Functional minimization is performed according to the Euler-Lagrange

equation,

$$\hat{H}\psi_i = \sum_j \Lambda_{ij}\psi_j, \tag{2.11}$$

where the right-hand-side comes from the orthogonality constraint on the Kohn-Sham wavefunctions and

$$\hat{H} = [(-\frac{1}{2}\nabla_i^2) + v(\vec{r}) + \int \frac{n(r')}{|r - r'|}dr' + v_{xc}(\vec{r})], \tag{2.12}$$

with the exchange-correlation potential

$$v_{xc}(\vec{r}) = \frac{\delta E_{xc}[n(\vec{r})]}{\delta n(\vec{r})}. \tag{2.13}$$

Since the potential on the electrons depends on the charge density via the Hartree and the exchange-correlation terms, the equation has to be solved self-consistently. The Kohn-Sham approach is also, in principle, exact, but still requires the knowledge of E_{xc}. Finding more and more accurate E_{xc} is an active field of research.

2.3 Functionals for exchange and correlation

The crucial quantity in the Kohn-Sham approach is the exchange-correlation energy, which is expressed as a functional of the charge density $E_{xc}[n(\vec{r})]$. As discussed in the Kohn and Sham's seminal paper [44], by explicitly separating out the independent-particle kinetic energy and the long-range Hartree terms, the remaining exchange-correlation functional $E_{xc}[n(\vec{r})]$ can be reasonably approximated as a local or nearly local functional density. They pointed out that electrons in solid can often be considered close to the limit of the homogeneous electron gas. In this limit, the effects of exchange and correlation can be treated as local in character, and therefore, the exchange-correlation functionals becomes an integral over all space with the exchange-correlation energy density at each point assumed to be the same as in a homogeneous

electron gas with that density,

$$E_{xc}^{LDA}[n(\vec{r})] = \int d^3r n(\vec{r}) \epsilon_{xc}^{hom}(n(\vec{r})). \tag{2.14}$$

This is the local density approximation (LDA). In the case of studying a magnetic system, the spin densities $n^{\uparrow}(\vec{r})$ and $n^{\downarrow}(\vec{r})$ are not equivalent at every point in the system. An extension to LDA to study magnetic systems is the local spin density approximation (LSDA) where,

$$\begin{aligned} E_{xc}^{LSDA}[n^{\uparrow}(\vec{r}), n^{\downarrow}(\vec{r})] &= \int d^3r n(\vec{r}) \epsilon_{xc}^{hom}(n^{\uparrow}(\vec{r}), n^{\downarrow}(\vec{r})) \\ &= \int d^3r n(\vec{r}) \epsilon_{x}^{hom}(n^{\uparrow}(\vec{r}), n^{\downarrow}(\vec{r})) + \epsilon_{c}^{hom}(n^{\uparrow}(\vec{r}), n^{\downarrow}(\vec{r})). \end{aligned} \tag{2.15}$$

The exchange-correlation energy density can subsequently be separated into the exchange energy and the correlation energy density. The exchange energy of the homogeneous gas is given by a simple analytical form using the Dirac exchange formula [45],

$$\epsilon_{x}^{hom}(n^{\uparrow}(\vec{r}), n^{\downarrow}(\vec{r})) = -\frac{3}{4}(\frac{6}{\pi} n^{\uparrow}(\vec{r}))^{1/3} - \frac{3}{4}(\frac{6}{\pi} n^{\downarrow}(\vec{r}))^{1/3}. \tag{2.16}$$

On the other hand, the correlation energy density has been accurately calculated for the homogeneous electron gas as a function of density using high precision using Quantum Monte Carlo techniques [46].

The first step beyond the local approximation is a functional of the magnitude of the gradient of the density $|\nabla n^{\sigma}|$ at each point. The term generalized-gradient approximation (GGA) denotes various ways to include this dependence,

$$E_{xc}^{GGA}[n^{\uparrow}(\vec{r}), n^{\downarrow}(\vec{r})] = \int d^3r n(\vec{r}) \epsilon_{xc}(n^{\uparrow}(\vec{r}), n^{\downarrow}(\vec{r}), |\nabla n^{\uparrow}(\vec{r})|, \nabla n^{\downarrow}(\vec{r})|) \tag{2.17}$$

Numerous forms for the GGA exchange-correlation functionals have been proposed, and among them, the most widely used functionals are B88 [47], PW91 [48], BLYP [49, 50] and PBE [51]. The generalized-gradient approximations show improvements over LSDA in many chemical problems, and therefore GGAs are widely adopted by the

chemistry community. However, every approximation has its limitations. Among the most serious faults is the spurious self-interaction present in most exchange-correlation functionals. In the Hartree-Fock approximation, the unphysical self-interaction term in the Hartree interaction is exactly canceled by the non-local exchange interaction. However, this cancellation is only approximate in most exchange-correlation functionals. This self-interaction effect is negligible in the homogeneous gas but large in cases with localized charge density, for example the d-electrons in transition metals. In Appendix A, we will actually look into a DFT + Hubbard U approach and discuss how it can better describe the physical properties of transition metal complexes.

2.4 Plane-wave basis set

In solving for the Kohn-Sham wavefunctions, it is necessary to expand them in a basis set. Many choices are possible, including atomic orbitals, Gaussians, linearized augmented plane wave (LAPW) and plane waves. The plane-wave basis set is most commonly used in extended systems with periodic boundary conditions. The use of a plane wave (PW) basis set has a number of advantages over other choices, including the simplicity of the basis functions, which make no assumptions regarding the form of the solution, the absence of basis set superposition error, and the ability to efficiently calculate forces on atoms. Moreover, full convergence of the forces acting on the ions with respect to the basis set is easily achieved with plane waves, and no Pulay forces arise in the dynamics, since the basis set is independent of the atomic positions.

Despite the advantages of using plane-waves, plane-waves with continuous values of the k-vector are, in principle, needed to fully represent a wavefunction. However, the use of periodic boundary conditions together with the Bloch theorem allow us to simplify the expansion. According to Bloch theorem, the wavefunctions can be written as Bloch wavefunctions,

$$\psi_{i,\vec{k}}(\vec{r}) = \sum_{\vec{G}} c_{i,\vec{k}}(\vec{G}) e^{i(\vec{k}+\vec{G})\vec{r}}. \tag{2.18}$$

In order to satisfy periodic-boundary conditions, the Bloch wavefunctions with quantum number $\vec{k}$ can be expanded in a discrete set of plane waves with k-vector $(\vec{k}+\vec{G})$, where $\vec{G}$ is the set of reciprocal lattice vectors. The set of values of k-vectors needed to represent a wavefunction now changes from continuous to discrete, but still infinite. In practice, the set of plane waves is restricted to a sphere in reciprocal space most conveniently represented in terms of a cut-off energy, E_{cut}, such that for all values of $\vec{G}$ used in the expansion,

$$\frac{\hbar^2|\vec{k}+\vec{G}|^2}{2m_e} \leq E_{cut} \tag{2.19}$$

The choice of E_{cut} depends on how structured wavefunctions are. Usually, to represent accurately the wavefunctions near the ionic cores, a large number of plane waves would be needed, making simulations very expensive computationally. The pseudopotential approximation, which we discuss in the next section, provides a solution to smooth the wavefunction around the core region and, therefore, requires a significant smaller number of plane waves.

2.5 Pseudopotential

Electrons in matter can be broadly categorized into two types - core electrons, which are strongly localized in the closed inner atomic shells, and valence electrons, which exist also outside the core. Since the potential in the region close to an atomic nucleus varies as $\frac{1}{r}$, which diverges as $r \to 0$, an extremely large number of plane waves would be needed to expand the core electron wavefunctions and the valence electrons wavefunctions around the core region. This large number of plane waves would make the computational cost extremely high.

The use of pseudopotential approximation is a way to solve this problem, by removing the core electrons and replacing the interaction between the core and the valence electrons ($\nu^{ion}(\vec{r})$) by a weaker pseudopotential with core electron screening ($\nu^{ps}(\vec{r})$) [52] (Fig. 2-1). Since most physical properties are determined by the valence electrons, this treatment is able to greatly reduce the computational cost,

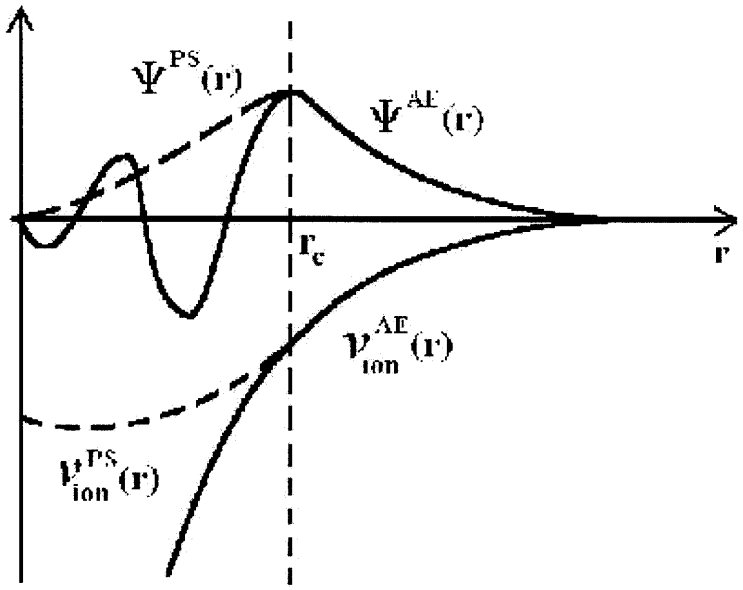

Figure 2-1: An illustration of the concept of pseudopotential approximations.

while describing physical properties with high accuracy. With this treatment, the valence pseudo-wavefunctions are smoother and nodeless in the core region and are identical to the real wavefunctions outside the core region. The computational cost in calculations using pseudopotentials is reduced in two ways. Firstly, the number of wavefunctions needed in a calculation is reduced by removing the core electrons. Secondly, the valence wavefunctions are smoother within the core region and fewer plane waves are needed to adequately describe the valence wavefunctions. To ensure that a pseudopotential calculation reproduces the same energy differences as an all-electron calculation, it is necessary for the normalized pseudo-wavefunctions to be identical to the normalized all-electron wavefunctions outside the core. This condition is called 'norm-conservation'.

2.6 Ultrasoft pseudopotential

Ultrasoft pseudopotentials, developed by Vanderbilt [53], further relax the norm-conserving constraint. With this flexibility, ultrasoft pseudopotentials attain much smoother (softer) pseudo-wavefunctions and therefore can use considerably fewer

plane waves for calculations with the same accuracy. In this scheme the total valence density $n(\vec{r})$ is partitioned into hard and soft contributions,

$$n(\vec{r}) = \sum_n [|\phi_n(\vec{r})|^2 + \sum_{ij} Q_{ij}(\vec{r}) \langle \phi_n | \beta_j \rangle \langle \beta_i | \phi_n \rangle], \tag{2.20}$$

where β_i's are projector functions that depend on the ionic positions, and the augmentation function $Q_{ij}(\vec{r})$ are given by

$$Q_{ij}(\vec{r}) = \psi_i^*(\vec{r})\psi_j(\vec{r}) - \phi_i^*(\vec{r})\phi_j(\vec{r}), \tag{2.21}$$

where $\psi_i(\vec{r})$ are the all-electron wavefunctions, and $\phi_i(\vec{r})$ are ultrasoft wavefunctions constructed without satisfying the norm-conserving condition $Q_{ij}(\vec{r}) = 0$. Also, the orthonormality condition takes on a generalized form

$$\langle \phi_i | S(\{R_I\}) | \phi_i \rangle = \delta_{ij}, \tag{2.22}$$

where $S(\{R_I\})$ depends on the ionic positions through $|\beta_i\rangle$ and is defined as,

$$S(\{R_I\}) = 1 + \sum_{ij} q_{ij} |\beta_i\rangle \langle \beta_j|, \tag{2.23}$$

with,

$$q_{ij} = \int Q_{ij}(\vec{r}) dr. \tag{2.24}$$

2.7 Car-Parrinello molecular dynamics

In performing molecular dynamics simulations, the motion of the atoms are described by the Lagrangian

$$\mathcal{L} = T - V. \tag{2.25}$$

T and V are the kinetic and potential energies of the atoms. The Newton equations of motion can be obtained by minimizing the action ($S = \int \mathcal{L} dt$),

$$\begin{aligned} \frac{d}{dt}\left(\frac{\partial \mathcal{L}}{\partial \dot{R}_I}\right) &= \frac{\partial \mathcal{L}}{\partial R_I} \\ m_I \frac{d^2 R_I}{dt^2} &= -\frac{dV}{dR_I}, \end{aligned} \tag{2.26}$$

where R_I is the position of atom I. In actual simulations, the trajectories of the atoms are obtained from the numerical integration of the equations of motion with a finite timestep δt. The forces of on atoms, i.e. the right hand side of the equation of motion, are calculated in classical molecular dynamics from classical force-fields. However, classical force-fields usually contain experimentally fitted parameters to a particular condition, and the transferability and accuracy are usually in questions. A more accurate approach to obtain forces on atoms would be to calculate them quantum-mechanically (i.e. from first-principles). In the Born-Oppenheimer approximation, the ions move on the potential energy surface of the electronic ground state $V = \langle \Psi | \hat{H} | \Psi \rangle$, where $\hat{H}$ is the Hamiltonian. The right hand side on the equations of motion now becomes

$$\begin{aligned} -\frac{dV}{dR_I} &= -\frac{d\langle \Psi | \hat{H} | \Psi \rangle}{dR_I} \\ &= -\frac{\partial \langle \Psi |}{\partial R_I} | \hat{H} | \Psi \rangle - \langle \Psi | \frac{\partial \hat{H}}{\partial R_I} | \Psi \rangle - \langle \Psi | \hat{H} | \frac{\partial \Psi}{\partial R_I} \rangle \\ &= -E \frac{\partial \langle \Psi | \Psi \rangle}{\partial R_I} - \langle \Psi | \frac{\partial \hat{H}}{\partial R_I} | \Psi \rangle \\ &= -\langle \Psi | \frac{\partial \hat{H}}{\partial R_I} | \Psi \rangle = -\langle \Psi | \frac{\partial \hat{V}}{\partial R_I} | \Psi \rangle, \end{aligned} \tag{2.27}$$

where $\hat{V}$ is the operator for the external potential acting on the electrons, which is the only R_I-dependent term in $\hat{H}$. This is the Hellmann-Feynman theorem, which makes the calculation of forces a lot simpler, since the forces on atoms can now be calculated without the computation of the derivative of the wavefunction with respect to the positions of atoms and all is needed is the analytical form of $\frac{d\hat{V}}{dR_I}$. Despite this

simplifications, the calculation of forces on atoms quantum-mechanically is still very time-consuming since it requires the computation of the ground state wavefunction at every timestep.

In 1985, Car and Parrinello [23–25] introduced a different approach to significantly lower the computational costs in performing first-principles molecular dynamics simulations. In this method, the ground state wavefunctions (i.e. the Kohn-Sham orbitals) are allowed to evolve simultaneously with the ions and the computation of the ground state wavefunctions is not needed at every timestep. The dynamics of the ions and the wavefunctions are described by the extended Lagrangian:

$$\begin{aligned} \mathcal{L}_{CP} &= \mu \sum_i f_i \int d\mathbf{r} \left| \dot{\psi}_i(\mathbf{r}) \right|^2 + \frac{1}{2} \sum_I M_I \dot{\mathbf{R}}_I^2 - E_{KS}\left[\{\psi_i\}, \{\mathbf{R}_I\}\right] \\ &+ \sum_{ij} \Lambda_{ij} \left(\int d\mathbf{r} \psi_i^*(\mathbf{r}) \psi_j(\mathbf{r}) - \delta_{ij} \right), \end{aligned} \tag{2.28}$$

where $E_{KS}[\{\psi_i\}, \{\mathbf{R}_I\}]$ is the DFT energy functional and the ψ_i are the Kohn-Sham orbitals. The equation of motions for the ions and wavefunctions are, respectively,

$$M_I \ddot{R}_I = -\frac{dE_{KS}[\{\psi_i\}, \{\mathbf{R}_I\}]}{dR_I} \tag{2.29}$$

$$\mu_i \ddot{\psi}_i = -\frac{\delta E_{KS}[\{\psi_i\}, \{\mathbf{R}_I\}]}{\delta \psi_i^*} + \sum_j \Lambda_{ij} \psi_j. \tag{2.30}$$

The Kohn-Sham orbitals are allowed to evolve as classical degrees of freedom with the inertial parameters μ_i. The Lagrange multiplier Λ_{ij} restricts the evolution of the wavefunctions to preserve the orthonormality. In performing Car-Parrinello molecular dynamics, the wavefunctions are relaxed to the ground state at a fixed set of ionic positions and then the ions are allowed to move according to the equations of motion. The electronic wavefunctions adiabatically follow the motion of the ions, with some small oscillations about the electronic ground state (Born-Oppenheimer surface). The electronic wavefunctions will have a "fictitious" kinetic energy associated with their motion and the fictitious mass μ_i. By choosing a small enough μ_i, the motion of the wavefunctions will be very fast relative to the motion of the ions and the wavefunctions

will stay very close to the instantaneous ground state.

Moreover, to ensure the wavefunctions stay close to the ground state in the course of the simulation, the ionic degrees of freedom need to be adiabatically separated from the electronic degrees of freedom so that the ionic dynamics would not heat up the "fictitious" electronic dynamics. This is achieved by ensuring that the frequency spectra of the electronic wavefunctions and the ions are well separated from one another; this condition can always be satisfied if there exists an energy gap between the occupied and unoccupied Kohn-Sham orbitals. Within a harmonic approximation, the lowest frequency of oscillation of the wavefunctions about the ground state may be written as

$$\omega_0 = \left(\frac{2(\epsilon_j - \epsilon_i)}{\mu_i} \right)^{1/2}, \tag{2.31}$$

where ϵ_i and ϵ_j are the eigenvalues of the highest occupied and the lowest unoccupied orbitals respectively. Therefore, a small enough μ_i is chosen so that ω_0 is significantly larger than the highest ionic vibrational frequency so that the exchange of energy between the ionic and the electronic degrees of freedom is practically zero. However, a small μ_i requires a small timestep to correctly integrate the equations of motion for the wavefunctions. Special care is needed to choose the value of μ_i to obtain an optimal balance between the accuracy and the speed of the simulations.

2.8 Extended Lagrangian methods for molecular dynamics in different ensembles

In the above discussion of the Car-Parrinello extended Lagrangian, the system is implicitly assumed to be in the micro-canonical (NVE) ensemble. Often, it is more convenient to fix the temperature rather than the total energy throughout the simulation. While the temperature is an intensive quantity, it is related to its extensive counterpart (kinetic energy of the ions) by

$$T = \frac{2}{3} E_{kin} N k_B = \frac{1}{3 N k_B} \sum_{i=1}^{N} \frac{p_i^2}{m_i}. \tag{2.32}$$

In this work, we adopt the integral thermostat method (or Nose-Hoover thermostat [54–57]) to control the temperature on the ions. The Nose-Hoover thermostat introduces additional degrees of freedom into the system's Hamiltonian, that becomes,

$$H = \sum_{i=1}^{N} \frac{p_i^2}{2m_i s^2} + V(r^N) + \frac{p_s^2}{2Q} + (3N+1)k_B T ln(s) \tag{2.33}$$

where s is the additional degree of freedom and T is the target temperature. The equation for the additional degree of freedom evolves together with original spatial coordinates and momenta. Physically, the Nose-Hoover thermostat acts as a heat reservoir, with which the system can exchange energy, so that temperature (i.e. the total kinetic energy of ions) fluctuates around a target value. In some systems with small HOMO-LUMO gaps that it is not practical to choose a small enough "fictitious" mass to adiabatically separate the ionic and electronic degrees of freedom, a thermostat can be applied to the electronic degrees of freedom so that the wavefunctions do not heat up and stay close to the Born-Oppenheimer surface.

Chapter 3

Static and dynamical properties of heavy water at ambient conditions from first-principles molecular dynamics

3.1 Introduction

Water, due to its abundance on the planet and its role in many of the organic and inorganic chemical processes, has been studied extensively and for decades both at the theoretical and at the experimental level [3–18,58]. In the last two decades, numerous ab-initio simulations on water have appeared [11–18], showing good agreement with experiments for the structural and dynamical data. However, this good agreement has recently been challenged by a number of investigations [26, 27] including our own [28, 59].

We have undertaken an extensive investigation of the static and dynamical properties of water, to ascertain its phase stability around ambient conditions as predicted by first-principles molecular dynamics. Particular care has been given to the statistical accuracy of the results, assuring that the time scales and length scales of the

simulations were chosen appropriately for the given conditions.

In this chapter, we will first detail all the technical aspects of our simulations. Then, we will surveys the static and vibrational properties of the water molecule and the water dimer in vacuum, at the GGA-PBE [51] density-functional level. We will also discuss the extensive liquid water simulations, performed with Car-Parrinello molecular dynamics, in the temperature range between 325 K and 400 K. Moreover, we will discuss the limitations of this approach, and some of the possible reasons to explain the remaining discrepancies with experimental results.

3.2 Technical Details

The structural and vibrational properties of the water monomer and dimer and the binding energy of the dimer have been calculated using density-functional theory in the generalized-gradient approximation and the total energy pseudopotential method, and density-functional perturbation theory [60], as implemented in PWscf of our electronic structure package [61]. We performed separate calculations using either norm-conserving pseudopotentials for both the hydrogen and the oxygen, or ultrasoft ones. These same pseudopotentials were also used for the norm-conserving or ultrasoft molecular dynamics simulations. In particular, the O Troullier-Martins norm-conserving pseudopotential [62] was generated using the FHI98PP package [63] with core radii for the s, p and d components of 1.25 a.u., 1.25 a.u., and 1.4 a.u. respectively. The Troullier-Martins hydrogen pseudopotential was generated using the Atom code [64] with a core radius for the s component of 0.8 a.u. The ultrasoft pseudopotentials were taken from the standard PWscf distribution [65]. The Kohn-Sham orbitals and charge density have been expanded in plane waves up to a kinetic energy cutoff of 25 and 200 Ry (respectively) for the ultrasoft case, and of 80 Ry and 320 Ry for the norm-conserving case. A cubic supercell of side 30 a.u. was used; interaction with periodic images is negligible [66] with this unit cell size.

Table 3.1: Structural properties of the water monomer and dimer and binding energy of the dimer, as obtained in DFT-PBE using ultrasoft or norm-conserving pseudopotentials, and compared to available experimental and theoretical results.

	PBE US (This work)	PBE NC (This work)	PBE NC (Ref [71])	Experiments (Ref. [67–70])	BLYP (Ref. [66])
$\angle_{HOH}$	104.6^0	104.2^0	104.2^0	104.5^0	104.4^0
d_{OH}(Å)	0.98	0.97	0.97	0.96	0.97
$\angle_{OHO}$	173^0	172^0	174^0	174^0	173^0
d_{OO}(Å)	2.89	2.88	2.90	2.98	2.95
E_{dimer} (kJ/mol)	-23.2	-23.8	-21.4	-22.8	-18

3.3 Water monomer and dimer: Structural and Vibrational Properties

The equilibrium structures and energetics are summarized in Table 3.1. We have included published results [66] using the BLYP functional for comparison. Both ultrasoft and norm-conserving PBE density functionals show very good agreement with experimental values. In particular, the PBE results have a dimer binding energy in closer agreement to the experiments than BLYP; the binding energy in this latter case is too weak by 4 kJ/mol, and exhibits a longer O-O distance.

Table 3.2 and 3.3 show respectively the vibrational frequencies of the water monomer and dimer in vacuum. In this calculation, a hydrogen mass of 1 a.m.u. was used (as opposed to the 2 a.m.u. mass used for the dynamical simulations of heavy water). The calculations of the vibrational frequencies were performed using density functional perturbation theory using a cubic cell of size $(30 \text{ a.u.})^3$. To achieve a convergence of a few cm^{-1} in the frequencies, cutoffs of 35 Ryd and 420 Ryd were used for wavefunctions and charge densities, respectively, in the ultrasoft case and, in the norm-conserving case, 100 Ryd and 400 Ryd were used. As shown in Table 3.2 and 3.3, the PBE functional gives intramolecular stretching modes that are in general blue-shifted compared to BLYP and experimental results. In the calculations for the dimer, the libration modes are also higher for the PBE functionals then those given

Table 3.2: Vibrational frequencies of water monomer: ν_1, ν_2 and ν_3 are the symmetric stretching, bending and asymmetric modes, respectively.

	PBE (US)	PBE (NC)	Expt [67]	BLYP [66]
$\nu_1(cm^{-1})$	3781	3704	3657	3567
$\nu_2(cm^{-1})$	1573	1599	1595	1585
$\nu_3(cm^{-1})$	3908	3816	3756	3663

Table 3.3: Vibrational frequencies of water dimer: ν_1, ν_2 and ν_3 are the symmetric stretching, bending and asymmetric stretching modes, respectively. Proton acceptor and donor molecules are denoted as (A) and (D). $\nu(Hb)$ are the two libration modes between molecules and $\nu(O-O)$ is the hydrogen-bond stretching mode.

	PBE (US)	PBE (NC)	Expt [67–70]	BLYP [66]
$\nu_1(A)(cm^{-1})$	3778	3695	3622	3577
$\nu_2(A)(cm^{-1})$	1570	1596	1600	1593
$\nu_3(A)(cm^{-1})$	3901	3804	3714	3675
$\nu_1(D)(cm^{-1})$	3601	3532	3548	3446
$\nu_2(D)(cm^{-1})$	1593	1616	1618	1616
$\nu_3(D)(cm^{-1})$	3871	3781	3698	3647
$\nu(Hb)(cm^{-1})$	666	644	520	600
$\nu(Hb)(cm^{-1})$	379	378	320	333
$\nu(O-O)(cm^{-1})$	202	196	243	214

by experiments and BLYP. We note in passing that the errors on these frequencies (especially the low energy ones) are slightly larger than usually expected from DFT. We will return to this point in a later section.

3.4 Liquid water simulations

3.4.1 Liquid water simulation at 325 K

Simulation Details

In this first simulation, we used a body-centered-cubic supercell with 32 heavy water molecules, periodic boundary conditions, and the volume corresponding to the experimental [72] density of 1.0957 g/cm^3 at 325 K. A body-centered-cubic supercell strikes

the optimal balance, for a given volume, in the distance between a molecule and its periodic neighbors, and the number of these periodic neighbors. Ultrasoft pseudopotentials were first used, as detailed in the previous section, with plane-wave kinetic energy cutoffs of 25 Ry (wavefunctions) and 200 Ry (charge densities). The deuterium mass was used in place of hydrogen to allow for a larger timestep of integration. It should be noted that for classical ions this choice does not affect thermodynamic properties such as the melting temperature (the momentum integrals for the kinetic energy factor out in the Boltzmann averages). Of course, dynamical properties such as the diffusion coefficient will be affected by our choice of heavier ions. Extensive experimental data for deuterated (heavy) water are in any case widely available.

The wavefunction fictitious mass (μ) is chosen to be 700 a.u.; this results in a factor of $\sim$14 between the average kinetic energy of the ions and that of the electrons. A timestep of 10 a.u. was used to integrate the electron and ionic equations of motions. This combined choice of parameters allows for roughly 25 ps of simulation time without a significant drift in the kinetic energy of wavefunctions and the constant of motion for the Lagrangian (2.28). Our choice of fictitious mass is consistent with the ratio $\mu/M \leq \frac{1}{3}$ for heavy water molecules suggested by Grossman et al. [26] , and assures that the physical properties are not influenced by the electronic degrees of freedom. Our initial configuration was obtained from a comparatively short 1.2 ps simulation at twice the value of the target temperature (650 K instead of 325 K); a restart with zero initial velocities was then performed at 325 K, with the temperature controlled by a single Nose-Hoover thermostat on the ions (no electronic thermostat is applied in any of the simulations).

Results

The thermostat stabilizes quickly ($\sim$1 ps) the temperature around the target value of 325 K, with the usual fluctuations due to small size of the system. However, the system is still far from equilibrium; this can be clearly observed by looking at the time evolution of the radial distribution function (RDF) and mean square displacements (MSDs). We plot in Fig. 3-1 the MSDs of the oxygen atoms as a function of

time. For the first 10 ps, the water molecules diffuse with a velocity comparable with experimental data; after 10 ps, a sharp drop in diffusivity is observed, accompanied by a distinctive sharpening of the features in the oxygen-oxygen radial distribution function (see Fig. 3-2). The radial distribution functions was calculated from the infinite bulk system by repeating the unit cell in all directions. This means that molecules up to 5.5 Å in a 32-molecule cell are inequivalent. As we move beyond this cutoff distance, the radial distribution functions will include both molecules that are inequivalent, and some that are equivalent. The statistical accuracy is going to be gradually, but slowly, affected. In this graph, and most of the latter figures, we plot radial distribution functions only up to 5.5 Å(but see e.g. Fig. 10 for a discussion of the finite-size effects).

The potential energy for the dynamics (Fig. 3-1) also drifts downward in these first 10 ps, and stabilizes afterward. We calculated the self-diffusion coefficient (D_{self}) from the Einstein relation (in 3 dimensions):

$$6D_{self} = \lim_{t\to\infty} \frac{d}{dt} \left\langle |\mathbf{r}_i(t) - \mathbf{r}_i(0)|^2 \right\rangle . \tag{3.1}$$

The structural and dynamical properties before and after this 10 ps mark are summarized in Table 3.4; experimental values at 298 K are included for comparison. All these observation conjure to a picture in which the system takes at least 10 ps to reach a reasonably thermalized state, in a process somewhat reminiscent of a glass transition. Although the time needed for equilibration will be dependent on the initial conditions, these preliminary result suggests that simulation times in the order of ten of picoseconds might be need to calculate well-converged thermodynamic observables.

Once the initial thermalization trajectory was discarded from our averages, we obtained a self-diffusion coefficient one order of magnitude smaller than the experimental value measured at room temperature. This result, combined with the clear over-structuring of the oxygen-oxygen radial distribution function $g_{OO}(r)$, indicates that our system has reached a "frozen" equilibrium state very different from what expected for liquid water (strictly speaking, a system with a finite and small number

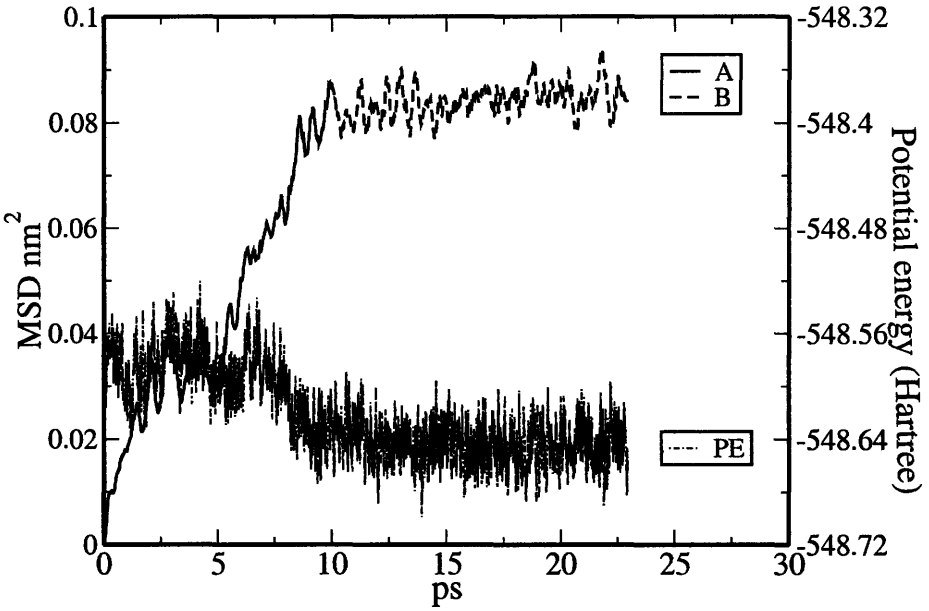

Figure 3-1: Mean square displacement and potential energy as a function of time for our first 32-water molecules simulations at 325 K. A: Diffusive region in the first stage of the simulation. B: After about 10 ps diffusivity drops abruptly.

Table 3.4: Structural and dynamical parameters before and after the 10 ps mark, compared with the experimental results at 298 K.

	$g(r)_{max}$	D (cm^2/s)
Before	2.82	1.5×10^{-5}
After	3.21	0.14×10^{-5}
Expt [4, 72]	2.75	2.0×10^{-5}

of inequivalent atoms or molecules will never undergo a phase transition).

These considerations indicates the need to assess accurately the phase stability of liquid water as obtained from first-principle molecular dynamics. At the same time, they point out the requirement of long simulation times, and a careful analysis of the technical details of the simulations.

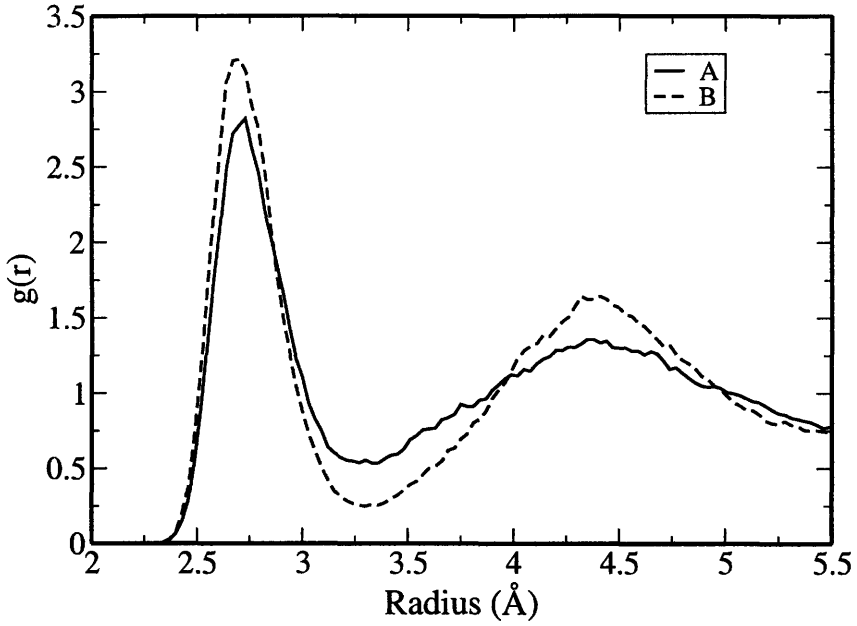

Figure 3-2: O-O radial distribution function before (A) and after (B) the equilibrium is attained.

3.4.2 Extensive water simulations in the region between 325 K and 400 K

Simulation details

In order to find out the temperature at which our system would move from a glassy to a liquid-like state, we decided to perform a series of extensive simulations at increasing temperature, from 325 K to 400 K. We first performed $\approx$ 25 ps simulations at 325 K, 350 K, 375 K and 400 K, using μ=700 a.u. and δt=10 a.u. . We used at every temperature the experimental densities [72], with the caveat that the 400 K value was obtained by extrapolation. 25 ps is approximately the maximum time allowed for a simulation with these parameters before the drift in the kinetic energy of the wavefunctions becomes apparent. We thus used these simulations as efficient "thermalization" runs, to be followed by production runs that will be described below. It is interesting to monitor during these thermalization runs the evolution of the MSDs;

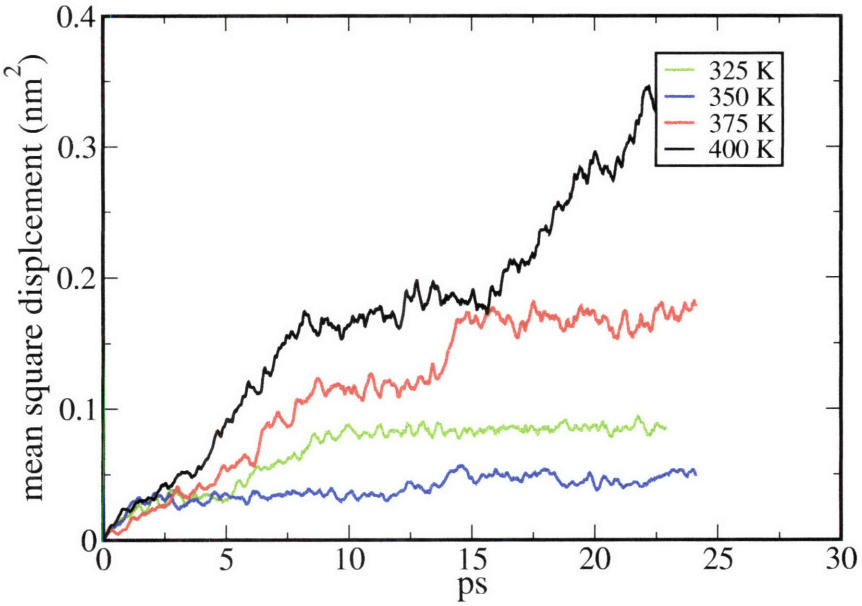

Figure 3-3: Mean square displacements as a function of time of our initial equilibration runs for 32 water molecules at 325, 350, 375 and 400 K.

these are shown for all four temperatures in Fig. 3-3. An abrupt drop in diffusivity is observed for all cases but one (predictably, the one at the highest temperature of 400 K). The onset of this drop in diffusivity varies, but broadly speaking is again of the order of 10 ps.

With these trajectories, now well thermalized in configuration space, we started our four production runs at 325 K, 350 K, 375 K and 400 K, and each of them starting from the last ionic configurations of the previous simulation at the corresponding temperature, but with zero ionic velocities. These four runs, lasting between 20 ps and 37 ps, were performed using μ=450 a.u. and δt=7 a.u. This choice of mass and timestep allows for an excellent conservation of the constant of motion, and negligible drift in the fictitious kinetic energy of the electrons, for the simulation times considered. The ratio between the kinetic energy of the ions and that of the electrons was $\approx$ 22 for the whole production time. Although a small enough fictitious mass decouples the electronic and ionic degrees of freedom, Tangney *et. al.* [73] pointed out that there

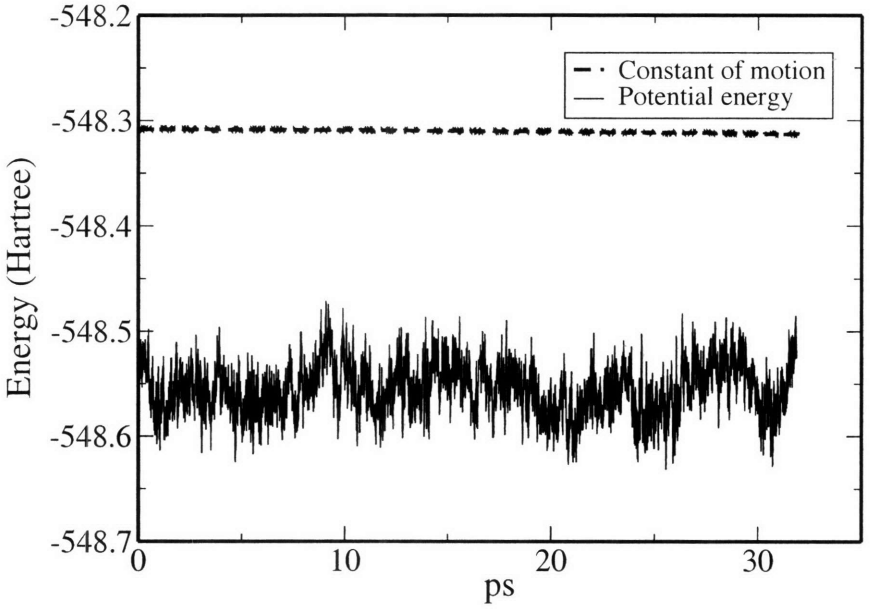

Figure 3-4: Potential energy and constant of motion in a production run at 400 K.

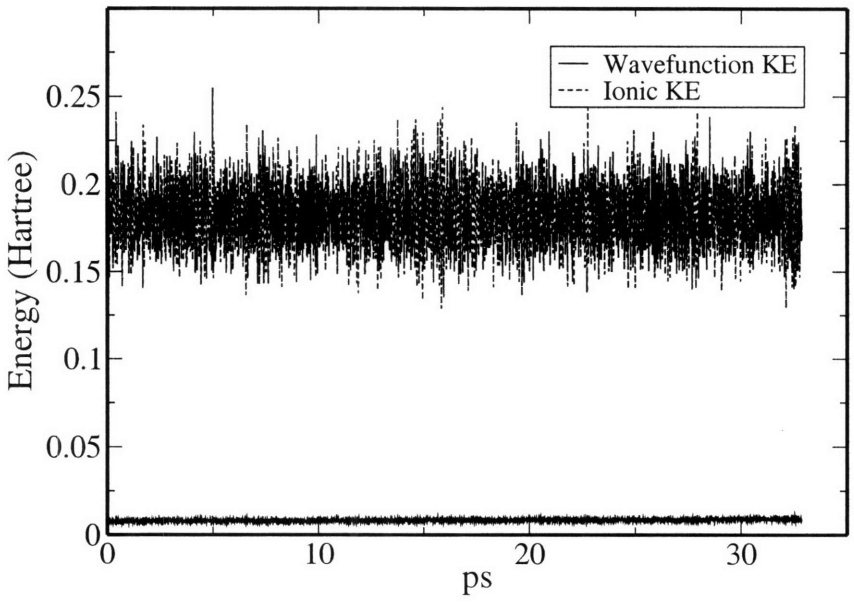

Figure 3-5: Kinetic energy of the ions and the electrons in a production run at 400 K.

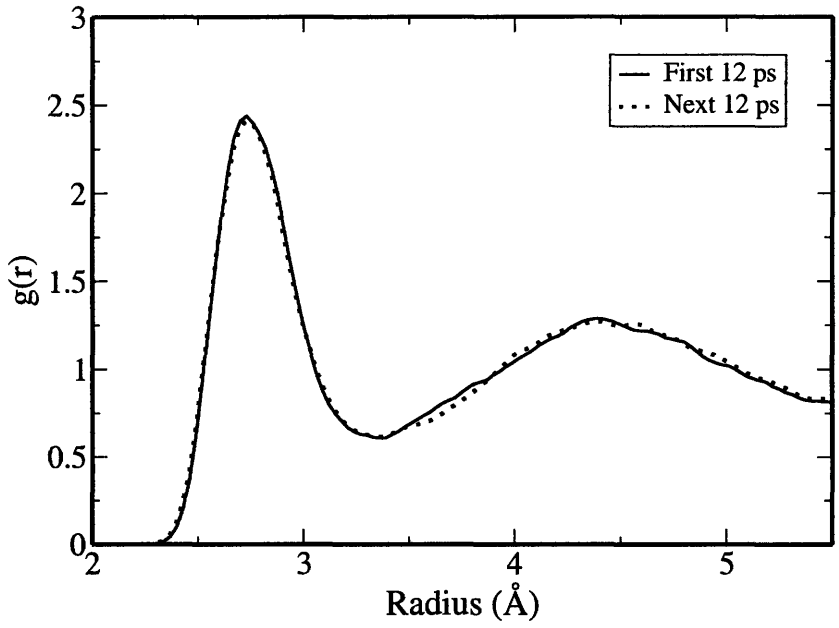

Figure 3-6: O-O radial distribution functions calculated from the first and the next 12 ps of the simulation at 400 K.

is a fictitious mass dependent error that is not averaged in the time scale of ionic motions. Schwegler *et. al.* [71] studied this effect comparing closely Car-Parrinello and Born-Oppenheimer simulations finding a larger self-diffusion coefficient in the Car-Parrinello simulation. However, the structural and thermodynamical properties were not affected.

We show in Figs. 3-4 and 3-5 the case of the 400 K simulation; we stress that no periodic quenching of the electrons was needed, and the simulations were single uninterrupted runs. Since the initial configurations were already at equilibrium at their respective temperature, and thermalization in momentum space is fast, we found that "production time" can start early in the simulations. We discarded from each trajectory the initial 1.2 ps that were needed to allow the ions to reach their target kinetic energy. As a measure of the good thermalization reached in the simulations, we show in Fig. 3-6 the O-O radial distribution function obtained from the first 12 ps of our 400 K trajectory, and the following 12 ps.

Table 3.5: Details of the production runs.

Pseudo-potentials	T(K)	Density (g/cm^3)	μ (a.u.)	δt (a.u.)	Production time (ps)
US	325	1.0957	450	7	37.6
NC	325	1.0957	300	5	22.1
US	350	1.0815	450	7	22.9
US	375	1.0635	450	7	21.1
US	400	1.0554	450	7	32.5
NC	400	1.0554	300	5	20.2

To rule out any spurious effect in our simulations coming from the use of pseudopotentials, or an extended Lagrangian, we also performed two simulations using norm-conserving pseudopotentials (as described in Section 3.2). These require larger plane-wave basis sets (80 Ry for the wavefunctions and 320 Ry charge densities, corresponding to 40000 plane waves vs 7000 for the ultrasoft case), and discrepancies, if any, with the ultrasoft calculation will provide an approximate estimate of the effects of the pseudopotential approximation and of the dynamics of the fictitious degrees of freedom. For the runs involving these norm-conserving pseudopotentials, we used μ =300 a.u. and δt=5 a.u [74]. These parameters results in a factor of $\sim$ 13 between the kinetic energy of the ions and that of the electrons. Details of all these simulations are shown in Table 3.5.

Results

The oxygen-oxygen and oxygen-deuterium radial distribution functions for the different conditions considered in this work are shown in Fig. 3-7 and Fig. 3-8 respectively. We find that at temperatures of 375 K and below both g_{OO} and g_{OH} show considerably more structure than found experimentally at 300 K. For this range of temperatures the height of the first peak of $g_{OO}(r)$ is roughly between 3.2 and 3.4, and significantly larger than the experimental value of 2.75 (also measured at 300 K). However, when the temperature in our simulations is increased to 400 K, a distinct drop of the first peak to $\sim$ 2.5 is observed, the radial distribution function $g_{OO}(r)$ and $g_{OH}(r)$ show a sharp change in their structure, and the water molecules start diffusing much faster,

as reflected in the MSDs curves for the oxygen atoms shown in Fig. 3-9. To provide cleaner statistics, the MSDs curves shown have been calculated as an average over individual MSDs curves, each obtained from our trajectory by shifting - for each individual MSDs curve - the starting configuration by 0.017 ps (in this way, a 17 ps trajectory would provide 1000 progressively shorter MSDs curves that are then averaged). The self-diffusion coefficient D_{self} is calculated from the slope of the respective MSDs curve in the range of 1 to 20 ps using Einstein's relation (3.1). Negligible differences are observed between simulations performed with ultrasoft or norm-conserving pseudopotentials, ruling out any role of the pseudopotential details in this observed result.

The structural and dynamical results are summarized in Table 3.6. As seen in this table, there is an eight-fold increase in D_{self} when increasing the temperature from 375 K to 400 K. Price *et. al.* [75] reported the experimental self-diffusion coefficient of supercooled heavy water at different of temperatures. At 276.4 K, which is just below the freezing temperature of heavy water (277.0 K), the experimental value for D_{self} is $0.902 \times 10^{-5} cm^2/s$. D_{self} for our simulations at 325 K, 350 K and 375 K is 0.16, 0.25 and 0.26 $\times 10^{-5} cm^2/s$, respectively. These numbers are significantly smaller then the experimental value below the freezing point. On the other hand, D_{self} at 400 K in our simulations is comparable to the experimental value at 300 K. These observations suggest that the theoretical freezing point for water at the DFT-PBE level is between 375 K and 400 K, and water below 375 K is in a glassy/supercooled state.

The hydrogen-bond structure can be studied calculating the number of hydrogen bonds per molecule: we identify a hydrogen bond is identified when two oxygen atoms are closer than 3.5 Å and the $\angle_{OHO}$ angle is greater than 140 ^{o} (consistently with Ref [76], and at slight variance with Ref [77]). The results are shown in the last column of Table 3.6. Between the temperatures of 325 K and 375 K there are only small changes in the number of hydrogen bonds in the system, going from 3.86 per molecule to 3.72 per molecule. An abrupt decrease to 3.37-3.45 bonds occurs when the temperature increases from 375 K to 400 K. The experimental value of 3.58 at 300 K lies between our values at 375 K and 400 K, further suggesting that the freezing

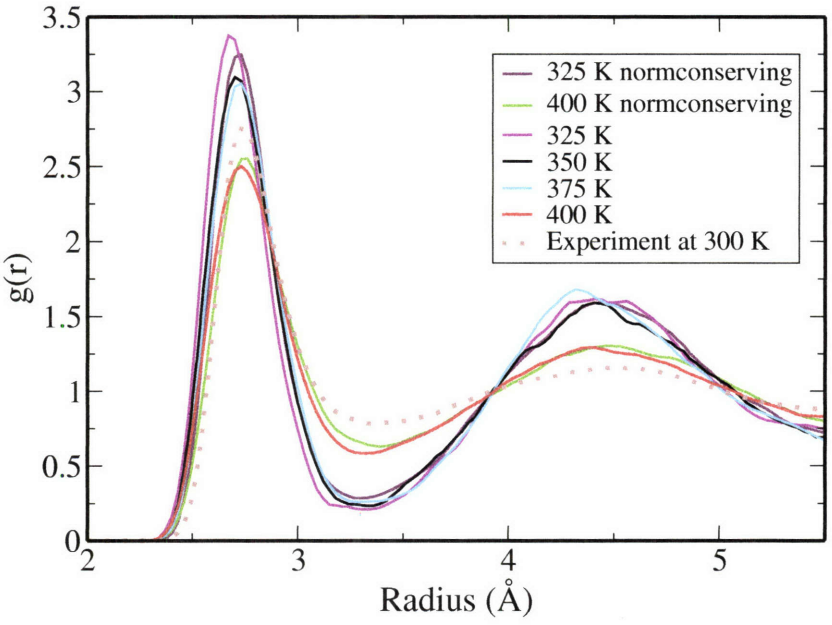

Figure 3-7: O-O radial distribution functions calculated from the production runs at 325 K, 350 K, 375 K and 400 K for ultrasoft and norm-conserving pseudopotentials. Experimental result is taken from Ref [4].

point in our simulations is between 375 K and 400 K.

In summary, we found clear liquid-like signatures in the structure and dynamics of (heavy) water, as described by DFT-PBE and Car-Parrinello MD, for temperatures reaching at least 400 K. At temperatures of 375 K and lower water is found to be in a glassy state, more structured and with much lower diffusivity. This discrepancy of more than 100 K between experimental and theoretical results is obviously relevant, given the enormous important of water in the description of systems ranging from electrochemistry to biology, and it is investigated further in the next section.

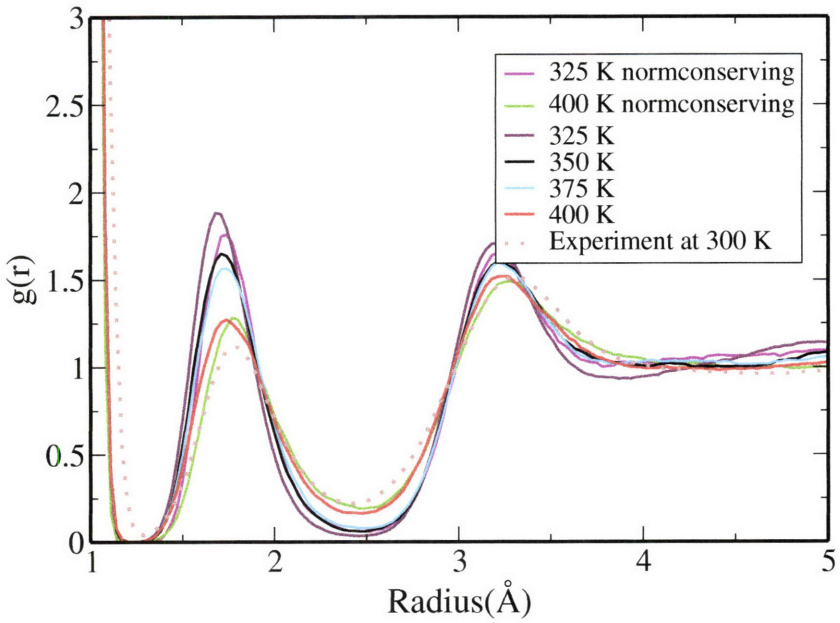

Figure 3-8: O-D radial distribution functions calculated from simulations at 325 K, 350 K, 375 K and 400 K for ultrasoft and norm-conserving pseudopotentials. Experimental result is taken from Ref [4].

Table 3.6: Summary of structural and dynamical properties of water. D_{self} is self-diffusion coefficient. g_{max} is first peak height and R[g_{max}] is location of first peak. The last column is the number of Hydrogen-bond per molecule.

	D_{self} $10^{-5}cm^2/s$	g_{max}	R[g_{max}]	no.of H-bonds per molecule
325 K (US)	0.07	3.38	2.67	3.86
325 K (NC)	0.16	3.25	2.73	3.79
350 K (US)	0.25	3.25	2.73	3.77
375 K (US)	0.26	3.10	2.71	3.72
400 K (US)	2.03	2.50	2.73	3.45
400 K (NC)	1.66	2.55	2.75	3.37
Expt [72, 78] at 300 K	1.80	2.75	2.80	3.58

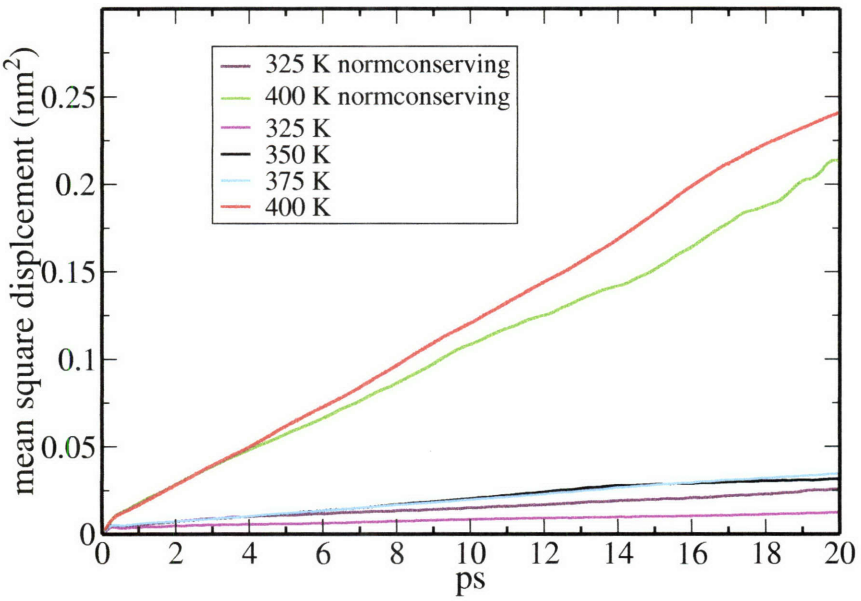

Figure 3-9: Mean square displacements calculated from simulations at 325 K, 350 K, 375 K and 400 K for ultrasoft and norm-conserving pseudopotentials.

3.5 Overestimation of the freezing temperature of water

There are several possible reasons for the overestimation of the freezing temperature of water, and several of them could play a significant role. We discuss here some of the possibilities.

3.5.1 Finite-size effects

Since our simulation cell contains only 32 water molecules, finite-size effects could obviously play a role even if periodic-boundary conditions are used. The interactions of water molecules with their periodic images could be considerable due to the long-range hydrogen-bond network. On the other hand, when zero correlations are found between a molecule and its periodic image we can safely assume that the unit cell is for all practical purposes large enough, and every molecule feels the same environment

that it would have in an infinite system. In our case, the distance between a molecule and its eight periodic images is $\sim$ 11 Å and at this distance all radial distribution functions look very flat and unstructured. In any case, to study the finite-size effects we carried out another extensive simulation (40 ps total, with 15 ps of production time following 25 ps of thermalization) for a system composed of 64 heavy water molecules at 400 K. We used the same parameters for this simulation as in the 32-molecule, 400 K ultrasoft simulation. The oxygen-oxygen radial distribution function g_{OO}(r) is shown in Fig. 3-10 for both the 32- and 64-molecule systems. As mentioned previously, the radial distribution functions was calculated by repeating the unit cell in all directions. The molecules up to 5.5 Å in the 32-molecule cell, and 6.9 Å in the 64-molecule cell are inequivalent. We indicate in the graphs with two arrows, the radii of the spheres completely inscribed by in BCC simulation cells.

Differences between 32- and 64-molecule systems are negligible, and within the variance for simulations of the order of 10-20 ps (as estimated from uncorrelated classical simulation data [26]); the 64-water simulation shows a marginally more structured $g(r)$ where the first peak height is at about 2.6 (compared to 2.5 for the 32-water case). Larger ab-initio simulations would be too demanding; for this reason, we performed two classical simulations at 300 K using the SPC force field [79] for water, and comparing the case of 64 and 1000 water molecules (each simulation lasting 1000 ps). The g_{OO}(r) calculated from these two runs are shown in Fig. 3-11, and again we do not find any significant differences between these two curves. These results help ruling out finite-size effects as the major cause of the discrepancy observed with the experimental numbers.

3.5.2 Exchange-correlation functional effects

While density-functional theory is in principle exact, any practical application requires an approximated guess to the true exchange-correlation functional. In this work, we have used the GGA-PBE approach [51]. As it was observed in Sec. III, the structural properties for the water molecule and dimer are in excellent agreement with experiments, as is the binding energy for the dimer. On the other hand, the vibra-

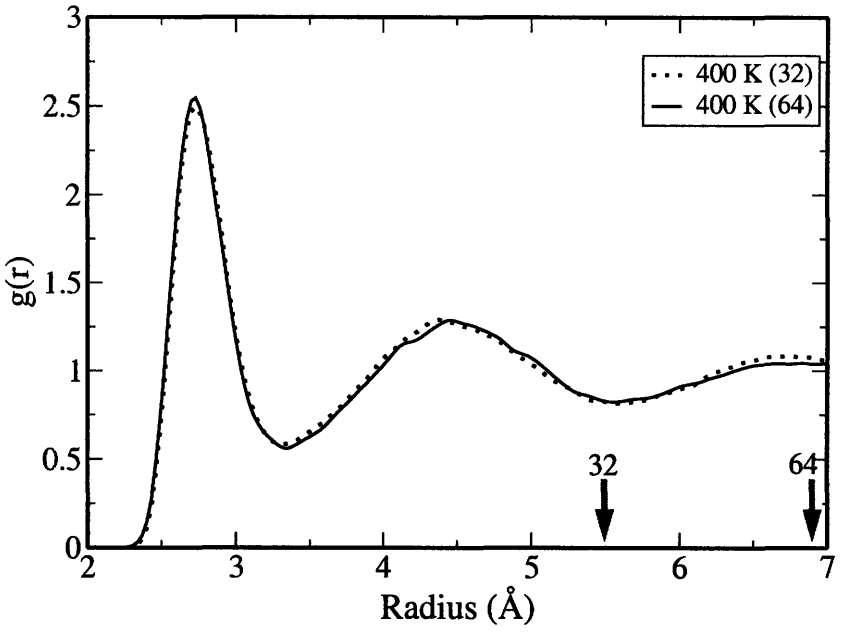

Figure 3-10: O-O radial distribution function for a Car-Parrinello simulations with 32 or 64 molecules. The arrows indicate the radius of the sphere that is completely inscribed by the BCC simulation cells with 32 or 64 molecules.

tional properties show larger discrepancies with experiments than usually expected, in particular for some of the libration modes in the dimer. This result certainly points to the need for improved functionals to describe hydrogen bonding. The dependence of the melting point on the exchange-correlation functional chosen is more subtle; below 400 K, PBE water displays solid-like oxygen-oxygen radial distribution functions that are only slightly affected by the temperature, and that are similar to those obtained with a fairly different functional such as BLYP [26]. The similarity between these radial distribution functions is just a reminder that the structural property and the geometry of the intermolecular bonds are well described by different functionals; once water is "frozen", all radial distribution functions will look similar. The temperature at which this transition takes place could be affected by the use of different functionals [80] and the magnitude of the contribution of any one of them to the melting point temperature is still open to investigation.

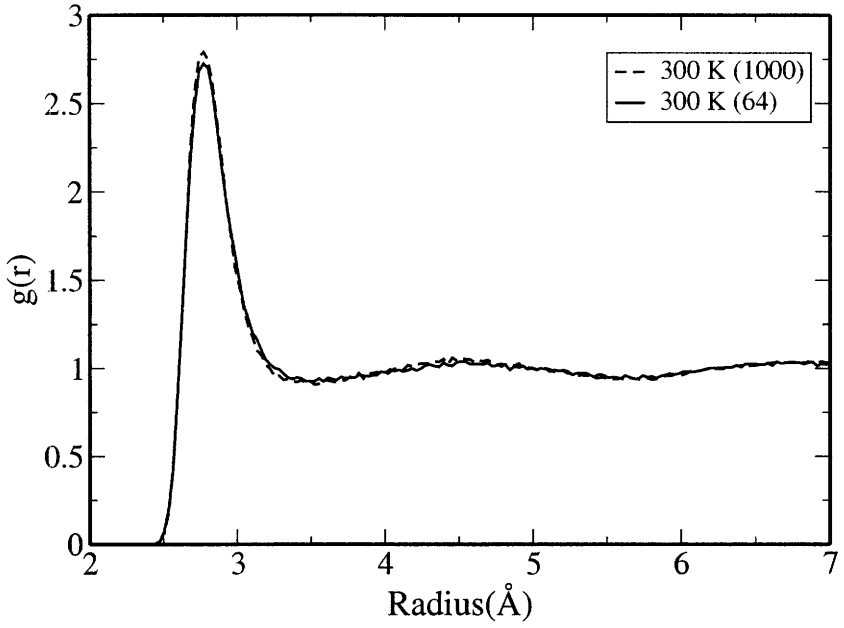

Figure 3-11: O-O radial distribution function for a classical (SPC) simulation with 64 or 1000 water molecules.

3.5.3 Quantum effects

In first-principles Car-Parrinello or Born-Oppenheimer molecular dynamics simulations the ions are most often treated as classical particles, which is a good approximation for heavy ions (path-integral simulation can describe the quantum nature of the ions [81–83], but their computational costs, when paired with a first-principles DFT descriptions of the electrons, preclude at this moment simulations with the statistical accuracy needed). However, for light ions like hydrogen or deuterium, the effects of a proper quantum statistics can be very significant; tunneling of the nuclei can also affect the dynamics [84, 85]. In the case of water, all the intramolecular vibrational modes and some of the intermolecular modes are much higher in energy compared to room temperature. We show in Fig. 3-12 the power spectrum for the deuterium atoms as calculated from the velocity-velocity correlation function of heavy water molecules for our simulations at 400 K (ultrasoft, 32 molecules). The distinctive peaks of the intramolecular stretching and bending modes are centered around

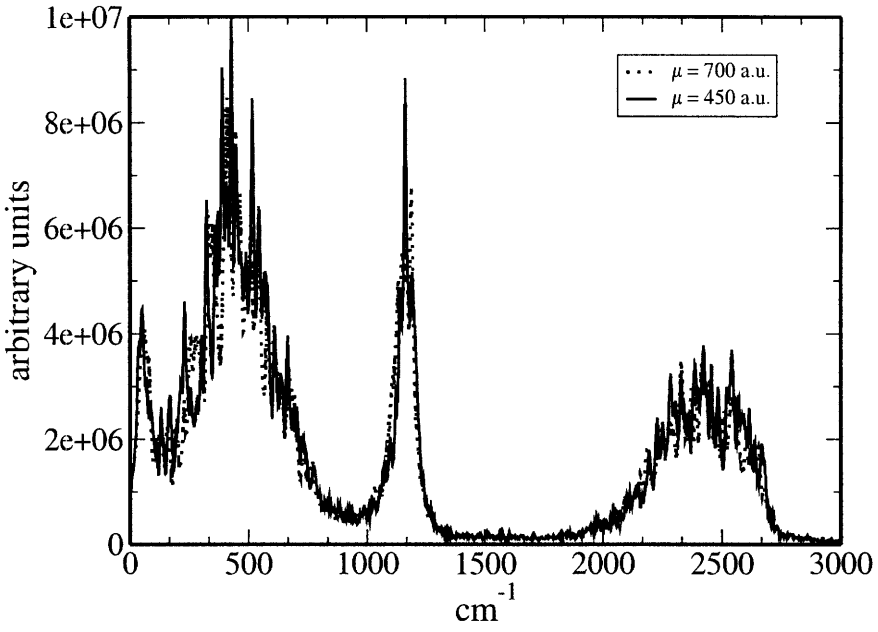

Figure 3-12: Power spectrum of deuterium atoms calculated from the velocity-velocity correlation function. For comparison, we also show the power spectrum as obtained with a larger fictitious mass of 700 a.u (dotted line) instead of 450 a.u.

2400 cm^{-1} and 1200 cm^{-1} respectively, much higher than the room temperature of $k_B T_{room} \approx 200$ cm^{-1}. The peak at 500 cm^{-1} corresponds to the intermolecular vibrational modes, also larger than $k_B T_{room}$. When ions are treated as classical particles, as in our ab-initio molecular dynamics simulations, all vibrational modes obey Boltzmann statistics. In reality, modes with frequency higher than $k_B T_{room}$ are frozen in their zero-point motion state, and their exchange of energy with the lower-frequency modes ("the environment") is suppressed - in other words their contribution to the specific heat is zero, in full analogy with the low-temperature discrepancies from the Dulong-Petit law in solids. This effect could significantly affect the dynamics of water-water interactions, and it has long been argued that treating each water molecule as a rigid body could actually provide a closer match with experimental conditions. In fact, recent ab-initio simulations [86] in which the water molecules are constrained to maintain their equilibrium intramolecular bond lengths and bond angle result in

a more diffusive and less structured description of water, that remains liquid at a temperature of 326 K. Path-integral simulation [87] for water described with classical potentials did find as well a significant difference due to the quantum effects (i.e. the freezing of the high-energy vibrational excitation), of the order of 50K.

3.6 Conclusions

We performed extensive first-principles molecular dynamics simulations of heavy water at the DFT-PBE level. Equilibration times are found to be comparatively long, and easily in excess of $\approx$ 10 ps at ambient temperature. At ambient temperature, water is found to be over-structured compared to experiments, and with a diffusivity that is one order of magnitude smaller than expected. An abrupt change in the structure and dynamics is observed when the the temperature is raised from 375 K to 400 K; even at this high temperature, where a liquid-like state is reached, water shows more structure and less diffusivity than found experimentally at room temperature. These results are broadly independent of some of the possible errors or inaccuracies involved in first-principles simulations, including in this case finite-size effects, insufficient thermalization or simulation times, or poorly designed pseudopotentials. Our simulations suggest that the freezing point is around 400 K - this discrepancy is at variance with the good agreement for the structure and energetics of the water monomer and dimer with the experimental values, and could originate in the neglect of quantum statistics for the many high-frequency vibrational modes in this system.

THIS PAGE INTENTIONALLY LEFT BLANK

Chapter 4

Compton scattering study of water at normal and supercritical conditions

4.1 Introduction

The average number of hydrogen bonds per molecule n_{HB} in liquid water has recently become a subject of controversy [88–91]. Wernet *et al.* [88] have compared the X-ray absorption spectra (XAS) of bulk ice, an ice surface and water and concluded that the liquid contains significantly more broken hydrogen bonds than previously thought; Smith *et al.* disagree with these conclusions [89–91]. Prendergast and Galli [92] have shown that established 4-fold coordination models withstand XAS data, but they also noted that the interpretation of XAS is complicated due to different final-state effects.

On the other hand, under high-temperature and high-pressure conditions, around and beyond the water critical point (647 K, 220.6 bar), the hydrogen bond network dissociates in a very rapid evolution, leading to density inhomogeneities over mesoscopic distances around the critical state and beyond. The degree of persistence of the hydrogen bonding in the region beyond the critical point has also been controversial.

Neutron diffraction results have been interpreted differently: some authors [29, 30] conclude that $n_{HB} \sim 0$ above the critical point whereas others conclude that n_{HB} is still sizeable [31, 32]. Other experimental techniques, such as X-ray diffraction [33], infrared spectroscopy [34], or NMR [35] point to a persistence of H-bonds in supercritical water (SCW).

In collaboration with Abhay Shukla and Christophe Bellin (Jussieu, Paris VI, and the the European Synchrotron Radiation Facility in Grenoble), we combined theoretical and experimental efforts to derive robust measures of hydrogen bonding, not taken from the ionic structure (as in neutron and X-ray diffractions) but from the ground-state electronic structure of the system. Compton scattering (i.e. inelastic scattering of photons by electrons) [93] is one of the few spectroscopies capable of directly probing the bulk electronic ground state in materials, through the relation that is established between the energy loss of the photon and the projection of the initial electron momentum along the scattering vector $\vec{k}$. Formation of chemical bonds by valence electrons, leading to localization in real space, can thus be detected in momentum space as a broadening of the corresponding Compton profile. This unique sensitivity to outer electrons and thus to intermolecular interactions and to chemical bonding is in contrast with X-ray diffraction, which is principally sensitive to the core-electron signal. Compton scattering has already revealed the quantum nature of the hydrogen bond in ice [94], and recent investigations [95–97] have suggested that it might be also suitable for liquid water. In this chapter, we present state-of-the-art first-principles calculations together with X-ray Compton scattering experiment [98] to provide an extremely consistent picture for n_{HB} in the normal and supercritical regimes.

4.2 What is Compton scattering?

Compton Scattering is the inelastic scattering of an X-ray photon by an electron. As shown in Fig 4-1, during this inelastic scattering process the momentum and the energy transfer from the photon to electron are $\vec{k} = \vec{p}_2 - \vec{p}_1$ and energy transfer

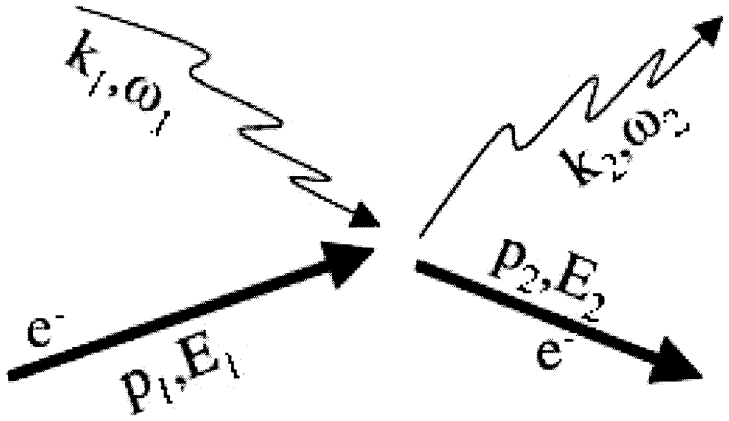

Figure 4-1: A schematic diagram of inelastic X-ray scattering by an electron: a photon with energy $\hbar\omega_1$ and momentum k_1 hits an electron with initial energy E_1 and momentum p_1. The photon is scattered away with energy $\hbar\omega_2$ and momentum k_2.

$\hbar\omega = E_2 - E_1$, respectively, where $\vec{p}_1$, E_1, and $\vec{p}_2$, E_2, are the initial- and final-state momenta and energies for the electron. The scattering cross-section can be obtained from Fermi's golden rule [99]:

$$\frac{d^2\sigma}{d\Omega d\omega_2} = \left(\frac{d\sigma}{d\Omega}\right)_T \frac{\omega_2}{\omega_1} \sum_f |\langle\psi_2|e^{i\vec{k}\cdot\vec{r}}|\psi_1\rangle|^2 \delta(E_2 - E_1 - \hbar\omega). \tag{4.1}$$

The summation is over all the possible electronic final states and $\vec{k}$ and $\hbar\omega$ are the momentum and energy transfer during the scattering process. $\left(\frac{d\sigma}{d\Omega}\right)_T = \left(\frac{e^4}{m_e^2 c^4}\right)\frac{1}{2}(1 + cos^2\phi)$ is the Thomas scattering cross-section, where ϕ is the scattering angle.

In the Compton limit [100] (assuming the electron is free after scattering) the electronic final state wavefunction ψ_2 can be expressed as a plane wave with wavevector $\vec{p}_2$, $\psi_2 \sim e^{i\frac{\vec{p}_2\cdot\vec{r}}{\hbar}}$. Then, the scattering crossing section can be written as

$$\frac{d^2\sigma}{d\Omega d\omega_2} = \left(\frac{d\sigma}{d\Omega}\right)_T \frac{\omega_2}{\omega_1} \sum_f |\langle e^{i\frac{\vec{p}_2\cdot\vec{r}}{\hbar}}|e^{i\vec{k}\cdot\vec{r}}|\psi_1\rangle|^2 \delta(E_2 - E_1 - \hbar\omega). \tag{4.2}$$

By writing the summation over final states as a $\vec{p}'$ integration, where $\vec{p}' = \vec{p}_2 - \hbar\vec{k}$,

we obtain

$$\begin{aligned}\frac{d^2\sigma}{d\Omega d\omega_2} &= \left(\frac{d\sigma}{d\Omega}\right)_T \frac{\omega_2}{\omega_1}\int d\vec{p}'|\tilde{\psi}_1(\vec{p}')|^2\delta(\frac{\hbar^2k^2}{2m}+\frac{\hbar\vec{p}'\cdot\vec{k}}{m}-\hbar\omega) \\ &= \left(\frac{d\sigma}{d\Omega}\right)_T (\frac{\omega_2}{\omega_1})(\frac{m}{\hbar k})\int d\vec{p}' n(\vec{p}')\delta(\vec{p}'\cdot\vec{k}+\frac{\hbar k^2}{2}-m\omega) \qquad (4.3)\end{aligned}$$

where $\tilde{\psi}_1(\vec{p}')$ is the initial state electronic wavefunction in momentum space and $n(\vec{p}') = |\tilde{\psi}(\vec{p}')|^2$ is the electronic momentum density. Note that the electronic momentum density, being the square of the wavefunction in the momentum space, is different from the Fourier transform of the charge density in real space defined as $n^{FT}(\vec{p}) = \int e^{i\vec{p}\vec{r}}n(\vec{r})d\vec{p}$.

Owing to the presence of a δ-function, the integral in Eq. 4.3 is taken over a plane in momentum space perpendicular to $\vec{k}$, where $p = \frac{m\omega}{k} - \frac{\hbar k}{2}$ is the distance of this plane to the origin of momentum space. The scattering spectrum can be further simplified to

$$\begin{aligned}\frac{d^2\sigma}{d\Omega d\omega_2} &= \left(\frac{d\sigma}{d\Omega}\right)_T (\frac{\omega_2}{\omega_1})(\frac{m}{\hbar k})\int d\vec{p}'|\tilde{\psi}(\vec{p}')|^2\delta(p-\vec{u}\cdot\vec{p}') \\ &\equiv \left(\frac{d\sigma}{d\Omega}\right)_T (\frac{\omega_2}{\omega_1})(\frac{m}{\hbar k})J(p,\vec{u}). \qquad (4.4)\end{aligned}$$

$J(p,\vec{u})$ is called the Compton profile and $\vec{u}$ is the unit vector in the direction of the momentum transfer $\vec{k}$. This one-electron formula can be straight forwardly extended to the multi-electron case in condensed phase, in the context e.g. of density-functional theory. The one-electron wavefunction is replaced by the set of Kohn-Sham orbitals $\{\psi_i\}$, and the momentum density is given by

$$n(\vec{p}) = \sum_m |\tilde{\psi_m}(\vec{p})|^2. \qquad (4.5)$$

In our study, we analyze the changes of the Compton profiles as state conditions for water are changed, and we relate them to changes in hydrogen bonding. With a combined compared theoretical and experimental effort, we show how the Compton profiles can be an accurate measure of hydrogen bonding in these systems.

4.3 Calculating Compton profiles in a Car-Parrinello molecular dynamics simulation

In Car-Parrinello molecular dynamics, Γ-point sampling is employed since large supercells are used. For our typical supercells, this sampling procedure is sufficiently accurate for most physical properties (e.g. energies and forces). However, because of this, $J(p)$ can only be calculated on a very coarse-grained grid in reciprocal space. The resolution is limited to $2\pi/a$, where a is the unit cell side-length. In order to improve the resolution of the calculations with experiments, we adopt here the interpolation scheme already used in Ref. [101] replacing the δ function with it exponential form $\delta(p-\vec{u}\cdot\vec{p}) = \frac{1}{2\pi}\int d\lambda e^{i\lambda(p-\vec{u}\cdot\vec{p})}$. The Compton profile now becomes

$$J(p,\vec{u}) = \frac{1}{2\pi}\int_0^\infty d\lambda e^{i\lambda p}\tilde{n}(\lambda\vec{u}), \tag{4.6}$$

where $\tilde{n}(\lambda\vec{u})$ is the Fourier transform of $n(\vec{p})$. Again, this $\tilde{n}(\lambda\vec{u})$ is different from the charge density in real space. Instead, it is the convolution of a wavefunction in real space with itself, $\tilde{n}(\lambda\vec{u}) = \sum_i \int d\vec{r}\psi_i(\vec{r})\psi_i(\lambda\vec{u}-\vec{r})$. In molecular systems, the Kohn-Sham wavefunctions are expected to be localized in real space and so are the convolutions of the wavefunctions. Utilizing the fact that $\tilde{n}(\lambda\vec{u})$ is a localized function in real space, the integration in Eq. 4.6 can be performed with a cutoff λ_c in the upper limit and a $J(p,\vec{u})$ with arbitrary q can be calculated. In this treatment, the Compton profile calculated is direction ($\vec{u}$) dependent. Considering the way the real-space grid is arranged in Car-Parrinello molecular dynamics, it is straight forward to calculate $J(p,\vec{u})$ along the x, y and z directions. In the calculations of the Compton profiles of water in this chapter, all Compton profiles are calculated by averaging the values along the special axes for better comparison with experimental data and $J(p)$'s are normalized to the number of electrons per a water molecule in the region p=[-∞,∞] in both simulations and experiments. We note in passing that since a liquid is studied, averaging over different directions would not be needed in infinitely large simulations.

4.4 Molecular contributions to the Compton profiles

Wannier functions [102] can be constructed from Kohn-Sham orbitals; in the multi-band case, the Wannier transformation is

$$W_{n,\vec{R}}(\vec{r}) = \frac{V}{(2\pi)^3} \int_{BZ} e^{-i\vec{k}\cdot\vec{R}} \sum_m U^{\vec{k}}_{n,m} \psi_{m,\vec{k}}(\vec{r}) d\vec{k}, \tag{4.7}$$

where $\psi_{m,\vec{k}}(\vec{r})$ is the Kohn-Sham orbital of band m with Bloch quasi-momentum $\vec{k}$. V and $\vec{R}$ is a vector in the Bravais lattice. $U^{\vec{k}}_{n,m}$ is a unitary transformation on the Kohn-Sham orbitals; All physical properties are invariant under any choice of this unitary transformations. For the special case of Γ-point sampling, Eq. 4.7 can be simplified to:

$$W_{n,\vec{R}}(r) = \sum_m U_{n,m} \psi_m(\vec{r}). \tag{4.8}$$

Due to the gauge freedom in choosing the unitary transformation $U_{n,m}$, the definition of Wannier functions is not unique. Marzari and Vanderbilt [103] defined an unique way to construct "maximally-localized" Wannier functions from the Kohn-Sham orbitals by minimizing the total spreads of the Wannier functions

$$\Omega = \sum_{n=1}^{N} (\langle W_n | r^2 | W_n \rangle - \langle W_n | r | W_n \rangle^2) \tag{4.9}$$

Wannier functions can be a powerful tool in studying the electronic and dielectric properties of materials, and can also provide an insightful picture of the chemical bonding nature. Moreover, the "centers of charge" of the Wannier functions can provide a classical correspondence for the "location of an electron". Using the "centers of charge", a set of Wannier functions belonging to a particular molecule can be selected and the molecular contributions to the Compton profile due to that particular molecule can be computed. We employed this technique to study the relations between hydrogen bonding and Compton profiles in Section 4.9.

Table 4.1: Temperatures and densities used in ab-initio simulations for different thermodynamics state points studied

77 °C, 1 atm (Ambient)	200 °C, 300 bar (Subcritical)	300 °C, 300 bar (Subcritical)	397 °C, 300 bar (Near critical point)	430 °C, 300 bar (Supercritical)
0.97 g/cm^3	0.89 g/cm^3	0.76 g/cm^3	0.40 g/cm^3	0.19 g/cm^3

4.5 Rigid water simulations at ambient and supercritical conditions

In this section, we discuss our extensive Car-Parrinello molecular-dynamics simulations of water at ambient and supercritical conditions. It has been shown that ab-initio molecular dynamics simulations of water at room conditions gives an unphysical glassy-like state [26, 27]. Liquid-water characteristics appear only when the simulation temperature is raised to 127 °C [28, 71]. This discrepancy is believed to be due, at least in part, to the quantum effects of high-frequency intramolecular modes at room temperature. Those high-energy modes are expected to be frozen in their zero-point motion and the exchange of energy with other degrees of freedom is very unlikely. Ab-initio molecular dynamics simulations with rigid water molecules, which partly mimic these intramolecular quantum effects, has been shown to produce a better description of liquid water at room conditions [86]; and rigid water shows indeed liquid-like properties down to a temperature of 77 °C. In view of this, all the Car-Parrinello simulations in this work were done with 32 rigid water molecules, using the SHAKE algorithm.

We performed extensive simulations of normal water at ambient, subcritical and supercritical regimes at 77, 200, 300, 397 and 430 °C. The simulations were done at constant volume with the density fixed at the experimental density at 300 bar (at 77 °C, the density is the one at 1 atm and differs by less than 4% from the one at 300 bar). Simulation conditions are summarized in Table 4.1. In all the simulations, ultrasoft pseudopotentials and PBE-GGA (described in Section 3.2) were used. Plane-wave energy cutoffs of 25 Ryd and 200 Ryd were chosen to expand the wavefunctions and

the charge density, respectively. A fictitious mass μ of 1100 a.u. and a timestep of 10 a.u. were used to integrate the equations of motions. Each simulation gathered about 17 ps of production time after more then 15 ps of "flexible" water simulation at the same conditions. At each temperature, the Compton profiles were calculated from the average of 10 configurations equally spaced apart.

4.5.1 SHAKE algorithm

In Car-Parrinello molecular dynamics, the ions are moving according to the forces derived from the Car-Parrinello Lagrangian and, therefore, there is no restriction on molecular structures. In order to perform molecular dynamics with rigid water molecules, we imposed structural constraints using the SHAKE algorithm [104]. In the SHAKE algorithm a constraint $g(r)$=0 is added to the Lagrangian and the equations of motion for ions are altered by the constraint

$$\mathcal{L} = T - V + \lambda g(r), \tag{4.10}$$

$$m\ddot{r} = -\frac{\partial V(r)}{\partial r} + \lambda \frac{\partial g(r)}{\partial r}. \tag{4.11}$$

For our water simulations, two O-H bond lengths and the H-O-H angle are fixed by these constraints. The bond angle constraint can be more straight-forwardly imposed, in this case, by fixing instead the H-H distance in each molecule. To choose appropriate bond lengths and bond angles for the rigid water molecules, we calculated the average bond lengths and angles from simulations with flexible water molecules at various conditions. The average bond lengths and angles do not vary significantly from ambient to supercritical conditions, and d_{OH}=0.995 Å and $\angle_{HOH} = 105.0^o$ were taken as the reference geometry to be imposed to the rigid water molecules. With three constraints on each molecule, the total number of degrees of freedom for a system with m water molecules (i.e. $3m$ atoms) is now $3(3m) - 6 - 3m = 6m - 6$. The number of degrees of freedom is important in calculating the temperature of the system when a (Nose-Hoover) thermostat is used during the simulations.

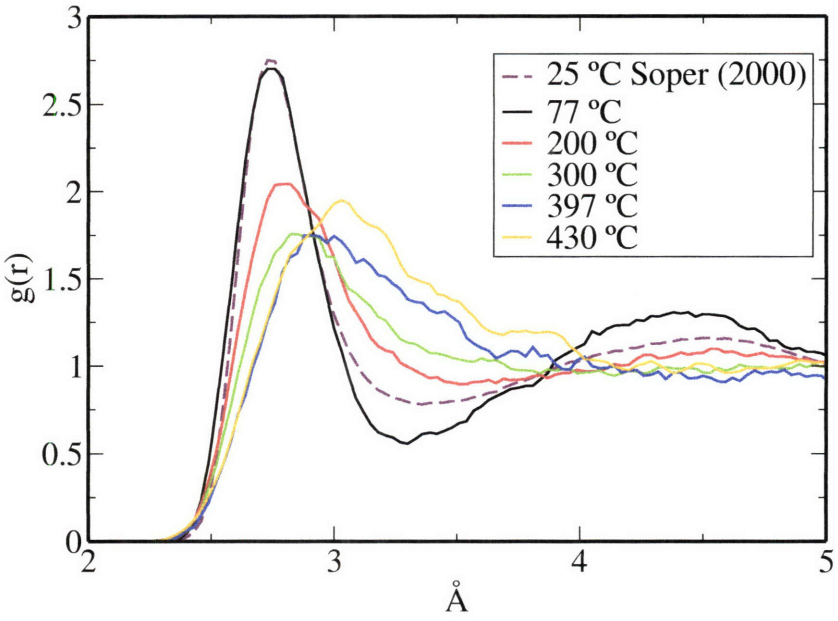

Figure 4-2: O-O radial distribution functions from simulations at different thermodynamic state points and comparison with the experimental data at ambient condition.

4.6 Structural and dynamical properties

Fig. 4-2 shows the O-O radial distribution functions for the simulations at the thermodynamic state points described in Table 4.1. On the same figure, we have included the experimental O-O radial distribution function at 25 ^{o}C [3]. The first peak for the theoretical radial distribution functions of rigid water molecules at 77 ^{o}C agrees well with the experimental data at ambient conditions. Unfortunately, there is no experimental radial distribution functions at the same conditions for the other thermodynamic state points. We have instead compared the self-diffusion coefficients between simulations and experiments (Table 4.2). The self-diffusion coefficients in the simulations are calculated from the slopes of the mean square displacement curves.

From Table 4.2, the agreement between simulations and experiments at higher temperatures is very good and progressively better as the temperature increases. This can be understood by the fact that the discrepancies between simulations and

Table 4.2: Comparison of self-diffusion coefficients between simulations and experiments at different thermodynamic state points.

	Simulations (10^{-5} cm^2/s)	Experiments [105,106] (10^{-5} cm^2/s)
77 °C (Sim.), 30 °C (Expt.), 1 bar	1.5	2.6
200 °C, 300 bar	9.5	27.7
300 °C, 300 bar	26.0	37.4
397 °C, 300 bar	69.1	82.5
430 °C, 300 bar	163.3	174.4

experiments are believed to be due to the poor descriptions of hydrogen bonding interactions (either because of the ionic quantum effects or the choice of exchange-correlations functionals). As temperature increases, hydrogen bonding becomes less significant and, therefore, the agreement in self-diffusion coefficient is expected to improve.

4.7 The effects of hydrogen bonds on the Compton profile

When a hydrogen bond is formed, the lone-pair orbital of one of the water molecules approaches the other molecule, and the lone-pair orbital, forced be orthogonal to the orbitals of the other molecule, becomes more structured in real space. This structuring leads to a broadening of the electronic momentum density in reciprocal space, and the Compton profile is, therefore, broadened. As shown in Fig. 4-3, the Compton profile calculated from the simulation at 77 °C, which is expected to have a stronger hydrogen-bonding structure, is more broadened than that of 430 °C. However, this broadening is not very pronounced. Instead of looking at the absolute profile, it becomes useful to plot the difference in Compton profiles with respect to a reference state.

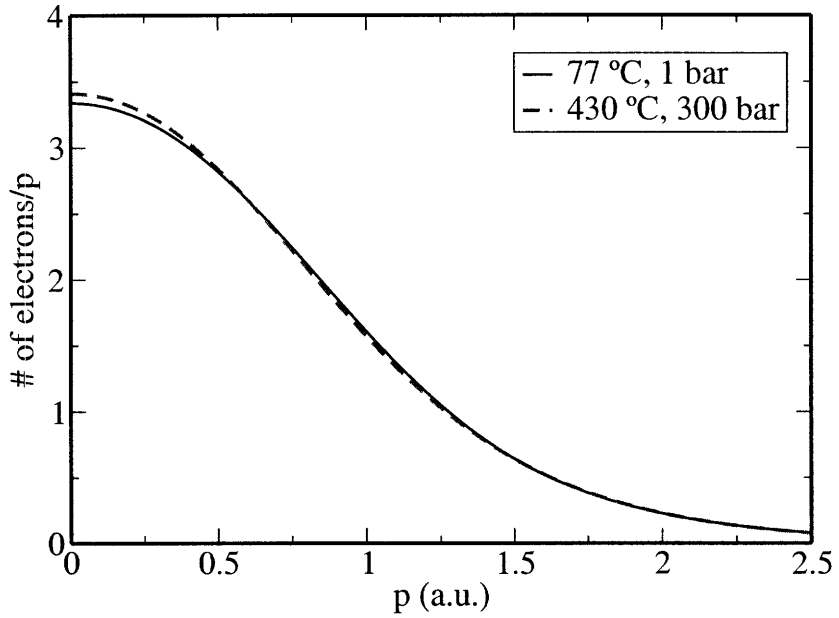

Figure 4-3: The absolute Compton profiles for the simulations at 77 °C and 430 °C. Water at 77 °C, having stronger hydrogen bonding network, shows a more broadened Compton profile than that of water at 430 °C.

4.8 Compton profile differences

We now show in Fig. 4-4(a) the experimental $\Delta J(p)$ for all the state points considered, and contrast it with the one obtained from the first-principles molecular dynamics simulations (Fig. 4-4(b)). $\Delta J(p)$ is defined as

$$\Delta J(p) = J_{reference}(p) - J(p), \tag{4.12}$$

with respect to the liquid reference state. The reference state in the experiments is taken at 30 °C, while in the rigid-water, first-principles simulations, at 77 °C, for the reasons mentioned above. The simulation data are convoluted with a Gaussian of σ=0.218 a.u. (1 a.u. in momentum space equals $\frac{2\pi}{1 \text{ bohr}}$) to match with the experimental resolution. Since the reference state is expected to have the strongest hydrogen bonding (i.e. largest broadening in the Compton profile), the Compton profile differ-

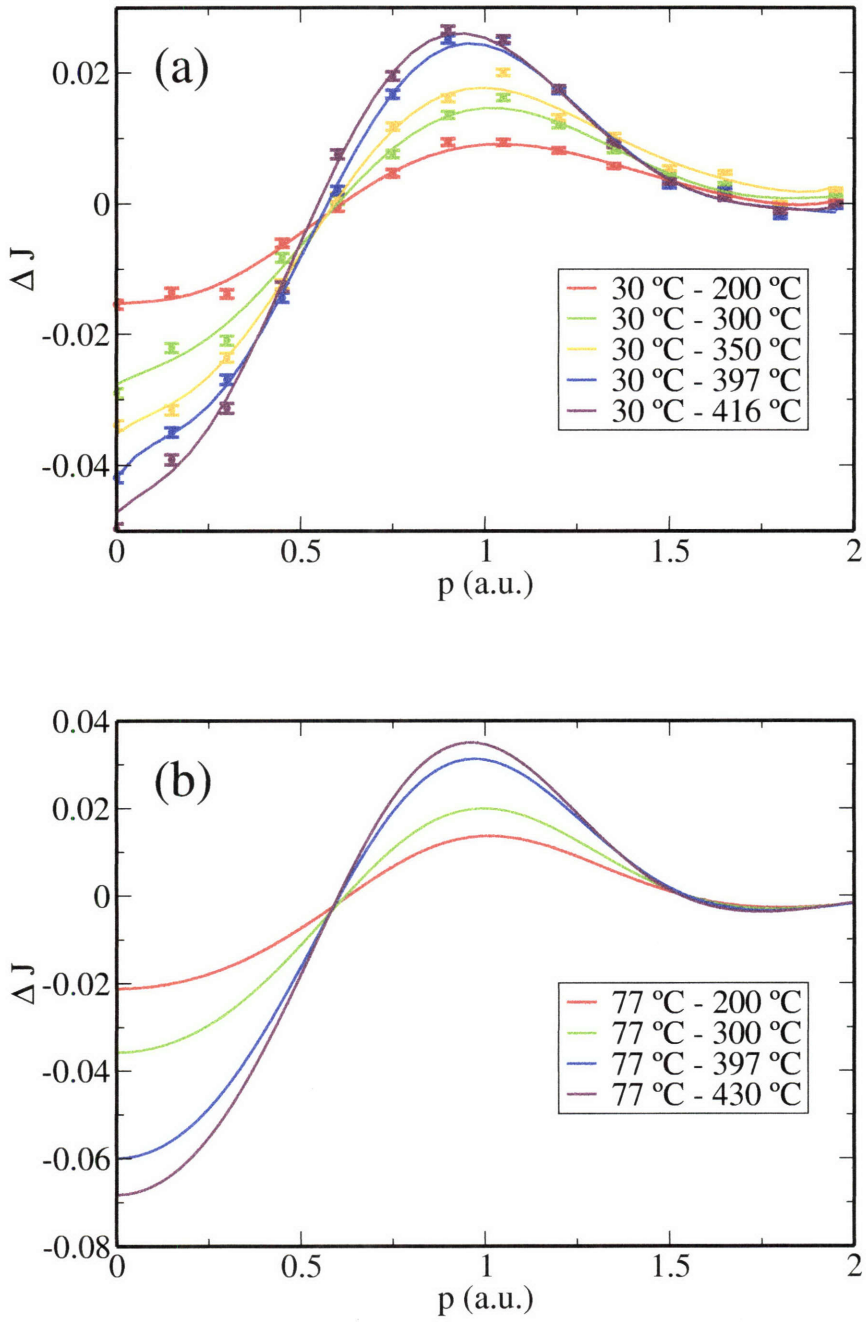

Figure 4-4: (a)Experimental Compton profile difference $\Delta J(p)$ (in electrons per atomic unit of momentum) with respect to the experimental reference state as a function of temperature. The curves are polynomial fits which act as guides for the eye; the experimental data (with error bars) are given by the solid circles. (b)Theoretical Compton profile difference $\Delta J(p)$ (in electrons per atomic unit of momentum) with respect to the theoretical reference state as a function of temperature. The temperature of reference state is 30 °C for the experiments, 77 °C (and density 0.97 g/cm^3) for the theory.

ences are negative in the small p region, and become positive and attain their peak at around p=1 a.u.

It can be seen that the overall agreement between experiments and simulations is excellent - with the caveat that the theoretical amplitudes overestimate the experimental values by $\approx$40%. However a single rescaling factor of 0.73 brings all theoretical curves for all p in quantitative agreement with experiment. The existence of this rescaling factor has been discussed in the literature, e.g. for the Compton profile anisotropy of ice [94, 101] and it allows us to make a significant advance as shown below.

$J(p)$ is sensitive, especially in the low momentum region, to the valence electronic wavefunctions. $\Delta J(p)$ is non-zero precisely in this region and measures changes in the bonding brought about by breaking or formation of hydrogen bonds. Inspired by these considerations and the fact that the area under the Compton profile corresponds to the amount of scattering electrons, we propose an electronic measure of hydrogen-bonding in water. This is the amount of electrons whose momentum space wave function changes in going from a reference state (chosen here as water under normal conditions) to the one being measured and is obtained directly from the Compton profile difference for the two states:

$$n_e = \frac{1}{2}\int_{-\infty}^{\infty} |\Delta J(p)|\, dp. \tag{4.13}$$

This sum-rule measures the number of electrons affected when hydrogen bonding is altered and in our case tracks the progressive breaking of hydrogen bonds as the temperature is raised from ambient conditions (the $\frac{1}{2}$ is to take into account double counting). The experimentally-determined n_e, and the one obtained from the simulations (after rescaling the latter to 73% of the original values, as mentioned above), are plotted in Fig. 4-5 as a function of temperature. The excellent agreement reflects the striking similarity in the shape of the experimental and theoretical $\Delta J(p)$ in Fig. 4-4(a) and (b). It should be noted that n_e(T) in Fig. 4-5 does not saturate, indicating that even at the highest temperatures considered hydrogen bonds remain.

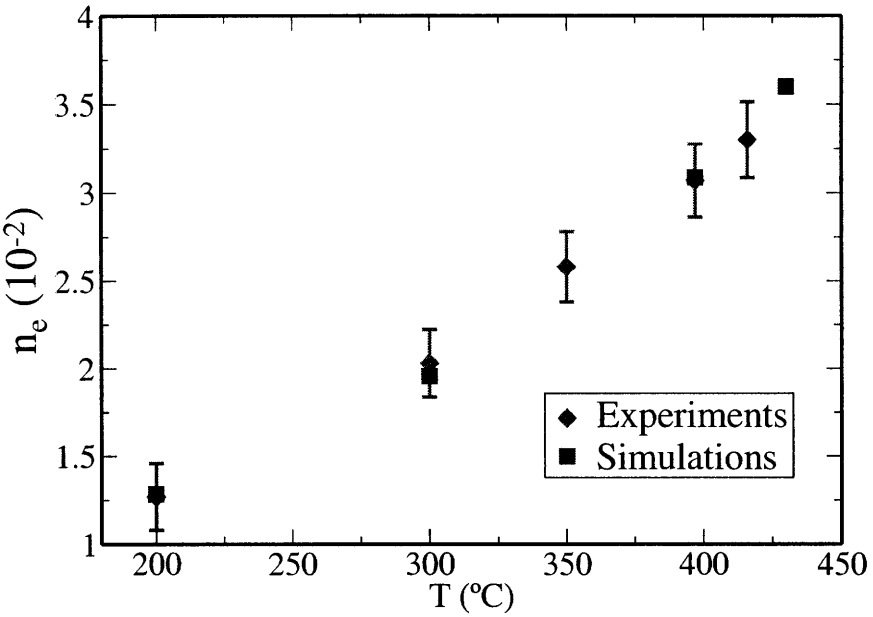

Figure 4-5: The integration of the absolute value of the profile difference, n_e, (see Eq. 4.13) as a function of temperature for simulations (squares), after scaling down to 73% of the original values, and experiments (diamonds).

4.9 The relation between n_e and hydrogen bonding

In the preceding section we have linked n_e to the variation in hydrogen bonding as expressed through the temperature of the system. In the following we make the direct connection between n_e and n_{HB} by studying a model system: a cluster containing five water molecules, one at the center and the other four surrounding it in a tetrahedral arrangement. A single hydrogen bond can then be formed or broken simply by removing, one at a time, the four outer molecules. This model was already considered in Ref. [96]. At variance with the previous studies, we can actually resolve the Compton profiles of the individual molecular contributions, taking advantage of the decomposition offered by the maximally-localized Wannier functions technique. Thus, we can compute the Compton profile of the central molecule only, as the hydrogen bonds with its neighbors are broken, one at a time. The number of hydrogen bonds formed by the central molecule n_{HB} is clearly defined within this framework.

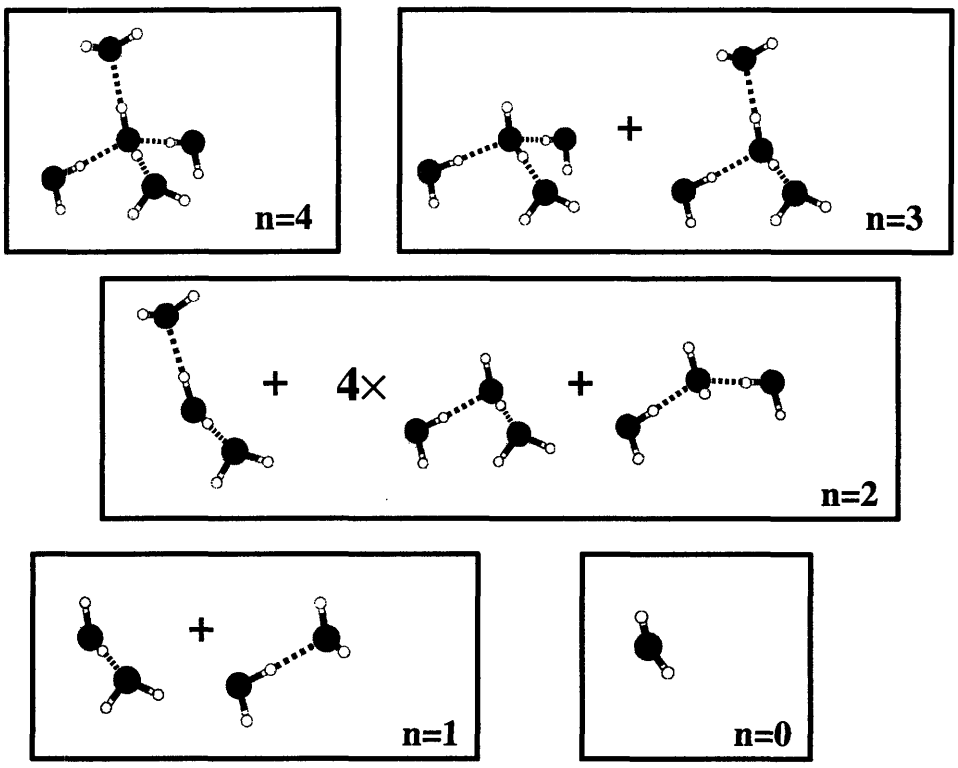

Figure 4-6: Procedure to calculate the Compton profiles at different n_{HB} using a model structure of 5 water molecules. An hydrogen bond can be formed or broken by changing the O-O distance between the center oxygen with its four oxygen neighbors. n_{HB} is defined as the number of hydrogen bonds formed by the center molecule. The Compton profile for each value of n_{HB} is calculated by averaging over possible configurations having the same n_{HB}.

The corresponding Compton profile has been calculated by averaging over all the possible clusters with a given n_{HB}, as shown in Fig. 4-6.

With 77 °C as the reference state, we plot in Fig. 4-7 the Compton profile differences for different n_{HB}. Then, we can compare n_{HB} with the computed n_e from Fig. 4-7. The n_{HB} dependence as a function of n_e can then be obtained and rescaled by the factor determined experimentally (Fig. 4-8, squares) and is clearly seen to be linear. The slope of this variation gives the number of electrons involved in one hydrogen bond. Most remarkably, the water simulations - ranging from normal conditions to the supercritical regime - obey the same identical trend, and fall on this universal straight line, as shown by the circles in Fig. 4-8. For these points, the average number of hydrogen bonds per molecule is measured according to the structural criterion of

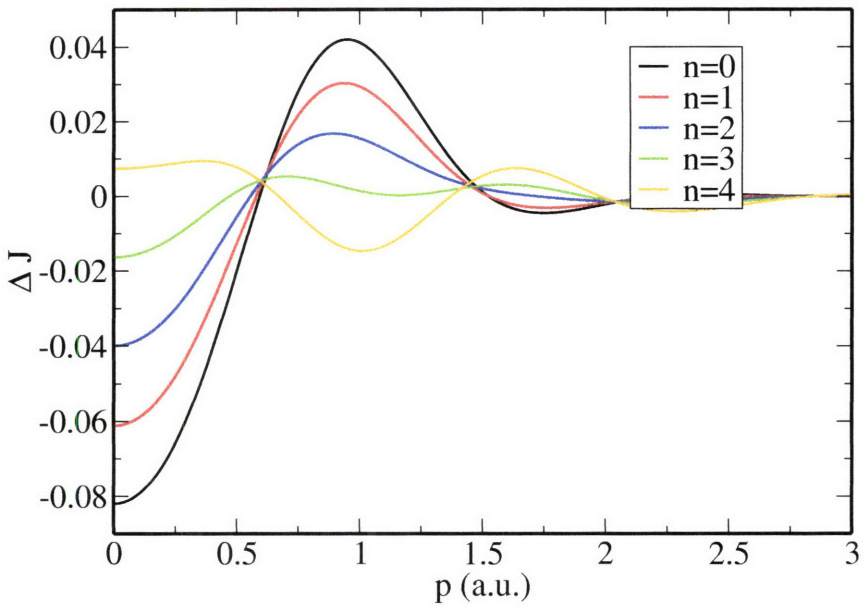

Figure 4-7: Compton profile differences for different n_{HB} calculated from different clusters with 77 ^{o}C as the reference state.

Ref. [88]. This is the central result of this work, demonstrating a linear relationship between n_e and n_{HB} under a wide variety of conditions, ranging from the normal to the supercritical regime, and establishing Compton scattering as an accurate and direct probe of hydrogen bonding in water. It is worthwhile to notice that the central water molecule of our cluster is surrounded only by its first coordination shell and that in the bulk liquid, longer range interactions exist, mostly mediated by dispersion and electrostatic forces. However, even in the liquid the linear relationship between n_e and n_{HB} holds indicating that the overwhelming contribution to the sum rule for n_e is from the first coordination shell.

The slope of the line in Fig. 4-8, as mentioned earlier, provides directly an absolute measure of the number of electrons involved per hydrogen bond - the universal relation above, assigns a value of 0.013 electrons per molecule for every bond that is broken (or formed). The bonding and coordination picture that emerges from this results remains in close agreement with the established understanding of coordination in

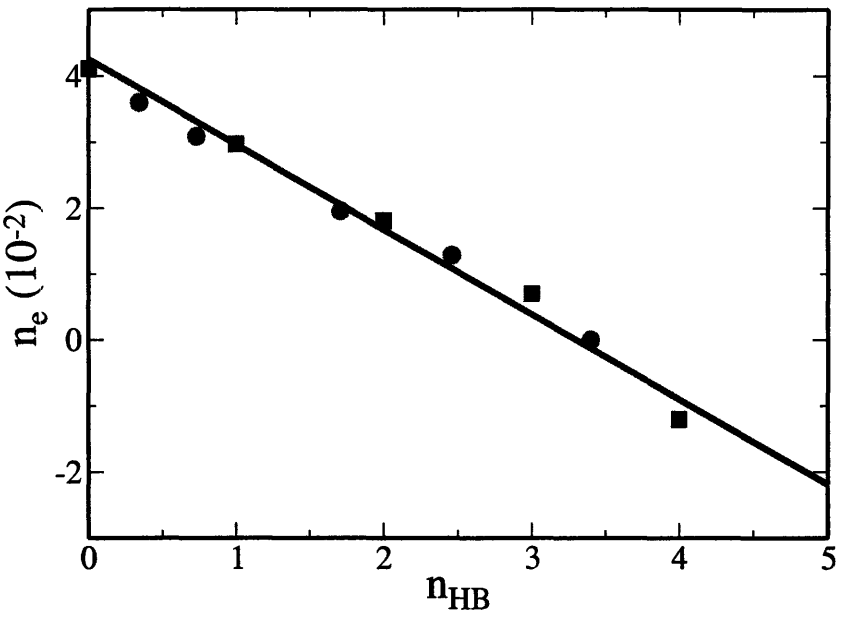

Figure 4-8: n_e as function of the number of H-bonds per molecule (n_{HB}) (liquid water at ambient condition as the reference state) . Square: ice clusters (the Compton profiles are only calculated from the center molecule). Circle: rigid water simulations.

water. Our final estimates for all state points measured are summarized in Table 4.3, where we can see that in going from the normal state to the supercritical regime and beyond, n_{HB} decreases from 3.4 (compared to the value 3.58 from Ref. [78]) to 0.34.

4.10 Connectivity of hydrogen-bond network

We now examine the connectivity of the hydrogen-bond network as we move from the normal to the supercritical regime. Fig. 4-9(a) shows three snapshots from our simulations which illustrate the hydrogen bond connectivity at different conditions. Since the density changes considerably the volume considered for the simulation also varies as is seen by the change in size of the molecules across the different panels. In a snapshot from 200 °C, blue molecules are those networked with more than 5 other molecules while the very few red ones are non-networked monomers. Simulation at 300

Table 4.3: Experimental and theoretical (after scaling of 0.73) n_e, and theoretical n_{HB} at different state points. The first column shows the experimental temperature and pressure at each state point. The theoretical temperatures and pressures are the same as the experimental ones except in the first and the last state points shown below, which are (77 °C, 1 bar) and (430 °C, 300 bar). respectively.

Temperature and pressure	$n_e(10^{-2})$ (experiment)	$n_e(10^{-2})$ (theory)	n_{HB} (theory)
30 °C, 300 bar			3.40
200 °C, 300 bar	1.27 ± 0.19	1.28	2.46
300 °C, 300 bar	2.03 ± 0.19	1.96	1.71
350 °C, 300 bar	2.58 ± 0.20		
397 °C, 300 bar	3.07 ± 0.21	3.09	0.73
416 °C, 300 bar	3.30 ± 0.21	3.60	0.34

°C shows sizeable amounts of green (networked with between 2 and 5 other molecules) as well as some red molecules. Finally, a snapshot from the 430 °C simulation has a large monomer population but also a few clusters of less than 6 molecules. To quantify these observations, we show in Fig. 4-9(b) the distribution of cluster sizes at a given simulation - n molecules belong to a cluster if they all have hydrogen bonds with each other. At normal conditions almost all the water molecules are connected to each other. The percolation transition occurs between 300 °C and 397 °C as shown in Table 4.3 and is consistent with the well known percolation threshold $n_{HB} = 1.53 - 1.55$, [108, 109]. This is also reflected in the bimodal in distribution at 300 °C and the distributions at 397 °C and 430 °C showing a dominating amount of monomers but also a substantial amount of dimers and trimers, indicating that hydrogen bonds is still non-negligible in supercritical conditions: in experiment, we found n_{HB}=0.74±0.16 at 416 °C, while theory predicts n_{HB}=0.34 at 430 °C.

4.11 Conclusions

In conclusion, Compton scattering data provide a stand-alone and absolute measurement of the number n_e of electrons per water molecule involved in the hydrogen bond.

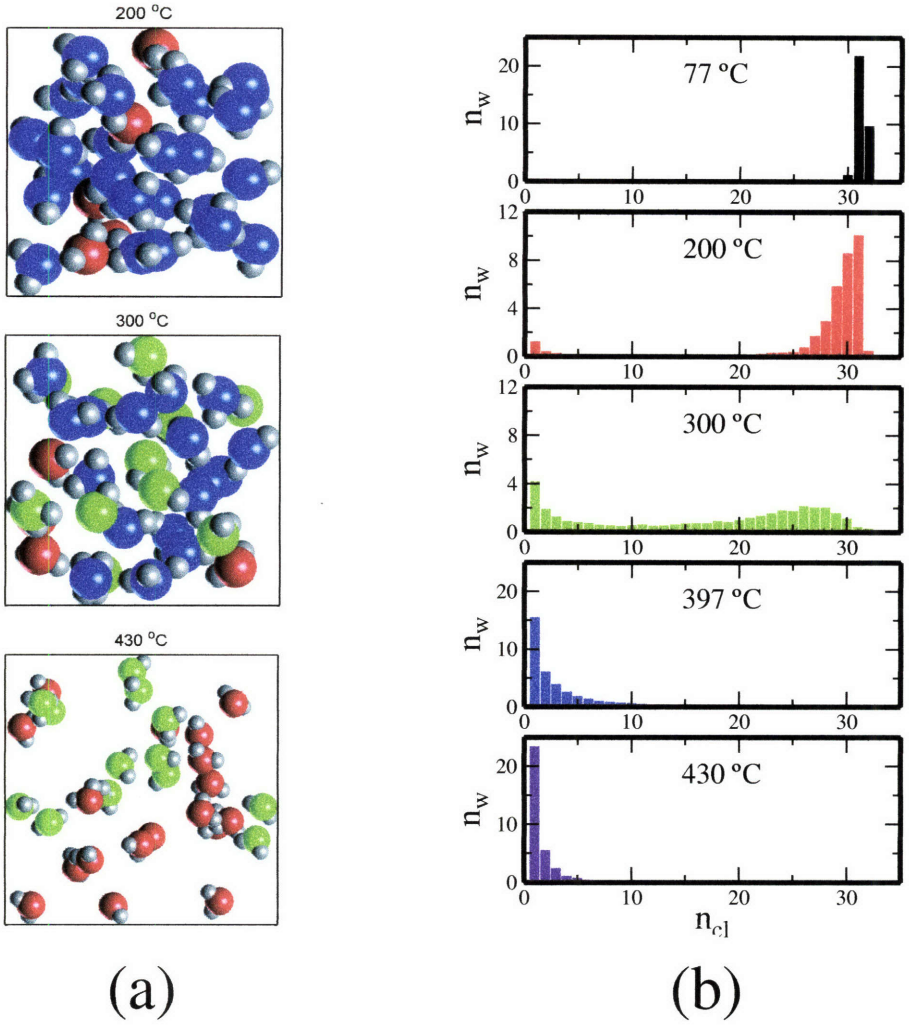

Figure 4-9: (a) snapshots of simulations at 200 °C, 300 °C and 430 °C. The color code represents water molecule connectivity. Blue: molecules networked with more than 5 other molecules; green: molecules networked with 2 to 5 other molecules; red: monomers. (b) Number of water molecules (y-axis) distributed in clusters of different sizes (x-axis) for various temperatures.

By using state-of-the-art first-principles simulations we demonstrate that n_e provides a measure of coordination and a rigorous definition for the average number n_{HB} of hydrogen bonds per water molecule over a large temperature range. Our study supports the existence of quasi-tetrahedral coordination in ambient conditions and the observation that hydrogen bonding persists above the critical point. This approach should prove valuable in the future to address many issues in hydrogen bonded networks and chemical bonding in general.

THIS PAGE INTENTIONALLY LEFT BLANK

Chapter 5

Study of electron-transfer reactions from first-principles molecular dynamics

5.1 Introduction

Electron transfer is one of the most important processes in nature [110]. Despite its simplicity, electron-transfer reactions are central to molecular events in inorganic and organic redox chemistry. For example, electron transfer has been recognized as crucial in biological metabolism where small molecules such as water, nitrate, dioxygen, etc. are converted to composite biomolecules. Moreover, it is the primary event which follows light absorption in the photosynthetic system and in the mitochondrial events leading to dioxygen reduction in respiratory metabolism.

In studying electron-transfer reactions, the free energy barrier and the transfer matrix element are two key parameters to look at. In particular, there have been numerous calculations aiming at accurately obtaining free energy barriers (or equivalently the reorganization energy in some cases) with classical molecular dynamics [19, 20, 111–114] or static first-principles calculations [115]. While studies with classical potentials usually produce the correct qualitative picture, the values of the

reorganization energies (the free energy cost to move from the equilibrium configurations of the product to those of the reactant without the transfer of electron) and the free energy barriers, can not be accurately obtained. On the other hand, static first-principles calculation has been shown to give correct quantities in some simple reactions [115], but whether the same level of accuracy can be attained in complex reactions is questionable because of the neglect of the entropic effects. In order to construct an universal approach to accurately describe electron-transfer reactions both qualitatively and quantitatively, we decided to combine molecular dynamics and first-principles techniques. To our knowledge, no one has ever performed first-principles molecular dynamics studies of full electron-transfer reactions because of some fundamental and conceptual problems in density-functional approaches (see Section 5.9).

5.2 Marcus theory of electron transfer

The theory of electron transfer in polar solvent was developed by R. A. Marcus in the 1950s [2, 36, 37, 116, 117]. Since its introduction, the Marcus theory has become the framework for the study of electron-transfer reactions and Marcus, in recognition of his contributions to the field, was awarded the Nobel prize in 1992. In this section, we will give a brief introduction to the electron-transfer mechanism in Marcus scenario.

Consider an electron transfers from a donor species D^{m+} to an acceptor species A^{n+} in solution. First, D^{m+} and A^{n+} must diffuse through the solution and come into proximity to form a complex $D^{m+}A^{n+}$, in which the donor and acceptor are separated by a distance at which the electronic coupling matrix element is significant. In the Marcus scenario (Fig. 5-1), when the complex is formed, the system has two states, corresponding to the two relevant electronic states (reactant and product states) $D^{m+}A^{n+}$ and $D^{(m+1)+}A^{(n-1)+}$. The potential energy of the reactant state (or the product state) and the surrounding medium is a function of all of these nuclear coordinates, and defines a multi-dimensional potential energy surface.

In order for the electron transfer to occur, two principles have to be satisfied, 1) the Franck-Condon principle and 2) the conservation of energy. According to the

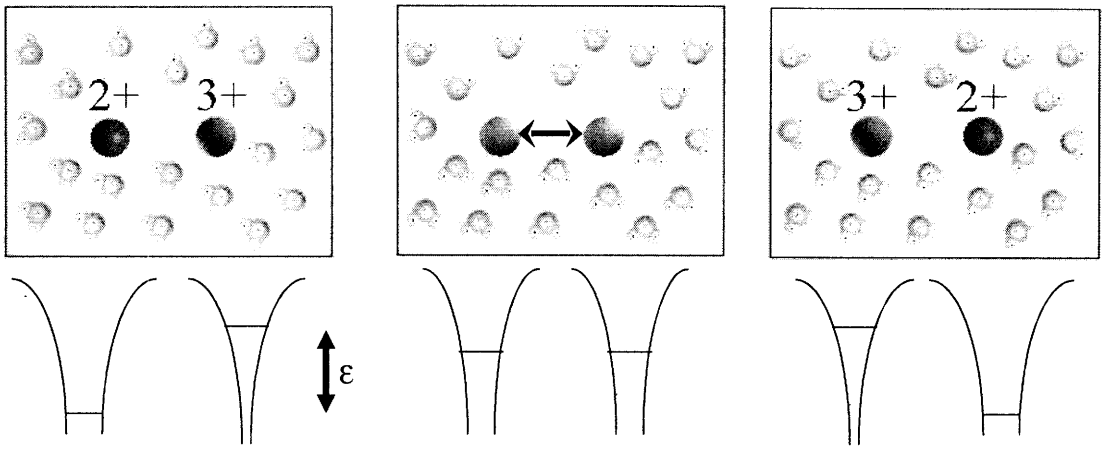

Figure 5-1: Schematic diagram of the electron-transfer process. The solvent fluctuations mediate the transfer process and the transfer occurs when the reactant and the product states are degenerate.

Franck-Condon principle, the electron, being a light particle, transfers from the donor site to the acceptor site instantaneously so that the ions do not have time to change either their positions or momenta. The conservation of energy requires that the product and reactant are degenerate during the transfer process. Since the ions are stationary during the transfer process, the conservation of energy requires, in a picture of independent electrons, degeneracy for the transferring electron to be at the donor or the acceptor site. This degeneracy is usually achieved with thermal fluctuations of the solvent and of the donor and the acceptor molecules. This temporary reorganization creates a situation where the electron resonates between the sites. If there were a finite coupling between the two electronic states, transfer could occur, and relaxations of the solvent molecules would then localize the electron on the new site.

Like other chemical reactions, it is important to define a reaction coordinate to characterize the role of ionic configurations on electron-transfer reactions. However, the solvent fluctuation effects on the reactant and product energies is a collective quantity depending on all the ionic coordinates of the solvent. In order to capture these collective contributions, the reaction coordinate (ϵ) of a particular ionic configuration is defined as the potential energy difference between the product and the reactant state at that configuration [20] and this choice of the reaction coordinate is also called the Marcus energy gap.

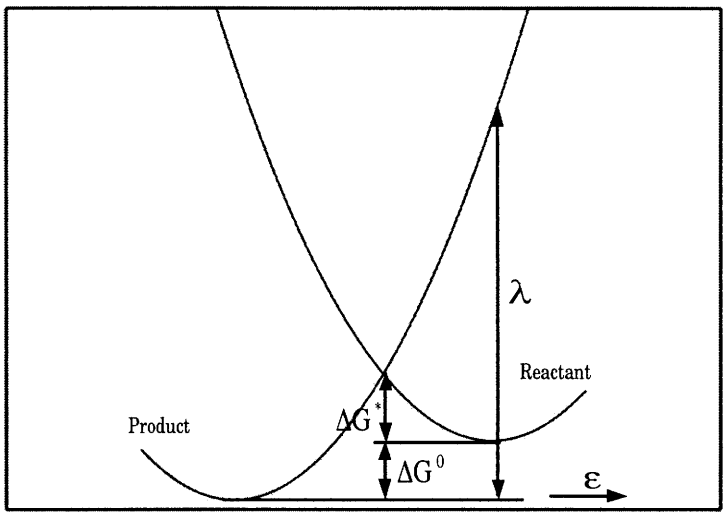

Figure 5-2: Diabatic free-energy surfaces for a typical electron-transfer reaction.

Fig. 5-2 show a simplified diagram of the free-energy surfaces of an electron-transfer reaction as a function of this reaction coordinate. As mentioned above, the electron transfer occurs when the reactant and product are degenerate, i.e. when $\epsilon = 0$. Once the system reaches the intersection of the two curves in Fig. 5-2, the probability of going from the reactant to the product free-energy surface depends on the extent of coupling of the electronic orbitals for the two reactants, which in turn depends on the separation distance r of the reactants.

The electron-transfer rate constant can be written as

$$\begin{aligned} k_{ET} &= \text{Rate of the system reaching the free-energy surfaces intersection} \\ &\times \text{Probability of electron tunneling at the intersection.} \end{aligned} \tag{5.1}$$

The rate of the system reaching the intersection depends on the solvent relaxation time and the temperature, and the electron tunneling probability is directly related to the electronic coupling matrix element between the reactant and the product states.

Depending on the electronic coupling magnitude, the electron-transfer reaction can be classified into adiabatic and diabatic processes.

In adiabatic reactions, the coupling is large so that the time for tunneling to occur is small compared to the time needed for the system to reach the intersection of the free-energy surfaces. Therefore, electron tunneling occurs whenever the interaction is reached. Therefore, probability of electron tunneling = 1. In this regime, the rate constant can be written as

$$\begin{aligned} k_{ET} &= \text{Rate of the system reaching the intersection of the curves} \\ &= Ae^{-\Delta G^*/k_B T}, \end{aligned} \tag{5.2}$$

which is the Arrhenius probability of reaching the intersection from the bottom of the reactants' free-energy surface, where G^* is the free-energy barrier. An adiabatic process usually occurs when the donor and the acceptor are in close contact, as in the case of some inner-sphere electron transfer processes.

In the diabatic limit, the tunneling matrix element is small and the system has to diffuse up to the intersection several times before the electron tunnels. Such a weak coupling case can be treated quantum mechanically using Fermi's golden rule. In the diabatic case, k_{ET} can be written as

$$k_{ET} = \frac{2\pi}{\hbar}|H_{DA}|^2 FC, \tag{5.3}$$

where H_{DA} is the electronic coupling matrix element between the donor and the acceptor. FC is the Franck-Condon factor and is equal to $\frac{exp(-(\Delta G^* k_B T)}{(4\pi\lambda k_B T)^{1/2}}$ in the classical case. Diabatic electron transfer usually occurs over long distances.

If we assume the free-energy surfaces to be parabolic (see Section 5.3), ΔG^* can be written as

$$\Delta G^* = \frac{(\Delta G^0 + \lambda)^2}{4\lambda}, \tag{5.4}$$

where λ, the reorganization energy, is the free energy cost to change from the equilibrium configurations of the product into the equilibrium configurations of the reactant

without the electron transfer having taken place.

5.3 Spin-Boson model for electron transfer

When studying a quantum-mechanical system with a limited number of degrees of freedom in contact with a dissipative environment, we can look into a simple model which can capture all the essential physics. The Spin-Boson model has been widely used to investigate these kinds of problems of a quantum system interacting with the environment. In this section, we will discuss the use of the Spin-Boson model to study electron-transfer reactions and its implication on the properties of the free-energy surfaces.

For the simplest model, which is a two-state quantum system totally isolated from the environment, we can write the Hamiltonian as,

$$H = E_0\sigma_z - K\sigma_x, \tag{5.5}$$

where we used the notation of the Pauli matrices:

$$\sigma_x = \begin{pmatrix} 0 & 1 \\ 1 & 0 \end{pmatrix}, \tag{5.6}$$

$$\sigma_z = \begin{pmatrix} 1 & 0 \\ 0 & -1 \end{pmatrix}. \tag{5.7}$$

The diabatic states (ϕ_R and ϕ_P) are defined as the eigenstates of σ_z, whose energies are $\pm E_0$, and K is the coupling strength between the two diabatic states. When the diabatic states have the same energy (E_0=0), the system shows a dynamical behavior which has no classical analog. In this case, the eigenstates of Eq. 5.5 become the linear combinations of the two diabatic states ($\psi_0 = \frac{1}{\sqrt{2}}(\phi_R + \phi_P)$ and $\psi_1 = \frac{1}{\sqrt{2}}(\phi_R - \phi_P)$). Since the diabatic states are not eigenstates of the system, if we prepare the system

in one diabatic state, the probability to find the system at time t in the other state is $P(t) = sin^2\frac{K}{\hbar}t$. This tunneling occurs because the phase of the two eigenstates changes with different frequencies, according to their eigenenergies, and the coupling term K dictates the tunneling frequency.

This two-state model (Eq. 5.5) is exactly solvable for any value of E_0, but it is the simplest of systems with no interaction with the environments. In reality, almost every two-state system (as in the case of the electron-transfer reactions) interacts with the environment, and the interactions can be so strong that the system is altered both quantitatively and qualitatively. The interactions with the environment can be introduced in the Hamiltonian through a term $\sigma_z\hat{\Omega}$, where $\hat{\Omega}$ is some operator of the environment. The environment can be regarded as an "observer" to the system and the system is observing the value of σ_z, from the form of this extra term. As we expect, the act of observing the system will destroy the phase coherence between the diabatic states, meaning the temporal behavior of the system is no longer $P(t) = sin^2\frac{K}{\hbar}t$. In general, the spin-boson Hamiltonian can be written as,

$$\begin{aligned} H &= E_0\sigma_z - K\sigma_x \\ &+ \sigma_z\sum_\alpha C_\alpha x_\alpha + H_b(\{m_\alpha\},\{\omega_\alpha\}). \end{aligned} \tag{5.8}$$

$H_b(\{m_\alpha\},\{\omega_\alpha\})$ is the Hamiltonian for the bath. Given that the coupling between the environments and the system is sufficiently weak, it is most convenient to write the Hamiltonian for the bath as a set of harmonic oscillators [118]:

$$\begin{aligned} H &= E_0\sigma_z - K\sigma_x \\ &+ \sigma_z\sum_\alpha C_\alpha x_\alpha + \sum_\alpha(\frac{1}{2}m_\alpha\omega_\alpha^2x_\alpha^2 + p_\alpha^2/2m_\alpha). \end{aligned} \tag{5.9}$$

The first two terms corresponds to the original Hamiltonian describing the isolated quantum system–the spin system. The environment, which is modeled by a set of harmonic oscillators, is represented by the forth term – the boson system. The third term represents the interactions between the quantum system and the environment,

which is taken as the linear coupling of the spin system with the boson system. The frequencies ω_α and masses m_α of the harmonic oscillators are independent of the quantum system and the constant C_α's define the coupling strength between the two systems. This simple form to describe the environment and a linear coupling preserves a richness of behavior, which is controlled by the values of C_α and K, and by the form of the density of states (the ensemble of frequencies) for the oscillators. As depicted by Chandler [119], the Spin-Boson Hamiltonian is a good theoretical model to investigate electron-transfer reactions. The two diabatic states of the quantum system corresponds to the the two electronic states, $D^{m+}A^{n+}$ and $D^{(m+1)+}A^{(n-1)+}$. The polar solvent, in this case, is the environment and the electrostatic interactions with the electronic states become the coupling. Within the Spin-Boson model, if the environments couple with the system linearly and the random variables $\{x_\alpha\}$ describing the environments are independent of each other, the reaction coordinate obeys Gaussian statistics and the free-energy surfaces are parabolic as will be shown below.

The Hamiltonian can be generalized as,

$$\begin{aligned} H &= \begin{pmatrix} E_R & -K \\ -K & E_P \end{pmatrix} + \sum_\alpha C_\alpha x_\alpha \begin{pmatrix} 1 & 0 \\ 0 & -1 \end{pmatrix} \\ &+ \sum_\alpha (\frac{1}{2} m_\alpha \omega_\alpha^2 x_\alpha^2 + p_\alpha^2/2m_\alpha) \begin{pmatrix} 1 & 0 \\ 0 & 1 \end{pmatrix} \\ &= \begin{pmatrix} H_R & -K \\ -K & H_P \end{pmatrix}. \end{aligned} \tag{5.10}$$

E_R and E_P are the energies of the diabatic states (ϕ_R and ϕ_P) in the absence of the

environments, respectively. The reaction coordinate can be written as,

$$\epsilon = H_P - H_R = E_P - E_R + 2\sum_\alpha C_\alpha x_\alpha. \tag{5.11}$$

Therefore, ϵ, being a linear combination of a large number of random variables $\{x_\alpha\}$, obeys Gaussian statistics (i.e. the probability distribution $P(\epsilon) \sim e^{-\beta\epsilon^2}$) according to the central limit theorem. The free energy for the fluctuation in the reaction coordinate, which is related (upon a constant) to the probability distribution by: $F(\epsilon) = -k_B T ln[P(\epsilon)]$ will therefore be parabolic. This treatment works whether or not $\{x_\alpha\}$ are Gaussian variables. The only criterion is that the environment couples linearly to the system. In the context of electron transfer reaction in polar solvent, this linear coupling regime corresponds to a system with a dielectrically unsaturated solvent, and therefore, the solvent will respond linearly to any change of the electronic states of the quantum system.

5.4 Relation between the reactant and product free energy surfaces

From the previous section, we know that the reaction coordinate (energy gap) obeys Gaussian statistics and the free energy surfaces are parabolic, in the limit of linear environments. Beside this parabolic nature of the free-energy surfaces, the free-energy curves were shown to obey a simple relation due to this unique definition of the reaction coordinate. It implies that, once we calculated the reactant free-energy surface as a function of the reaction coordinate, the product free-energy surface can be easily obtained. In this section, this simple relation will be presented.

Free-energy profiles as a function of the reaction coordinate for reactant and product can be written as

$$F_R(\epsilon_0) = A_R - k_B T ln[P_R(\epsilon_0)] \tag{5.12}$$

$$F_P(\epsilon_0) = A_P - k_B T ln[P_P(\epsilon_0)], \tag{5.13}$$

where $F_R(\epsilon_0)$ is the free-energy profile for the fluctuation of the reaction coordinate, A_R is the total free energy for the reactant electronic state and $P_R(\epsilon_0)$ is the probability distribution evaluated from the reactant potential surface. Similar set of definitions applies to the product case. The total free energy for the reactant and the product state can be obtained by phase space integration,

$$A_R = -k_BTln\int e^{-H_R(\{R_I\})/k_BT}\prod dR_I \tag{5.14}$$

$$A_P = -k_BTln\int e^{-H_P(\{R_I\})/k_BT}\prod dR_I. \tag{5.15}$$

From the above formulas, we can derive the relation between the free energy of reaction (ΔG^0) and the Marcus energy gap statistics,

$$\begin{aligned}\Delta G^0 = A_P - A_R &= -k_BTln\langle exp(-\frac{\epsilon(\{R_I\})}{k_BT})\rangle_R \\ &= k_BTln\langle exp(\frac{\epsilon(\{R_I\})}{k_BT})\rangle_P \end{aligned}\tag{5.16}$$

$\langle\cdots\rangle_R$ and $\langle\cdots\rangle_R$ correspond to the canonical average according to reactant and the product potential surface, respectively. $\epsilon(\{R_I\}) = H_P(\{R_I\}) - H_R(\{R_I\})$ is the Marcus energy gap for the ionic configuration $\{R_I\}$. The above relation shows that the free energy of reaction can be obtained without performing a full phase space integration, which is impossible in any sampling methods.

On the other hand, the free-energy profile difference between the product and reactant equals

$$\begin{aligned}F_P(\epsilon_0) - F_R(\epsilon_0) &= A_P - A_R - k_BTln\frac{P_P(\epsilon_0)}{P_R(\epsilon_0)} \\ &= -k_BTln\frac{\int\delta(\epsilon(\{R_I\})-\epsilon_0)e^{-H_P(\{R_I\})/k_BT}\prod dR_I}{\int\delta(\epsilon(\{R_I\})-\epsilon_0)e^{-H_R(\{R_I\})/k_BT}\prod dR_I} \\ &= -k_BTln\frac{\int\delta(\epsilon(\{R_I\})-\epsilon_0)e^{-\epsilon_0/k_BT}e^{-H_R(\{R_I\})/k_BT}\prod dR_I}{\int\delta(\epsilon(\{R_I\})-\epsilon_0)e^{-H_R(\{R_I\})/k_BT}\prod dR_I} \\ &= \epsilon_0 \end{aligned}\tag{5.17}$$

Equation 5.17 shows that the product and the reaction free-energy surfaces differ by

ϵ_0 at any value of ϵ_0. It means that once we get the reactant free-energy surface, the product free-energy surface can be easily obtained from the above relation. It also implies that the curvature of the two free-energy curves are identical at the same ϵ_0. Eq. 5.17 together with the parabolic approximation of the free-energy curves make the reorganization energy λ particularly important in studying electron-transfer reactions because the free-energy barrier ΔG^* of a reaction is related to the reorganization energy and the free energy of reaction ΔG^0 by,

$$\Delta G^* = \frac{(\Delta G^0 + \lambda)^2}{4\lambda}. \tag{5.18}$$

5.5 Previous studies of electron-transfer free energy surfaces using classical molecular dynamics

As already shown, the free energy surfaces are parabolic [116] and the energy gap, resulting from a combination of effects from the ions and the water molecules, obeys Gaussian statistics if the environment responds linearly to the electric field. There have been a number of classical molecular dynamic studies [19,20,111–114] supporting this assumption in the case of reactions between aqueous metal ions. For example, Fig. 5-3 shows the free-energy surfaces of ferrous-ferric self-exchange reaction taken from Ref. [114], using classical molecular dynamics with umbrella sampling.

Despite the qualitative consistency, quantitative agreement has not been achieved with classical force fields. The reorganization energy λ (i.e. the free energy cost to move from the equilibrium configurations of the product to those of the reactant without the transfer of electron) for the aqueous Fe^{2+}-Fe^{3+} self-exchange reaction was found to be 83.2 kcal/mol or 3.6 eV for ions 5.5 Å apart [114], while experimentally [115] (at the slightly shorter separation of 5.32 Å) it is found to be 2.1 eV. Although there have been studies of electron-transfer reactions including electronic polarization in classical force-field potentials [112,113], full first-principles studies are required to

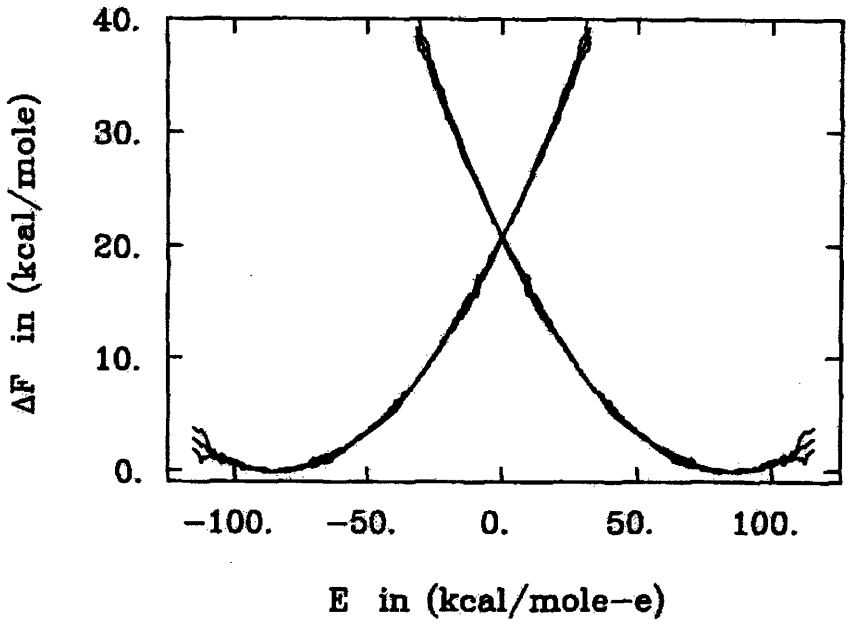

Figure 5-3: Diabatic free-energy surfaces for Fe^{2+}–Fe^{3+} electron transfer reaction calculated using classical molecular dynamics simulations when the ions are 5.5 Å apart. The figure is taken from Ref. [114]

describe realistically and quantitatively these reactions. Recently, an elegant grand-canonical density functional approach has been introduced to address this class of problems [21,22]. This approach is, however, targeted at half-reactions for a donor or an acceptor in contact with an electron reservoir, and the free energy surfaces and free energy barrier cannot be calculated using this approach. The need to qualitatively and quantitatively describe electron-transfer reaction has prompted us to explore the possibility of performing first-principles molecular dynamics studies of full electron-transfer reactions.

5.6 Static density-functional calculation of reorganization energy

In Marcus' original paper of electron transfer [2], a dielectric continuum treatment was suggested to calculate the reorganization energy contributions from the solvent (outer sphere contributions λ_{os}), assuming linear response of the environments to

the electric field. This original dielectric continuum treatment is in widespread use and can be sufficiently accurate, with the knowledge of the effective radii of the reactants. However, this method does not take into account the reorganization of the reactant molecules (inner sphere contribution λ_{is}) due to a change of oxidation states during electron transfer and this contribution can sometimes be significant. Theoretical approaches to estimate λ_{is} are surprisingly few, and the best approach is still a matter of debate. In a recent paper by Klimkans and Larsson [120,121], it was suggested that λ_{is} could be calculated in a convenient way from the total energies of the isolated reactant molecules in their ground and excited electronic states. In this section, we adopt this method to calculate λ_{is}, and together with the dielectric continuum treatment to obtain λ_{os}, we are able to compute the total reorganization energy for the ferrous-ferric self-exchange reaction.

In the case of iron ions solvated in water, the inner sphere can be taken to consist of the ion and the first solvation shell water molecules. As shown Fig. 5-4, the reorganization energy contributions are divided into the inner sphere (shaded regions) and outer sphere (the remaining region). λ_{is} is calculated using the isolated clusters of the iron with six water molecules, as it has been suggested experimentally [122,123] that both ferrous and ferric ions are six-fold coordinated in the first solvation shell by water molecules when solvated in water.

Fig. 5-5(a) shows schematically the procedure to calculate λ_{is} from first-principles. First, the ionic geometry of hexa-aqua ferrous cluster is optimized in vacuum. One electron is then removed from the system and we calculate the total energy of ferric ion in the optimized geometry of the ferrous ion cluster. A similar procedure is performed with the hexa-aqua ferric cluster and one extra electron is added to the system after ionic geometry optimization. λ_{is} can then be obtained from:

$$\lambda_{is} = E^{Fe^{3+}}[Fe^{2+}] + E^{Fe^{2+}}[Fe^{3+}] - E^{Fe^{2+}}[Fe^{2+}] - E^{Fe^{3+}}[Fe^{3+}] \qquad (5.19)$$

where $E^{Fe^{2+}}[Fe^{2+}]$ ad $E^{Fe^{2+}}[Fe^{3+}]$ are the total energies of ferrous or ferric ion in the optimized geometry of the ferrous ion cluster. Similar notations are used for

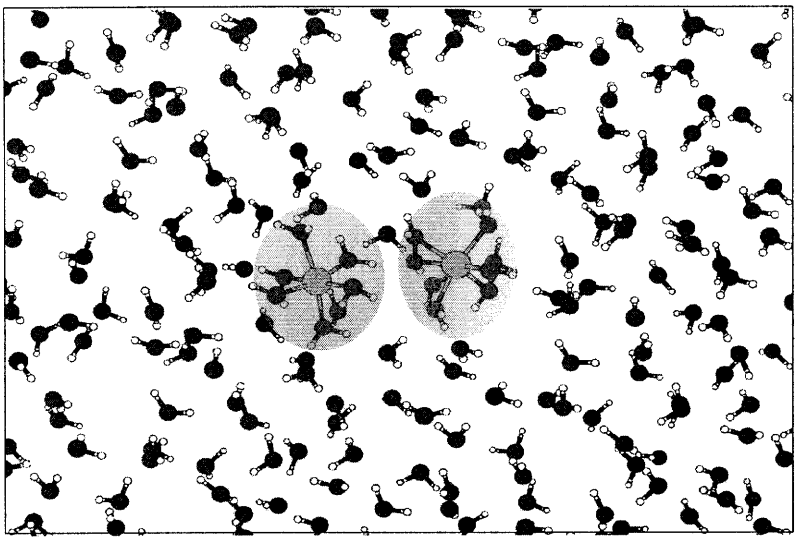

Figure 5-4: Schematic diagram showing the division of the reorganization energy contributions into inner and outer sphere.

$E^{Fe^{3+}}[Fe^{2+}]$ and $E^{Fe^{3+}}[Fe^{3+}]$. In most plane-wave codes employing periodic boundary conditions, comparing energies between systems with different charges always give errors due to the finite Coulomb interactions between periodic images. However, in the above procedure, these Coulomb interactions cancel out when calculating the difference in energies.

We performed these calculations in PWscf [61] using ultrasoft pseudopotentials for iron, oxygen and hydrogen atoms at PBE-GGA level. The ultrasoft pseudopotentials for O and H are from the standard PWscf distribution (H.pbe-rrkjus.UPF and O.pbe-rrkjus.UPF). We generated a 16-electron iron ultrasoft pseudopotential (Fe.pbe-sp-van_mit.UPF) using the Vanderbilt code [124]. Plane-wave cutoffs for wavefunction and charge density are 25 and 200 Ryd, respectively. The ion cluster is in a unit cell of side length 15.9 Å. Using the described procedure, the inner sphere contribution (λ_{is}) equals 0.50 eV.

The contributions to the reorganization energy from the outer solvent molecules can be estimated from the dielectric continuum model [2,116]. In this model, the ions and the first solvation shell water molecules are replaced by the conduction spheres with volumes approximately equal those occupied by the hexa-aqua iron clusters as

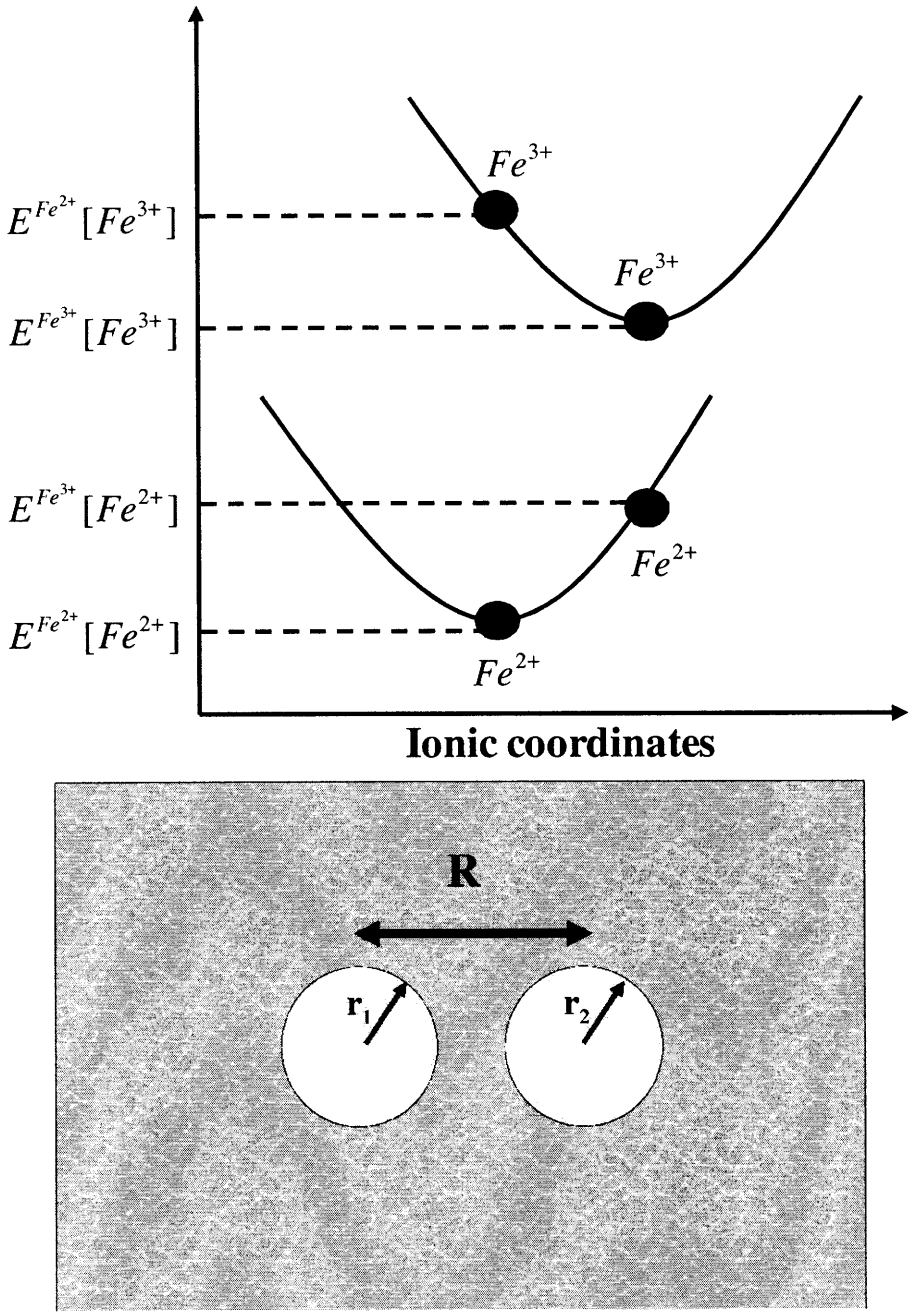

Figure 5-5: a) (upper panel) Procedure to calculate the inner sphere contributions to the reorganization energy using four separate first-principles calculations. b) (lower panel) Procedure to calculate the outer sphere contributions to the reorganization energy using the dielectric continuum theory. r_1 and r_2 are the radii of the sphere occupied by the ferrous and ferric ion clusters, respectively, taken as approximately the distance between the ion and the hydrogen atoms in the first solvation shell. R is the center to center distance between the two clusters.

shown in Fig. 5-5(b). λ_{os} can be calculated as,

$$\lambda_{os} = \frac{e^2}{4\pi\epsilon_0}(\frac{1}{2r_1} + \frac{1}{2r_2} - \frac{1}{R})(\frac{1}{\epsilon_\infty} - \frac{1}{\epsilon_{static}}) \tag{5.20}$$

where r_1 and r_2 are the radii of the sphere occupied by the ferrous and ferric ion clusters, respectively, taken as approximately the distance between the ion and the hydrogen atoms in the first solvation shell. R is the center to center distance between the two clusters. ϵ_∞ and ϵ_{static} are the optical and static dielectric constant of water. Taking r_1=2.66 Å, r_2=2.66 Å, R=5.5 Å, ϵ_∞=1.8 and ϵ_{static}=78, respectively, the outer sphere contribution, λ_{os}=1.54 eV.

The total reorganization energy ($\lambda=\lambda_{is}+\lambda_{os}$) equals 2.04 eV, which is in good agreement with the experimental value of 2.1 eV. However, this static calculation does not take into account the entropic effects. We cannot obtain the free energy surfaces of the reaction and therefore we cannot get the free energy barrier of reaction. Despite the deficiency of static calculations, it is a good indication that first-principles calculations can provide a better quantitative agreement to the experiments. In the next few sections, we will present a novel technique to calculate the electron-transfer free energy surfaces from first-principles molecular dynamics simulations and show the results of self-exchange reactions between aqua ferrous-ferric ions.

5.7 Calculating diabatic free energy surfaces from first-principles molecular dynamics

We argue in the following that state-of-the-art first-principles molecular dynamics calculations, together with several algorithmic and conceptual advances, are able to describe with quantitative accuracy these diabatic processes, while including the realistic description of the complex environment encountered. In this section, we present a novel technique to study full electron-transfer reactions from first-principles molecular dynamics, with ferrous-ferric self-exchange as a paradigmatic example. In all the molecular dynamics simulations discussed in this chapter, we use Car-Parrinello

molecular dynamics [23–25] and spin-polarized DFT in the PBE-GGA approximation. The ferrous and ferric ions are both in the high-spin states as confirmed by the literature [136, 137] and our own calculations. The ultrasoft pseudopotentials for Fe, O and H are the same pseudopotentials used in Section 5.6. The wavefunctions and charge density cutoffs are 25 and 200 Ryd, respectively. The deuterium mass was used in place of hydrogen mass to allow for a larger timestep of integration. The Car-Parrinello fictitious mass (μ) and the timestep are 450 a.u. and 5 a.u., respectively. A Nose-Hoover thermostat was used on the both electrons and ions. The ionic temperature was set at 400 K.

Fig. 5-6 shows schematically the sampling procedure used, following the lines of Ref. [114] for classical simulations. An ionic trajectory is first generated with the ions in the (2+r) and (3-r) states of charge, respectively. r is an "umbrella-sampling" parameter used to explore different regions of the phase space. We then perform two separate runs with the electronic state constrained in the reactant or in the product electronic configuration, and with the ions following the afore-generated ionic trajectories. The reaction coordinate ϵ at every timestep is thus given by the difference between the energies of the product and the reactant state. The probability distribution $P(\epsilon)$ is then calculated as:

$$P(\epsilon) = \frac{\sum_{\tau} \delta_{\epsilon'(\tau),\epsilon} exp\{-\beta[E_r(\tau) - E_s(\tau)]\}}{\sum_{\tau} exp\{-\beta[E_r(\tau) - E_s(\tau)]\}}, \tag{5.21}$$

where $\epsilon'(\tau) = E_p(\tau) - E_r(\tau)$ is the reaction coordinate at time τ; $E_r(\tau)$, $E_p(\tau)$ and $E_s(\tau)$ are the energies of the system in the reactant, product and sampling oxidation states, respectively, at time τ, and $\delta_{\epsilon'(\tau),\epsilon}$ is the Kronecker delta. The exponential term in the expression above restores the correct thermodynamical sampling according to the energy surface E_r. The free energy $F(\epsilon)$ is derived from the probability distribution $P(\epsilon)$ as $F(\epsilon) = -k_B T \ln(P(\epsilon))$.

It is of central importance to note that due to the lack of self-interaction correction in common exchange-correlation functionals, the transferring (3d minority spin) elec-

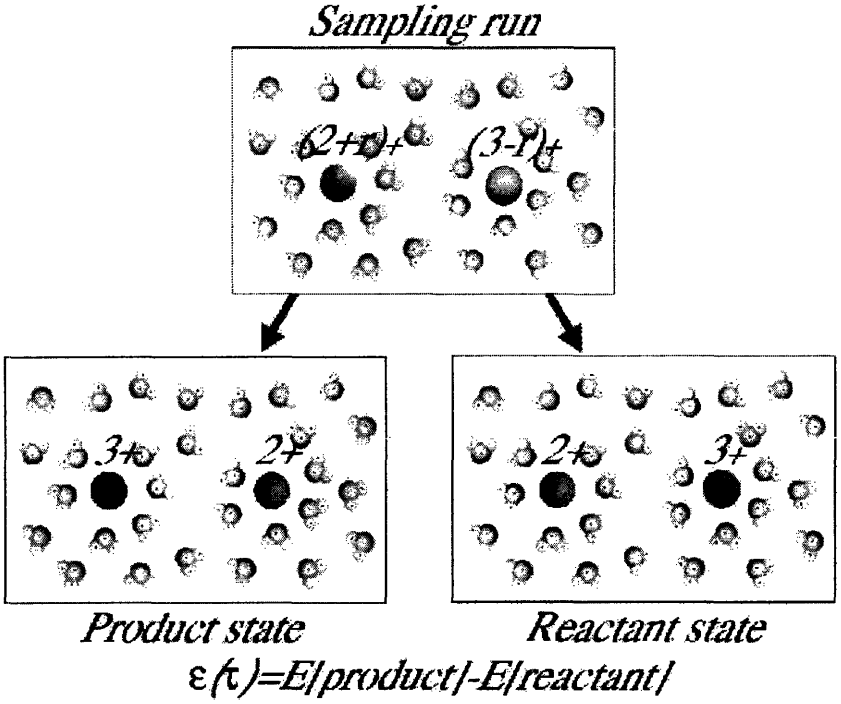

Figure 5-6: Procedure used to calculate the diabatic free energy surfaces for electron transfer from first-principles molecular dynamics: The reaction coordinate at each timestep is calculated from the energy difference between the product and reactant states in the ionic configuration provided by the sampling run. The phase space is explored via the umbrella sampling parameter r, determining the oxidation state of the ions.

tron will unphysically split between the two ions. Moreover, to calculate the energy gap, we need to accurately calculate the total energy when the minority spin electron localizes at either reactant or product site at any given ionic configuration. In order to address these central problems, we will consider two cases: 1) the case when two ions infinitely apart; 2) the two ion at a finite distance with the help of a penalty functional.

5.8 Special case when two ions infinitely apart

We first consider the simple case when oxidation states can be controlled trivially. This happens when two ions are infinitely apart; the two ions can be studied in separate simulation cells and the oxidation states are controlled by simply changing the

total number of electrons. For this special case, we performed runs using $Fe^{(2+r)+}$ and $Fe^{(3-r)+}$ (with r=0.0, 0.25, 0.50, 0.75 and 1.0), each solvated with 31 water molecules in the unit cell. We then carried out one Fe^{2+} and one Fe^{3+} run in the trajectory generated with $Fe^{(2+r)+}$, and one Fe^{2+} and one Fe^{3+} run in the trajectory generated with $Fe^{(3-r)+}$. Due to the symmetry of the reactant and product, the sampling ensembles of r=0 and 1 were from the same trajectories; similarly for r=0.25 and 0.75. (Also mentioned in Section 5.6, when calculating energies of charged systems in periodic-boundary conditions, the Coulomb interaction of charges with their periodic images should be removed [125]. In practice, these errors cancel out when calculating the energy gap, which is the difference in energy between systems with the same charge.)

The initial configuration for each simulation was prepared by replacing seven water molecules from the last configuration of a well-equilibrated 32 water molecules simulation at 400 K with an hexa-aqua iron ion. A re-scaling of the unit cell volume to 95% of the original size was needed to take into account of the difference in volumes occupied by seven water molecules and an hexa-aqua iron ion. A 5 ps equilibration run with the 31 water molecules and a ferrous ion was then carried out. The last ionic configuration of this equilibration run was taken as the initial configuration for each simulation with difference oxidation states for the ion. Each simulation has about 5 ps production run after 1 ps of thermalization. To access whether the systems prepared this way are well-equilibrated, Fig. 5-7 shows the Fe-O radial distribution functions for simulations with different ionic oxidation states. The black and the red curves show the radial distribution functions calculated from, respectively, the first and the second half of the 5 ps production runs. As seen in the figure, the solvation structures do not change significantly after 1 ps of thermalization. This observation is in good agreement with Bader *et. al.* [126] suggesting that a full relaxation happens within 1 ps after the change of oxidation state of aqueous iron ion.

Fig. 5-8 shows the resulting diabatic surfaces; the final result is obtained by integrating [127]

$$F(\epsilon) = \frac{\sum_r F_r(\epsilon) g_r(\epsilon)}{\sum_r g_r(\epsilon)}, \tag{5.22}$$

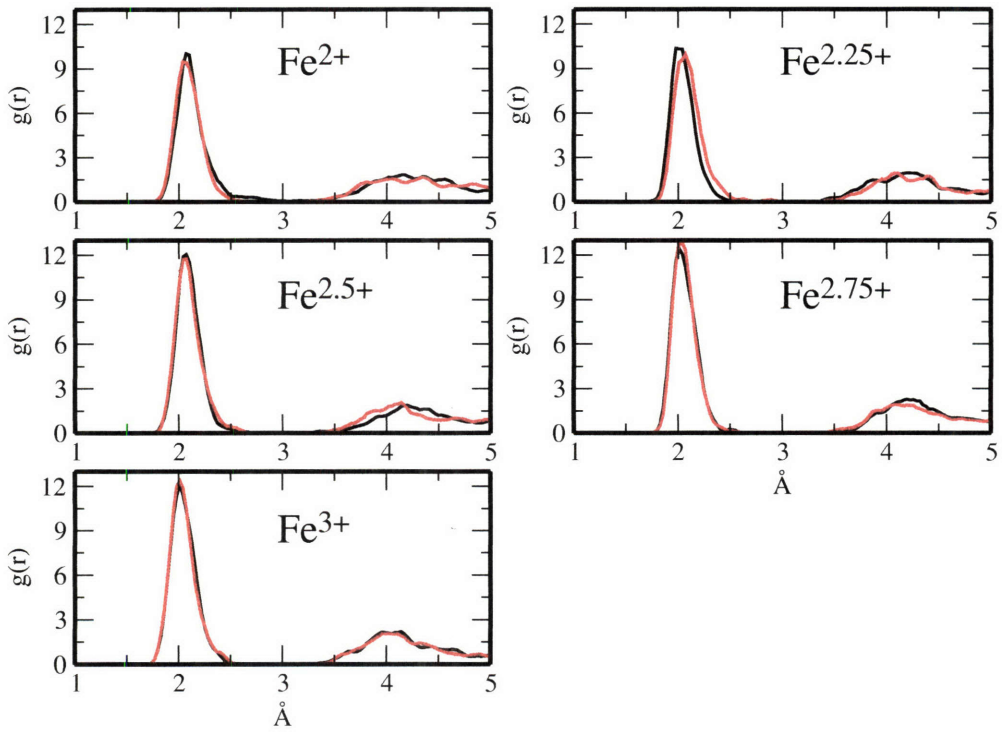

Figure 5-7: The Fe-O radial distribution functions for $Fe^{(2+r)+}$ solvated in water with r=0, 0.25, 0.5, 0.75, 1. Each simulation lasts about 5 ps after dropping the first 1 ps. The black and the red curves show the radial distribution functions calculated from, respectively, the first and the second half of different simulations.

where $F_r(\epsilon)$ is the slope of the free energy curve in the different sections, each characterized by an umbrella-sampling parameter r, and the weighting factor $g_r(\epsilon)$ is $\langle\delta(\epsilon - \epsilon(\tau))\rangle_r$. For this special case, the trajectories generated with $Fe^{(2+r)+}$ and $Fe^{(3-r)+}$ are independent; since each of them provides n data points, there will be n^2 energy gaps, providing high statistics and a very smooth free energy curve that fits accurately a parabola, with a coefficient of determination (R^2) of 0.9996, and a reorganization energy of 1.77 eV. Note that at the tail ends of each sampling region the statistical accuracy becomes lower - this explains the slight deviations from a parabola seen in Fig. 5-8.

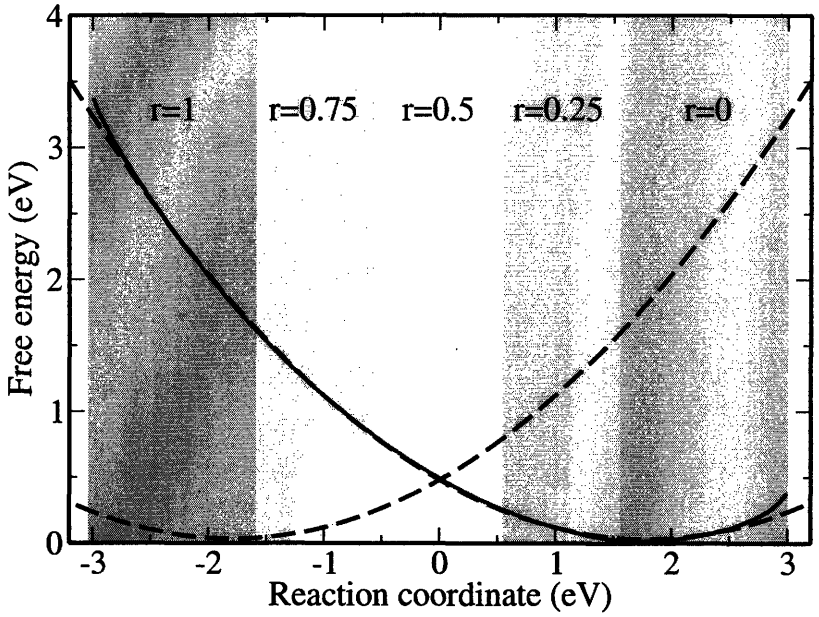

Figure 5-8: Diabatic free energy surfaces for ferrous-ferric electron transfer in the special case when two ions are infinitely apart. The solid curve has been obtained from first-principles molecular dynamics. The dashed curves are mirror images, and correspond to a parabolic fit of the data. Different shades indicate portions of the diabatic surface sampled with r=0, 0.25, 0.5, 0.75 and 1.

5.9 Penalty functional in controlling oxidation state

As mentioned earlier, the self-interaction errors of most exchange-correlation functionals result in a dramatic qualitative failure in describing ions in different oxidation states when more than one ion is present. This failure can be exemplified by the case of two iron ions in the 2+ and 3+ oxidation state in the same simulation cell. When such a system is studied – e.g. using PBE-GGA – the HOMO electron will split between the two iron centers, to decrease its own self-interaction, as exemplified in the case of two hexa-aqua ions putting side by side (Fig. 5-9). This behavior takes place irrespective of the chemical environment of the two iron centers; we observe it for two isolated atoms, two hexa-aqua iron complexes, or two ions fully solvated.

We will show in the following that this failure can be corrected by adding a

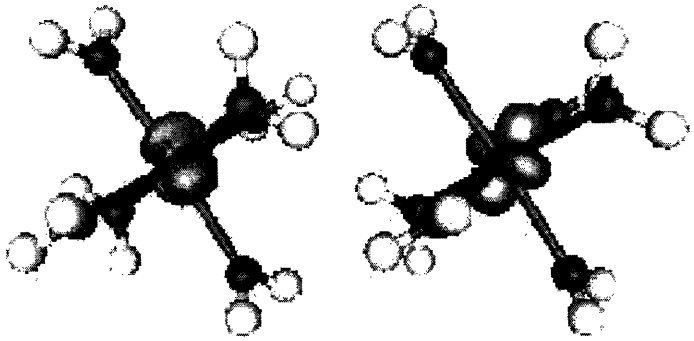

Figure 5-9: The HOMO orbital charge density distribution in the case when one hexa-aqua ferrous and one hexa-aqua ferric ions in the same unit cell. The minority spin electronic charge density (HOMO) splits between two ions due to the self-interaction.

penalty cost to ground states with non-integer occupation of the ion centers [128]. This same approach is also used to calculate the Marcus energy gap, where for a given configuration we need to determine both the correct ground-state energy (with the transferring electron in the reactant electronic configuration) and the first excited state (with the transferring electron in the product electronic configuration). We use and validate the following penalty functional

$$E[\{\psi_i\}] \rightarrow E[\{\psi_i\}] + \sum_I \frac{P^I}{\sigma_I\sqrt{2\pi}} \int_{-\infty}^{f_0^I - f_{\{\psi_i\}}^I} \exp(-\frac{x^2}{2\sigma_I^2})dx, \tag{5.23}$$

where $f_{\{\psi_i\}}^I$ is the largest eigenvalue of the minority-spin occupation matrix $(n_{mm'}^{I,\sigma})$ on ion I (calculated by projecting the minority-spin Kohn-Sham orbitals on the 3d atomic orbitals of iron in this work),

$$n_{mm'}^{I,\sigma} = \sum_i \langle\psi_i^\sigma|\phi_{m'}^I\rangle\langle\phi_m^I|\psi_i^\sigma\rangle. \tag{5.24}$$

ψ_i^σ are the Kohn-Sham orbitals and ϕ_m are the 3d atomic orbitals of iron. f_0^I is the target value of $f_{\{\psi_i\}}^I$. In the case of using ultrasoft pseudopotentials,

$$n_{mm'}^{I,\sigma} = \sum_i \langle\psi_i^\sigma|S(\{R_I\})|\phi_{m'}^I\rangle\langle\phi_m^I|S(\{R_I\})|\psi_i^\sigma\rangle, \tag{5.25}$$

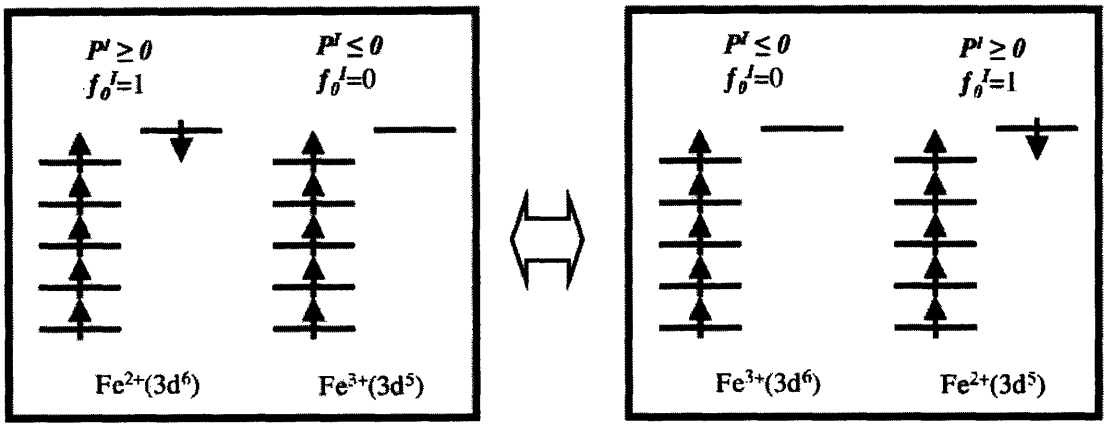

Figure 5-10: The transferring electron can be localized at the desired location with the appropriate sign of P^I and value of f_0^I.

where $S(\{R_I\})$ is related to the augmentation charge described in Section 2.6. There is no unique way to define the occupation matrix and the choice should depends on the systems studied. In this work, we chose to project the Kohn-Sham orbitals on the localized d-orbitals because this definition works well in systems with the transferring electron not taking part in any chemical bonding. Molecular orbitals, or Wannier functions can, instead, be used if the donor or acceptor ion is chemically bonded to the ligands.

Note that the definition of $f^I_{\{\psi_i\}}$ is independent of any unitary transformations on ψ_i^σ's or any definitions of the 3d atomic orbitals by forming linear combinations of ϕ^I_m. The penalty is in the form of a step function with the smearing relating to the value of σ. When $P^I > 0$, a big penalty will be incurred on the total energy if $f^I_{\{\psi_i\}}$ is smaller than f^I_0. Therefore, the ion is forced to have $f^I_{\{\psi_i\}} > f^I_0$. Similarly, if $P^I < 0$, $f^I_{\{\psi_i\}} < f^I_0$. By changing the sign of P^I and the target value f^I_0 on each reaction site, the transferring electron, i.e. the minority spin d-electron in the case of ferrous-ferric self-exchange, can be forced to localized at the desired site (Fig. 5-10). With the same scheme, a fraction of the electron, instead of the whole one, can also be localized at one site or the other and this fractional charge localization will be useful for umbrella sampling.

In performing molecular dynamics, the wavefunctions and ions evolve according

to the new equations of motion,

$$-m_I\frac{d^2R^I}{dt^2} = \frac{dE[\{\psi_i\}]}{dR^I}+\sum_I\frac{P^I}{\sigma_I\sqrt{2\pi}}exp[-\frac{(f_0^I-f^I_{\{\psi_i\}})^2}{2\sigma_I^2}](-\frac{df^I_{\{\psi_i\}}}{dR^I}), \quad (5.26)$$

$$-\mu_I\frac{d^2\psi_i}{dt^2} = \frac{dE[\{\psi_i\}]}{d\psi_i^*}+\sum_I\frac{P^I}{\sigma_I\sqrt{2\pi}}exp[-\frac{(f_0^I-f^I_{\{\psi_i\}})^2}{2\sigma_I^2}](-\frac{df^I_{\{\psi_i\}}}{d\psi_I^*}). \quad (5.27)$$

$f^I_{\{\psi_i\}}$ can be written as,

$$f^I_{\{\psi_i\}}=\sum_{m,m'}U^+_{5,m}n^{I,\sigma}_{m,m'}U_{m',5}, \quad (5.28)$$

where the unitary matrix U_{hl} diagonalized $n^{I,\sigma}_{m,m'}$ and the eigenvalues are arranged in the ascending order. The forces on ions are calculated from the new total functional from the Hellmann-Feynman theorem.

$$-m_I\frac{d^2R^I}{dt^2} = \sum_i\langle\psi_i|\frac{d\hat{H}}{dR^I}+\sum_I\frac{P^I}{\sigma_I\sqrt{2\pi}}exp[-\frac{(f_0^I-f^I_{\{\psi_i\}})^2}{2\sigma_I^2}]$$
$$\times\ (-\sum_{m,m'}U^+_{5,m}\frac{d|S(\{R_I\})|\phi^I_{m'}\rangle\langle\phi^I_m|S(\{R_I\})|}{dR^I}U_{m',5})|\psi_i\rangle). \quad (5.29)$$

$\hat{H}$ is the Hamiltonian corresponding to the original DFT functional. In this expression, both the augmentation factor $S(\{R_I\})$ and the atomic orbital ϕ^I_m depends analytically on R^I, the positions of the ions.

In practice, when the ions are solvated in water, the electronic structure as well as the occupation numbers are expected to be altered by the solvation process. To determine the optimal parameters used in the penalty functional, the reference states, at which the electronic structure should resemble the case of full solvation, were studied. In this case, we separately calculated the minority-spin occupation matrix for either a ferrous or a ferric hexa-aqua ion embedded in a dielectric continuum (ϵ=78) [129]. Then, we determine the parameters in the penalty functional applied on the ions so that the occupation matrices of the ferrous or ferric clusters are accurately reproduced once the two are studied in the same unit cell. In this case, we got P^I=0.54 eV, f^I_0=0.95 and σ_I=0.01 on the ferrous ion and P^I=-0.54 eV, f^I_0=0.28 and σ_I=0.01 on the ferric ion. We note that the target occupations for the minority-spin are not

chosen exactly one or zero, since the orbital hybridization between the iron $3d$ orbitals and the lone pairs of the water molecules contributes to the projection onto atomic orbitals. The contributions to the total energy from the penalty functional are close to zero on the ferrous ion and close to -0.54 eV on the ferric ion. When calculating the energy gap, these contributions are taken away from the total energy; in any case, these effects are negligible since these contributions cancel out when calculating energy differences. Different constraints or penalties have been recently implemented in density-functional calculations [130–132]; we found our choice particularly robust, but several variations on the theme can be envisioned.

5.10 Validations of the penalty functional

A first, qualitative validation of this penalty functional is performed examining the charge density obtained by subtracting from a calculation with a ferrous and a ferric hexa-aqua ion in the same unit cell that of an isolated ferrous hexa-aqua ion, and that of a ferric hexa-aqua ion (the hexa-aqua ions were 10 Å apart and a dielectric continuum surrounds the two clusters to remove long-range electrostatic interactions between them). The charge density difference is shown in Fig. 5-11.

As anticipated before, in the absence of a penalty functional, the transferring electron splits between the two ions; once the penalty functional is applied, the charge density around the ions reorganizes itself so that it produces a charge density that is the exact superposition of that obtained from the two independent calculations.

We can make the validation quantitative by calculating the energy gap for the system described, using two penalty-functional calculations that impose to the HOMO electron to localize first on one, then on the other ion. This energy gap can also be calculated exactly with PBE-GGA using the "4-point" approach [120,121], provided again that all long-range electrostatic interactions are screened out. The four calculations involve Fe^{2+} in two $Fe(H_2O)_6$ geometries (A and B), and Fe^{3+} in the same geometries; the energy gap is $[E_A(Fe^{2+}) + E_B(Fe^{3+}) - E_B(Fe^{2+}) - E_A(Fe^{3+})]$. The calculation follows the same idea as the computation of λ_{is} in Section 5.6. We choose

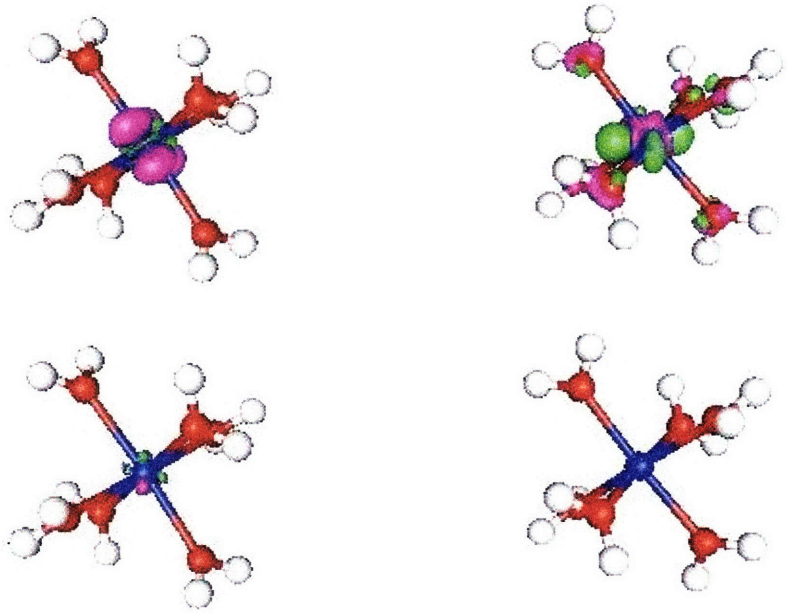

Figure 5-11: Charge density difference compared to DFT ground state charge density (calculated from ferrous and ferric ion clusters in separate cells), without (above) and with (below) penalty functional. The difference is large without the penalty functional. With the penalty functional, the difference compared to DFT ground state is minimal. The contours are plotted at 70% of the maximum density difference of the one with penalty functional. The maximum value with penalty functional is 8.8% of that without penalty functional.

Table 5.1: The energy gaps calculated with the penalty functional and the "4-point" approach for different random cluster geometries.

	Penalty functional (eV)	"4-point" (eV)
I	0.632	0.622
II	0.569	0.542
III	0.769	0.769
IV	1.027	1.012

one configuration in which the hexa-aqua ions are fully relaxed, and three carved out from random steps in the molecular dynamics simulations. Table 5.1 shows the energy gaps calculated with the penalty functional and with the "4-point" method. The energy gaps obtained with the penalty are in excellent agreement with the "4-point" values. It is worth mentioning that the energy gap is an excited-state property of the

system, and thus in principle outside the scope of density-functional theory, which is a ground-state theory. However, since charge densities of the HOMO and LUMO do not overlap, we can argue that all that is required is a description of the charge density that is locally correct (the excited state has an electron locally in equilibrium around an iron, oblivious of the other iron ion where it could sit more favorably). A more formal justification can be offered on the basis of "nearsightedness" in electronic matter [133, 134].

5.11 Diabatic free energy surfaces when two ions at finite distance apart

With these tools, we determined the diabatic free energy surfaces for two iron ions separated by 5.5 Å and solvated in 62 water molecules, in periodic boundary conditions. 5.5 Å was suggested [37, 135] to be the optimal distance for electron transfer. The initial configuration for the simulations were prepared by carving out two spheres, each containing seven water molecules, from the last configuration of a well equilibrated 64 water molecules simulations at 400 K and replacing them by two hexa-aqua iron ions, 5.5 Å apart. An equilibration run of 7 ps was then performed without the penalty functional. The sampling runs with different r were carried out from the last configuration of this equilibration run. Each sampling run has about 4.5 ps production time after 1 ps of thermalization. We show our results in Fig. 5-12, together with a parabolic fit to the data. Different color shades indicate portions of the diabatic surface sampled r=0, 0.5 and 1. The reorganization energy (λ) that we obtain is 2.0 eV, in excellent agreement with the experimental value of 2.1 eV [115]. The energy barrier $\Delta G \approx$0.49 eV, about a quarter of λ, as expected if the free-energy surfaces are parabolic.

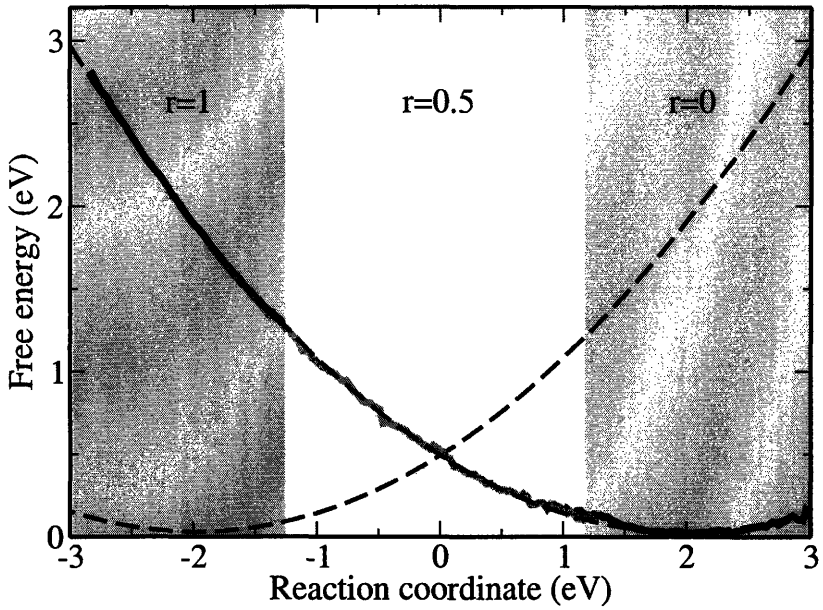

Figure 5-12: Diabatic free energy surface for ferrous-ferric electron transfer when the two ions are 5.5 Å apart. Different color shades indicate portions of the diabatic surface sampled r=0, 0.5 and 1. The right dashed curve is the parabolic fit of the data and the left dashed curve its mirror image.

5.12 Conclusions

In conclusion, we have demonstrated how it is possible to obtain Marcus diabatic surfaces from first-principles molecular dynamics, where the entire system is treated quantum-mechanically, with the accuracy and predictive power that this approach entails. The case when two ions are at a finite distance requires special care in dealing with self-interaction errors and excited-state energies. In response to these challenges, we developed and validated a penalty functional that is able to control the oxidation states of ions, and that describes accurately both the electronic ground state and the first excited state where the electron is transferred to the other ion. This approach can be successfully applied to a wide class of oxidation-reduction reactions, in solution (as it often happens in electrochemistry or biochemistry) or in the solid-state (intervalence charge-transfer).

Chapter 6

Conclusions

In this thesis, we performed extensive studies of the structural and dynamical properties of water at ambient and supercritical conditions, and electron-transfer reactions in aqueous systems from first-principles. At the DFT-PBE level, the structural, vibrational and energetic properties of the monomer and dimer are found in good agreement with the experimental results. In particular, the dimer binding energy agrees very well with the experimental value, showing that the energy functionals describe well the hydrogen bonding in water. Despite this excellent agreement, we found that first-principles molecular dynamics simulations of water at room temperature and pressure produce water at glassy states after a careful choice of small enough electronic fictitious mass and long enough equilibration of more than 10 ps [28].

Water starts to become truly liquid-like when temperatures reach 400 K. The causes to this ~100 K discrepancy in the freezing point can be various. The effects of the finite cell size of the simulations were shown to be negligible in our simulations with 32 water molecules. The two major causes are believed to be the choice of the exchange-correlation functional and the quantum-mechanical nature of the intramolecular (and of some high-frequency intermolecular) vibrational modes. Those modes should obey Bose-Einstein statistics but are not well described in our first-principles simulations, in which the ions are treated as classical particles.

We have investigated further the structure of normal and supercritical water with combined experimental and theoretical efforts, studying the X-ray Compton scat-

tering profiles. We proposed that the Compton profile difference with respect to a reference state is a robust measure of the hydrogen bonding structure, and in particular the average number of hydrogen bonds per molecule. Formation of hydrogen bonds by valence electrons leading to localization in real space is thus detected in momentum space as a broadening of the corresponding Compton profile. This unique sensitivity to outer electrons and thus to intermolecular interaction and to hydrogen bonding is a special characteristic of Compton scattering. By studying a simple cluster of five water molecules, we found that there is a linear relation between n_e of the profile differences and the number of hydrogen bonds per molecule. This relation is also well-obeyed by the Compton profile differences computed from our first-principles simulations with a scaling factor of 73% at various conditions (from ambient to supercritical conditions). In particular, we found that the number of hydrogen bonds per molecule at the supercritical condition is still significant, solving the long-standing controversy of whether there is significant hydrogen bonding network at supercritical conditions.

The study of structural and dynamical properties of pure water at ambient and supercritical conditions has provided the basis to study electron-transfer reactions in aqueous systems. We developed a novel method to calculate free-energy surfaces from first-principles molecular dynamics using umbrella sampling, and by controlling the oxidation states of ions. Due to the self-interaction problem in common DFT functionals and the need to perform excited state calculations to sample the reaction coordinate, no one, to our knowledge, has ever calculated the free-energy surfaces of a full electron-transfer reaction from first-principles. We first considered the case when two ions are infinitely apart, in which the oxidation states of the ions can be controlled trivially. We found that the free-energy curves are parabolic, validating the linear solvation model as first proposed by Marcus [2]. To study electron-transfer reactions between the ions at finite distance apart, we introduced a penalty functional, which solves both the self-interaction error and the excited state challenge.

With the ferrous-ferric self-exchange reaction as a paradigmatic example, we calculated the free-energy surface, when the ions are at 5.5 Å apart, fully from first-

principles. The reorganization energy is in good agreement with the experimental value, a great improvement in quantitatively describing electron-transfer reactions. It is hoped that this approach will allow more and more studies of such reactions from first-principles, since it can be successfully applied to a wide class of oxidation-reduction reactions, in solution (as it often happens in electrochemistry or biochemistry) or in the solid-state (intervalence charge-transfer).

THIS PAGE INTENTIONALLY LEFT BLANK

Appendix A

DFT + Hubbard U

A.1 Introduction

In studying strongly correlated electronic systems, LDA functionals usually fail to correctly describe the electronic structure due to the inhomogeneity of the electron gas. Improvements can be achieved using GGA functionals which provide better results on systems with inhomogeneous charge densities. Despite these improvements, GGA functionals still fail to correctly describe several physical properties in transition metal compounds, from magnetic order to metallic-versus-insulating behaviors [138]. The large correlations of strongly localized d-electrons cannot be correctly described by GGA functionals.

The main idea proposed by the DFT + Hubbard U method is to correct the standard DFT approach in order to be able to better describe strong electronic correlations in the d or f-electrons. We have to go beyond the electron gas approximation used to model electron-electron interactions. Strongly-correlated materials (usually systems with partially filled d or f-valence shells) have their d or f-electrons feeling strong Coulomb repulsions in the presence of another localized electron, and the electron motion is known to be "correlated" due to this Coulomb interaction. The band structure calculations are not the best approach to observe this physical behavior, as they are manifestation of a one body problem, whereas correlation is a many-body property. Moreover, the exchange-correlation functionals, even in the case of GGAs,

are built from the near-homogeneous electron gas so that interactions are treated in a mean-field approach, which cannot accurately describe correlations between electrons.

The Hubbard model [139] has a long history in studying strongly correlated electronic systems in the condensed matter community. The Hubbard model is of the form

$$H_{Hub} = \sum_{\langle i,j \rangle} \sum_{l,l'} t_{i,j} c^{+}_{i,l} c_{j,l'} + \frac{U}{2} \sum_{i} \sum_{l,l'} n_{i,l} n_{i,l'}, \tag{A.1}$$

which contains the hopping term and the on-site repulsion term. i and l are the site and the orbital indexes, respectively. However, since the model is too simplified and the hopping amplitudes t and on-site repulsion U are unknown, the model cannot allow us to obtain accurate numerical results. Owing to the difficulties in the direct use of the model, a number of methods were proposed [140–144]. The main idea they all have in common is to use some hints from the many-body formalism to correct for DFT and to go beyond the mean field approach. One of the most popular methods in this family is the DFT + Hubbard U approach [38, 39], which was shown to be a simple and effective way to describe strongly correlated systems from first-principles.

In this appendix, the formalism of a simplified and rotational invariant DFT + Hubbard U scheme developed by Cococcioni *et. al.* [145] is discussed. The Hubbard U value, which describes the strength of the correlation, can be obtained from first-principles using a linear response approach [146]. We then discuss in details our integration of this DFT + Hubbard U scheme in the Car-Parrinello molecular dynamics. This implementation allows finite temperature studies of transition materials. With this tool, we investigate the effects of Hubbard U corrections on the solvation structure of the ferrous and ferric ions and the energetics of the electron-transfer reactions.

A.2 The Hubbard U term

The formal expression of the DFT + Hubbard U energy functional is adapted from the Hubbard model that deals with strongly correlated materials. In this model, a small

number of localized orbitals is selected and the electronic correlation associated to them is treated in a special way. In order to account explicitly for the on-site Coulomb interaction not treated faithfully within DFT, Anisimov *et. al.* [38, 39] proposed to correct the standard functional adding Hubbard-like interaction E_U:

$$E_{DFT+U}[n] = E_{DFT}[n] + E_U[n^{I,\sigma}_{m,m'}], \tag{A.2}$$

where $E_U[n^{I,\sigma}_{m,m'}]$ is the Hubbard functional for on-site interactions, dependent on the occupation matrix of the strongly correlated electrons.

A.2.1 Localized orbital occupations

In order to fully define how this approach works, we first have to select the degrees of freedom on which the Hubbard U acts on. These degrees of freedom are described by the matrix $n^{I,\sigma}_{m,m'}$. Although it is usually straightforward to identify in a given system the atomic levels to be treated in a special way (the d-electrons in transition metals and the f ones in the rare earths and actinides series) there is no unique or rigorous way to define the occupation of localized states in condensed phase due to the possible bond formations. E.g., besides projecting on the normalized atomic orbitals, it is equally legitimate to calculate $n^{I,\sigma}_{m,m'}$ by projecting on Wannier functions on Mullikan populations, or on integrated values in (spherical) regions around the atoms of the angular-momentum decomposed charge densities. Taking into account the arbitrariness in the definition of $n^{I,\sigma}_{m,m'}$, no particular significance should be attached to any of them (or other that could be introduced). The usefulness and reliability of an approximate DFT + Hubbard U method should be judged from its ability to provide a correct physical picture of the systems under study irrespective of the details of the formulation, once all ingredients entering the calculation are determined consistently.

All the above-mentioned definitions for the occupation matrices can be put in the

generic form

$$n^{I,\sigma}_{mm'} = \sum_i f_i^\sigma \langle \psi_i^\sigma | P^I_{m,m'} | \psi_i^\sigma \rangle, \tag{A.3}$$

where ψ_i^σ is the Kohn-Sham wave function corresponding to the state i with spin σ of the system and f_i is the corresponding occupation number. $P^I_{m,m'}$ are generalized projection operators on the localized-electron manifold. When using Γ-point sampling (as in the case of Car-Parrinello molecular dynamics), the k-point dependence of the Kohn-Sham wavefunction is discarded. In particular, $P^I = \sum_m P^I_{m,m'}$ is the projector on the complete manifold of localized states associated with atom at site I and therefore

$$n^{I,\sigma} = \sum_m n^{I,\sigma}_{mm} = \sum_i f_i^\sigma \langle \psi_i^\sigma | P^I | \psi_i^\sigma \rangle \tag{A.4}$$

is the total localized-states occupation for site I.

In the applications discussed in this work, we will define localized-level occupation matrices projecting onto atomic wavefunctions. This particular choice has been shown to accurately describe a wide range of transition metal materials [145, 150–152]. The projector operators are therefore simply

$$P^I_{m,m'} = S(\{R_I\}) | \phi^I_{m'} \rangle \langle \phi^I_m | S(\{R_I\}), \tag{A.5}$$

where ϕ^I_m is the valence atomic orbital with angular momentum component $|lm\rangle$ of the atom sitting at site I (the same wave functions are used for both spins). In the case of iron ions, the valence orbitals are the localized d-orbitals of iron atom and l=2. Since we will be using ultrasoft pseudopotentials to describe valence-core interaction, the augmentation charge operator $S(\{R_I\})$ (defined in Eq. 2.23) is needed to describe the orthogonality in presence of charge augmentation.

A.2.2 A simplified rotationally invariant scheme

The Hubbard U functional ($E_U[\{n^{I,\sigma}_{m,m'}\}]$) is written as [145]

$$E_U[\{n^{I\sigma}_{mm'}\}] = E_{Hub}[\{n^{I,\sigma}_{mm'}\}] - E_{dc}[\{n^{I,\sigma}\}]. \tag{A.6}$$

$E_{Hub}[\{n^I_{mm'}\}]$ corresponds to the on-site interactions between the correlated electrons. $E_{dc}[\{n^I_{mm'}\}]$ is then subtracted in order to avoid double counting of the interactions contained both in $E_{Hub}[\{n^I_{mm'}\}]$, and in some average way, in DFT. In $E_{dc}[\{n^I\}]$, the total, spin-polarized, occupation of the localized manifold is used: $n^{I,\sigma} = \sum_m n^{I,\sigma}_{mm}$.

To derive the expression of $E_U[\{n^{I,\sigma}_{m,m'}\}]$, we write the on-site interaction in terms of the occupation number, λ_m (i.e. eigenvalues of the occupation matrix $n^{I,\sigma}_{mm'}$),

$$E_{Hub}[\{n^I_{mm'}\}] = \frac{U'}{2}\sum_{I,\sigma}\sum_{m,m'}\lambda^{I,\sigma}_m\lambda^{I,-\sigma}_{m'} + \frac{U}{2}\sum_{I,\sigma}\sum_{m\neq m'}\lambda^{I,\sigma}_m\lambda^{I,\sigma}_{m'} \tag{A.7}$$

In calculating $E_{dc}[\{n^{I,\sigma}\}]$, this interaction is expressed in a mean-field way by writing:$N^{I,\sigma} = \sum_m \lambda^{I,\sigma}_m$,

$$E_{dc}[\{n^{I,\sigma}\}] = \frac{U'}{2}\sum_{I,\sigma}N^{I,\sigma}N^{I,-\sigma} + \frac{U}{2}\sum_{I,\sigma}N^{I,\sigma}(N^{I,\sigma}-1) \tag{A.8}$$

Therefore, to calculate $E_U[n^{I,\sigma}_{m,m'}] = E_{Hub}[\{n^{I,\sigma}_{mm'}\}] - E_{dc}[\{n^{I,\sigma}\}]$, the first term in $E_{Hub}[\{n^{I,\sigma}\}]$ and $E_{dc}[\{n^{I,\sigma}\}]$ cancels each other and it gives,

$$\begin{aligned} E_U[\{n^{I,\sigma}_{m,m'}\}] &= \frac{U}{2}\sum_{I,\sigma}[\sum_m \lambda^{I,\sigma}_m - \sum_m (\lambda^{I,\sigma}_m)^2] \\ &= \frac{U}{2}\sum_{I}[\sum_{m,\sigma} n^{I,\sigma}_{mm} - \sum_{m'} n^{I,\sigma}_{mm'}n^{I,\sigma}_{m'm}] \\ &= \frac{U}{2}\sum_{I,\sigma} Tr[n^{I\sigma}(1-n^{I,\sigma})] \end{aligned} \tag{A.9}$$

As seen from Eq. A.9, the Hubbard U functional introduce a penalty, tuned by the value of the U parameter, for partial occupation of the localized orbitals and thus favors full occupation (λ=1) or empty orbitals (λ=0). The obtained results strongly depend on the definition of the localized orbitals and on the choice of the interaction parameters used in the calculation, that should be determined in an internally consistent way, instead of determining the value of the electronic couplings by seeking a good agreement of the calculated properties with the experimental results in a semi-empirical way. Cococcioni *et. al.* [146] proposed that the value of U can actually be

calculated consistently from first-principles and we will devote the next two sections discussing this.

A.3 Physical meaning of the Hubbard correction

Consider an atom in contact with a reservoir of electrons that can only exchange an integer number of electrons with the reservoir. This means that intermediate situations with fractional occupations of one (or more) of its orbital may only arise, in the open atomic system, as time averages over states with integer number of electrons on the atomic orbitals. In quantum mechanics an open system with a fluctuating number of electrons is described not only by a pure-state wavefunction, but rather by a statistical mixture so that, for instance, the total energy is given as:

$$E_n = (1-\omega)E_N + \omega E_{N+1} \tag{A.10}$$

where E_N and E_{N+1} are the energies of the systems with N and $N+1$ electron respectively, and ω represents the statistical weight of the state with $N+1$ electrons. The average number of electrons will be $N+\omega$ so that the total energy of this open atomic system is represented by a series of straight-line segments joining states corresponding to integer occupations of the atomic orbitals (Fig A-1). The slopes of the line segments are the eigenvalues of the states getting filled,

$$\epsilon_i = \frac{dE}{dn_i} \tag{A.11}$$

Density-functional theory with exact-exchange correctly reproduces this behavior [147, 148], which is instead not well described by common DFT approaches that reproduces a total energy with unphysical curvature for non-integer occupations and spurious minima in correspondence of fractional occupation of the orbital of the atomic system, as seen in Fig. A-1. The unphysical curvature is associated with the incorrect treatment by DFT of the self-interaction of the partially occupied Kohn-Sham orbital, that gives a nonlinear contribution to the total energy with respect to orbital

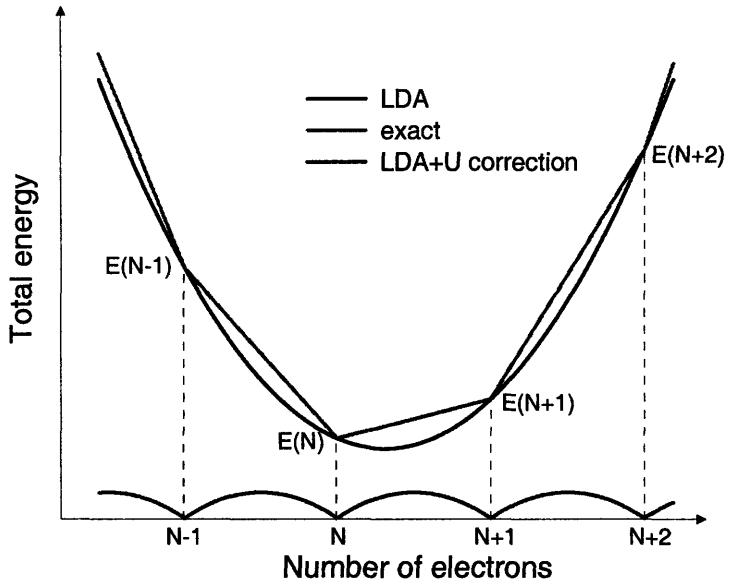

Figure A-1: The total energy profile as a function of the number of electrons in the system. The curve at the bottom is the correction due to Eq. A.9. The correct potential profile consists of segments of straight lines that flavor integral occupations. This figure is adopted from Ref. [145].

occupation (mainly a quadratic term coming from the Hartree energy that is not canceled properly in the exchange-correlation term). However, it is well known [149] that total energy differences between different states can be quite accurately reproduced by the DFT approach, if the occupation of the orbitals have integer values. We can recover the physical situation of an approximately piecewise linear total energy curved by adding a correction to the DFT total energy which vanishes for integer number of electrons and eliminates the curvature of the DFT energy profile in every interval with fractional occupations (bottom curve of Fig. A-1). This is exactly the kind of correction that is provided by Eq. A.9 if the numerical value of the parameter U is set equal to the curvature of the DFT energy profile. This understanding offers a way to obtain the value of U from first-principles without resorting to fitting with some experimental results.

A.3.1 Calculation of U from the linear response approach

As discussed in the previous section, the Hubbard U functional corrects for the spurious curvature due to the incomplete cancellation of the self interactions in the DFT total energy with respect to the number of localized electrons. The second derivative of the total energy ($\frac{\partial^2 E^{DFT}}{\partial (n^I)^2}$) corresponds to the effective curvature of the DFT total energy. However this quantity does not equal the Hubbard U. In fact, if we perturb a non-interacting system, we will still obtain a quadratic behavior of the total energy as a function of occupation. It is because the imposed occupation variation changes the kinetic energy of the system. This kinetic energy variation should not be included in the calculation because it is not originated from the electron-electron interactions. Because of this, the effective Hubbard U should be calculated as [145],

$$U = \frac{d^2 E^{DFT}}{d(n^I_{loc})^2} - \frac{d^2 E^{DFT}_0}{d(n^I_{loc})^2} \tag{A.12}$$

where the second derivative of E^{DFT}_0 is the above-mentioned independent electrons contribution to be subtracted from the full curvature of the DFT functional. n^I_{loc} is the total occupation of the localized orbitals, which can be calculated from the trace of the occupation matrix. However, it is not convenient to constrain the total localized orbitals occupation in actual calculations, and the occupation is forced to vary by adding to the DFT functional a localized perturbation.

$$E[\{\alpha\}] = \min_{n(r)} \{E[n^I_{loc}] + \alpha n^I_{loc}\} \tag{A.13}$$

This new functional is α dependent and we can switch to an occupation-dependent energy functional by a Legendre transformation,

$$E[\{n^I_{loc}\}] = \min_{\alpha} \{E[\alpha] - \alpha n^I_{loc}\}. \tag{A.14}$$

From this equation, the double derivative of the total energy with respect to the occupation can be easily obtained,

$$\frac{dE[n^I_{loc}]}{dn^I_{loc}} = -\alpha[n^I_{loc}] \tag{A.15}$$

$$\frac{d^2E[n^I_{loc}]}{d(n^I_{loc})^2} = -\frac{d\alpha[n^I_{loc}]}{dn^I_{loc}}. \tag{A.16}$$

In actual calculation, the quantity accessible is the response function: $\chi = \frac{dn^I_{loc}}{d\alpha}$ and the Hubbard U value equals

$$U = -\frac{d\alpha[n^I_{loc}]}{dn^I_{loc}} + \frac{d\alpha[n^I_{loc}]}{dn^I_{d,0}} = (\chi_0^{-1} - \chi^{-1}) \tag{A.17}$$

In Eq. A.17, the fluctuation of the localized orbital occupation, $n^I_{d,0}$, which defines the bare response function χ_0, is calculated without including the effects of the electron-electron interactions. In practice, a well-converged DFT (U=0, α=0) calculation is first performed in PWscf. Starting from that self-consistent potential and the corresponding electronic wavefunctions, a series of potential shifts (α) are added on the localized orbitals, and then we let the system evolve to self-consistency each time. The response functions χ_0 and χ are obtained numerically from the variation of $n^I_{d,0}$ and n^I_{loc} with respective to α. At the first iteration of the perturbed run only the bare perturbation is included in the effective potential acting on the electrons. It means that the density response obtained at the first iteration does not involve any effects of the electron-electron interactions and we can obtain $n^I_{d,0}$ and χ_0 from the first iteration of the perturbed runs; the interacting response function χ is instead calculated at the self-consistent stage.

However, this value of U, calculated in the reference state at U=0 eV, may not be the true value we want, as suggested by Kulik *et. al.* [152]. They instead suggested an internally-consistent approach to obtain the true U value. According to Ref. [152],

we can write out the quadratic part of the DFT + Hubbard U functional,

$$E_{quad} = \frac{U_{true}}{2} \sum_{i,\sigma} \lambda_i^{I,\sigma} (\sum_j \lambda_j^{I,\sigma} - 1) + \frac{U_{in}}{2} \sum_i \lambda_i^I (1 - \lambda_i^I). \tag{A.18}$$

The first term is the contribution already contained in the DFT functional in a mean-field way, and the second term is the Hubbard U correction. U_{true} is the true Hubbard U value we want to get. Since the Hubbard U correction would alter the electronic structure of the system, this may in-turn change the quadratic dependence of the DFT functional in the mean-field way. Therefore, U_{true} determined with different U_{in} may vary. If we obtain a value of U_{true}=A at U_{in}=0 and apply the U correction with U_{in}=A, U_{true} may become a different value under this correction. Because of this, U_{true} should be determined at the reference state calculated from the DFT + Hubbard U functional with U_{in}=U_{true} (i.e. internally consistent).

When perturbing the occupation in the linear response procedure, for small shifts in occupation, $a_i^{I,\sigma} = \frac{\delta \lambda_i^{I,\sigma}}{\delta N^{I,\sigma}}$ and $\frac{d^2}{d(N^{I,\sigma})^2} = \sum_{i,j} a_i^{I,\sigma} a_j^{I,\sigma} \frac{d^2}{d\lambda_i^{I,\sigma} d\lambda_j^{I,\sigma}}$. Therefore, the curvature of the DFT + Hubbard U functional, from Eq. A.18, is

$$U_{out} = \frac{d^2 E_{quad}}{d(N^{I,\sigma})^2} = U_{true} - \frac{U_{in}}{m}. \tag{A.19}$$

Here, $m = \frac{1}{\sum_i (a_i^{I,\sigma})^2}$ can be interpreted as an effective degeneracy of the orbitals whose population is changing during the perturbation. In this internally consistent procedure, calculations of U_{out} with a series of U_{in} are carried out and a U_{out} vs U_{in} curve is plotted. At different U_{in}, we get a value of U_{true} from the intercept of the tangent at U_{in} of the curve to the y-axis. The correct U_{true} is the one obtained with U_{in}=U_{true}.

A.4 Effects of the Hubbard U term on the reorganization energy in electron transfer

In this section, we first present the Hubbard U calculation of ferrous and ferric ions in water. Then, we will discuss effects of the Hubbard U correction on the reorganization energy of ferrous-ferric self-exchange reaction.

In the case of ferrous and ferric ions solvated in water, the Hubbard U functional, being a localized functional, is expected to be little affected by the outside water molecules except for those in the first solvation shell. For the same reason, this correction will have little effects on the physical properties beyond the first solvation shell. Therefore, the Hubbard U term would only change the inner sphere contribution (λ_{is}) when the reorganization energy is separated into inner and outer sphere contributions under the same scheme discussed in Section 5.6. In view of this, the Hubbard U values for the simpler systems of hexa-aqua ion clusters are calculated and these values of U are used to obtain to inner sphere contributions to the reorganization energy.

As mentioned in the previous section, the Hubbard U term has to be determined internally consistently. Fig. A-2 shows the U_{out} as a function of U_{in} for the case of ferrous and ferric hexa-aqua ions. In the case of the ferrous ion cluster (upper panel), there is a linear relation between U_{out} and U_{in} and U_{true} can be obtained as the y-intercept of this straight line. It is more complicated for the case of ferric ion cluster (lower panel), U_{true} is clearly dependent on U_{in} as implicated by the non-linearity of the curve. As suggested in the previous section, U_{true} should be evaluated at U_{in}=U_{true}. Therefore, a series of tangents to the curve are drawn and we obtained the y-intercept for each tangent. U_{true} is equal to the value of the y-intercept evaluated with a tangent drawn at U_{in}=U_{true}. With this procedure, we found that U_{true}=5.6 eV also.

With these values of U's, we can obtain λ_{is} following the same procedure in section 5.6. λ_{is}=0.75 eV, as compared to λ_{is}=0.50 eV as in the case of U=0 eV, was obtained when U=5.6 eV. These difference of 0.25 eV can be directly translated to

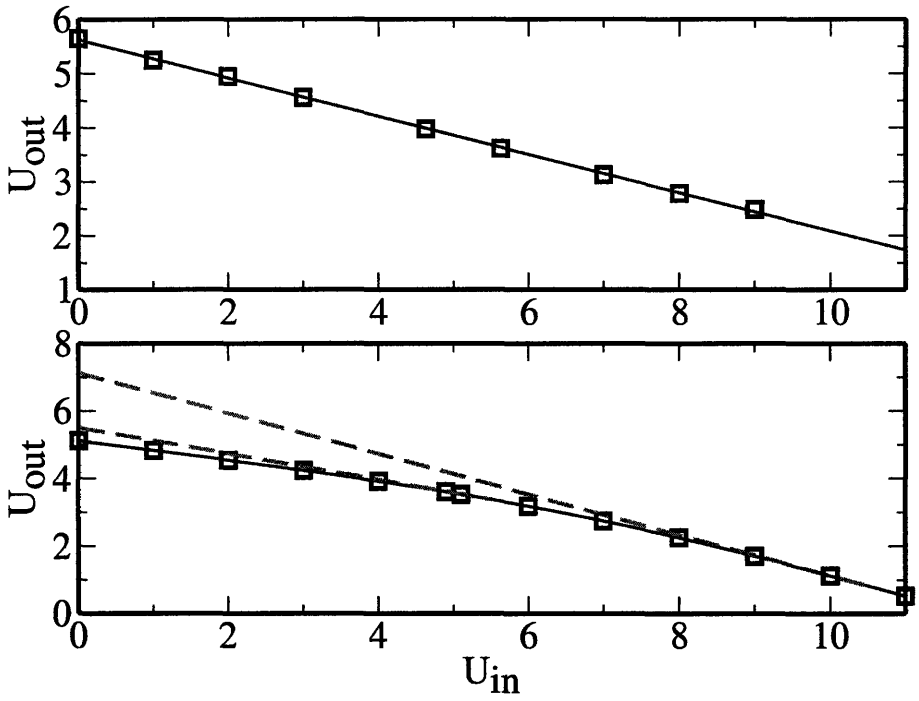

Figure A-2: U_{out} as a function of U_{in} for ferrous and ferric hexa-aqua ion clusters. In the case of ferrous ion cluster (upper panel), U_{out} and U_{in} obey a linear relation and U_{true} can easily be obtained from the y-intercept of the straight line. In the case of ferric ion cluster, a series of tangents were drawn and U_{true} equal the value of the y-intercept evaluated with a tangent drawn at U_{in}=U_{true}.

the total reorganization energy, and for the case when two ions are at 5.5 Å apart, the total reorganization energy, with the Hubbard U correction, is 2.25 eV.

This change in the inner sphere reorganization energy can be understood by the changes in relaxed structures of the clusters with a finite U. Table A.4 shows the six Fe-O distances for hexa-aqua ferrous and ferric ions with U=0 and 5.6 eV. While the optimum structure for $Fe(H_2O)_6^{2+}$ is altered significantly with U=5.6 eV, there are minimal changes in the case of $Fe(H_2O)_6^{3+}$. The larger elongations in d_{Fe-O} in the former case means that a bigger reorganization is required upon a change in oxidation state of the ions, and thus a larger reorganization energy. The elongation of d_{Fe-O} can be explained by the fact that the Hubbard U functional penalizes fractional

Table A.1: The d_{Fe-O}'s of the relaxed structures for hexa-aqua ferrous and ferric ions with U=0 or 5.6 eV.

	U=0 eV	U=5.6 eV
$Fe(H_2O)_6^{2+}$	d_{Fe-O}=2.11 Å 2.11 Å 2.14 Å 2.14 Å 2.14 Å 2.14 Å	d_{Fe-O}=2.15 Å 2.15 Å 2.18 Å 2.18 Å 2.18 Å 2.18 Å
$Fe(H_2O)_6^{3+}$	d_{Fe-O}=2.05 Å 2.05 Å 2.05 Å 2.05 Å 2.05 Å 2.05 Å	d_{Fe-O}=2.06 Å 2.06 Å 2.06 Å 2.06 Å 2.06 Å 2.06 Å

occupations, thus weakening the hybridization between the lone-pair orbitals of water and the empty d-orbitals.

A.5 Implementation of DFT + Hubbard U in Car-Parrinello molecular dynamics

Due to the promising applications of the Hubbard U functional to studying systems with transition metal ions, it will be of wide interest if we could perform finite temperature studies using this Hubbard U functional. In view of this, we implemented the Hubbard U functional in the Car-Parrinello molecular dynamics part of the Quantum-espresso package [61]. We have also performed molecular dynamics simulations of ferrous and ferric ions solvated in water with the Hubbard U functional and we will present the results below.

By including the Hubbard U correction, the new extended Car-Parrinello Lagrangian can be written as,

$$\begin{aligned} \mathcal{L}_{CP} &= \mu \sum_i f_i \int d\mathbf{r} \left|\dot{\Psi}_i(\mathbf{r})\right|^2 + \frac{1}{2}\sum_I M_I \dot{\mathbf{R}}_I^2 - E_{DFT}\left[\{\Psi_i\},\{\mathbf{R}_I\}\right] \\ &- E_U[n^{I,\sigma}_{m,m'}] + \sum_{ij}\Lambda_{ij}\left(\int d\mathbf{r}\Psi_i^*(\mathbf{r})\Psi_j(\mathbf{r}) - \delta_{ij}\right), \end{aligned} \tag{A.20}$$

With the new energy functional, the wavefunctions and the ions evolve according to

the new equations of motion,

$$M_I \ddot{R}_I = -\frac{dE_{DFT}[\{\psi_i\},\{R_I\}]}{dR_I} - \frac{dE_U[n^{I,\sigma}_{m,m'}]}{dR_I} \quad \text{(A.21)}$$

$$\mu_i \ddot{\psi}_i = -\frac{\delta E_{DFT}[\{\psi_i\},\{R_I\}]}{\delta \psi_i^*} - \frac{\delta E_U[n^{I,\sigma}_{m,m'}]}{\delta \psi_i^*} + \sum_j \Lambda_{ij}\psi_j. \quad \text{(A.22)}$$

According to the Hellmann-Feynman theorem, forces on ions can be written as

$$F^I = -\sum_{i,\sigma} \langle \psi_i^\sigma | \frac{d(\hat{H}_{DFT} + \hat{H}_U)}{dR^I} | \psi_i^\sigma \rangle, \quad \text{(A.23)}$$

where $\hat{H}_U$ is the potential due to the Hubbard functional,

$$\hat{H}_U = \frac{U}{2} \sum_{I,m,m'} S(\{R_I\}) |\phi^I_m\rangle (\delta_{m,m'} - 2n^{I,\sigma}_{m,m'} \langle \phi^I_{m'} | S(\{R_I\}). \quad \text{(A.24)}$$

A.5.1 Car-Parrinello molecular dynamics simulations of aqueous ferrous and ferric ions with Hubbard U corrections

We performed molecular dynamics simulations with the Hubbard U corrections both to test the code and to study the effects of this functional on the dynamics. We carried out two separate simulations with either ferrous or ferric ion solvated in 31 water molecules. In Car-Parrinello molecular dynamics simulations, the constant of motion is usually the quantity to look at in order to determine the accuracy of the implementation. The upper panel of Fig. A-3 shows the constant of motion and the potential energy as a function of time of the molecular dynamics simulations production run with aqueous ferrous ion and U=5.6 eV. In these simulations, a fictitious mass (μ) of 450 a.u. and timestep of 2.5 a.u. are used. The temperature is set at 400 K. This simulations was started from an ionic configuration from the end of a 11 ps of aqueous ferrous ion with U=0 eV and the first 1 ps of this simulation is discarded. The constant of motion in Fig. A-3 has negligible fluctuation as compare to the change in the potential energy. The lower left panel in Fig. A-3 shows Fe-O radial distribution function for aqueous ferrous ion in the case with U=0 or 5.6 eV.

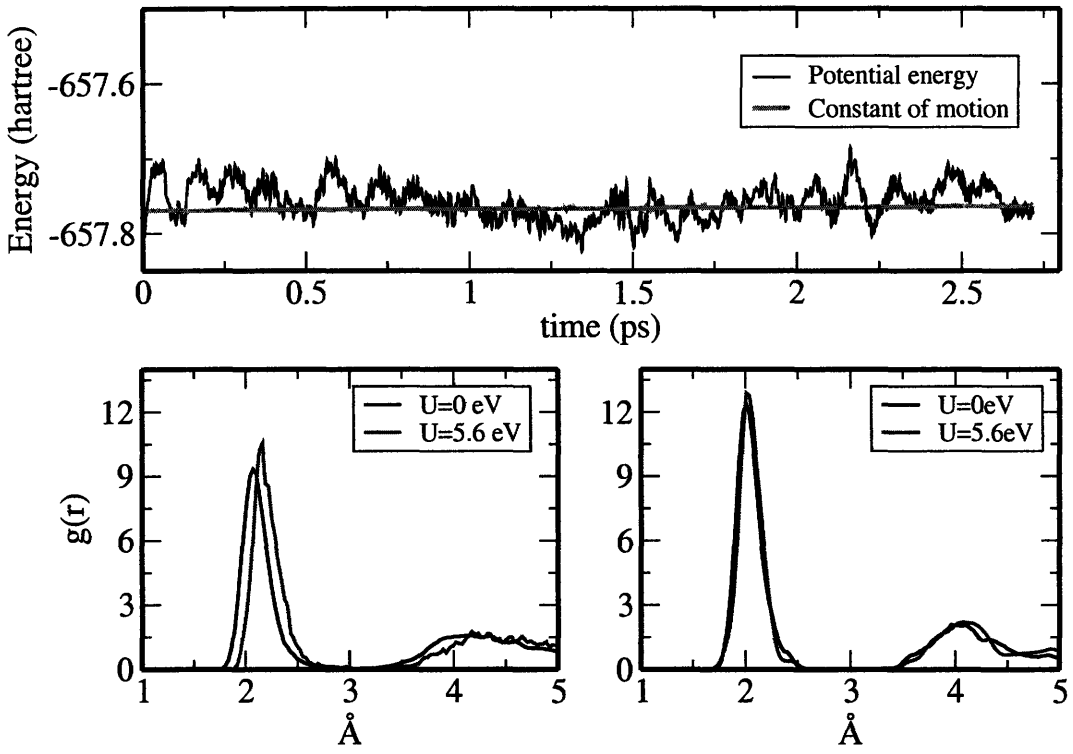

Figure A-3: Upper panel: The potential energy and the constant of motion of the simulation with ferrous ion solvated in 31 water molecules. Lower left: the Fe-O radial distribution functions of aqueous ferrous ion with U=0 and 5.6 eV. Lower right: the Fe-O radial distribution functions of aqueous ferric ion with U=0 and 5.6 eV.

Consistent with the static calculation in Section A.4, the radial distribution function with U=5.6 eV shows the first peak at a large distance. In the case of aqueous ferric ion, there is no significant change in the radial distribution function.

A.6 Conclusion

A DFT + Hubbard U approach describing the strong correlations of transition metal materials is introduced. It has been shown to produce significant improvement from widely used DFT functionals in describing condensed systems with transition metal

ions [145]. Using linear-response calculations [146], we calculated the value of U for hexa-aqua ferrous and ferric ions. With this correction included, it is shown that the reorganization energy is increased by 0.25 eV. Moreover, we have implemented the Hubbard U correction in Car-Parrinello molecular dynamics of the Quantum-Espresso package [61]. Using the simulations with the aqueous iron ions as a test, it is shown that the implementation is working properly. The Fe-O radial distribution functions for ferrous or ferric ions solvated in water are also shown.

Bibliography

[1] A. Nitzan and M. A. Ratner. Electron transport in molecular wire junctions. *Science*, 300:1384-1389, 2003.

[2] R. A. Marcus. On the Theory of Oxidation-Reduction Reactions Involving Electron Transfer. I. *J. Chem. Phys.*, 24:966-978, 1956.

[3] J. M. Sorenson, G. Hura, R. M. Glaeser, and T. Head-Gordon. What can x-ray scattering tell us about the radial distribution functions of water? *J. Chem. Phys.*, 113:9149-9161, 2000.

[4] A. K. Soper. The radial distribution functions of water and ice from 220 to 673 K and at pressures up to 400 MPa *Chem. Phys.*, 258:121137, 2000.

[5] A. Rahman and F. H. Stillinger. Molecular dynamics study of liquid water. *J. Chem. Phys.*, 55:3336-3359, 1971.

[6] W. L. Jorgensen, J. Chandrasekhar, J. D. Madura, R. W. Impey, and M. L. Klein. Comparison of simple potential functions for simulating liquid water. *J. Chem. Phys.*, 79:926-935, 1983.

[7] K. Toukan and A. Rahman. Molecular-dynamics study of atomic motions in water. *Phys. Rev. B*, 31:2643-2648, 1985.

[8] S. W. Rick, S. J. Stuart, and B. J. Berne. Dynamical fluctuating charge force-fields - application to liquid water. *J. Chem. Phys.*, 101:6141-6156, 1994.

[9] G. Lamoureux, A. D. MacKerell, Jr., and B. Roux. A simple polarizable model of water based on classical Drude oscillators. *J. Chem. Phys.*, 119:5185-5197, 2003.

[10] S. Izvekov, M. Parrinello, C. J. Burnham and A. Voth. Effective force fields for condensed phase systems from ab initio molecular dynamics simulation: A new method for force-matching. *J. Chem. Phys.*, 120:10896-10913, 2004.

[11] K. Laasonen, M. Sprik, and M. Parrinello. Ab-initio liquid water. *J. Chem. Phys.*, 99:9080-9098, 1993.

[12] M. Bernasconi, P. L. Silvestrelli, and M. Parrinello. Ab initio infrared absorption study of the hydrogen-bond symmetrization in ice . *Phys. Rev. Lett.*, 81:1235-1238, 1998.

[13] P. L. Silvestrelli and M. Parrinello. Water molecule dipole in the gas and in the liquid phase. *Phys. Rev. Lett.*, 82:3308-3311, 1999.

[14] P. L. Silvestrelli and M. Parrinello. Structural, electronic, and bonding properties of liquid water from first principles. *J. Chem. Phys.*, 111:3572-3580, 1999.

[15] E. Schwegler, G. Galli, and F. Gygi. Water under pressure. *Phys. Rev. Lett.*, 84:2429-2432, 2000.

[16] M. Boero, K. Terakura, T. Ikeshoji, C. C. Liew, and M. Parrinello. Water at supercritical conditions: A first principles study. *J. Chem. Phys.*, 115:2219-2227, 2001.

[17] S. Izvekov and G. A. Voth. Car-Parrinello molecular dynamics simulation of liquid water: New results. *J. Chem. Phys.*, 116:10372-10376, 2002.

[18] I-Feng W. Kuo and C. J. Mundy. An ab initio molecular dynamics study of the aqueous liquid-vapor interface. *Science*, 303:658-660, 2004.

[19] A. Warshel and W. W. Parson. Computer simulations of electron-transfer reactions in solution and in photosynthetic reaction centers. *Annu. Rev. Phys. Chem.*, 42:279-309, 1991.

[20] A. Warshel. Dynamics of reactions in polar solvents. Semiclassical trajectory studies of electron-transfer and proton-transfer reactions. *J. Phys. Chem.*, 86:2218-2224, 1982.

[21] I. Tavernelli, R. Vuilleumier, and M. Sprik. Ab initio molecular dynamics for molecules with variable numbers of electrons. *Phys. Rev. Lett.*, 88:213002, 2002.

[22] J. Blumberger, L. Bernasconi, I. Tavernelli, R. Vuilleumier, and M. Sprik. Electronic structure and solvation of copper and silver ions: A theoretical picture of a model aqueous redox reaction. *J. Am. Chem. Soc.*, 126:3928-3938, 2004.

[23] R. Car and M. Parrinello. Unified Approach for Molecular Dynamics and Density-Functional Theory. *Phys. Rev. Lett.*, 55:2471-2474, 1985.

[24] K. Laasonen, A. Pasquarello, R. Car, C. Lee, and D. Vanderbilt. Car-Parrinello molecular dynamics with Vanderbilt ultrasoft pseudopotentials. *Phys. Rev. B*, 47:10142-10153, 1993.

[25] D. Marx and J. Hutter "Ab-initio Molecular Dynamics: Theory and Implementation", Modern Methods and Algorithms in Quantum Chemistry Forschungzentrum Juelich, NIC Series, vol. 1, 2000. http://www.fz-juelich.de/nic-series/Volume1/marx.pdf

[26] J. Grossman, E. Schwegler, E. Draeger, F. Gygi, and G. Galli. Towards an assessment of the accuracy of density functional theory for first principles simulations of water . *J. Chem. Phys.*, 120:300-311, 2004.

[27] D. Asthagiri, L. R. Pratt, and J. D. Kress. Free energy of liquid water on the basis of quasichemical theory and ab initio molecular dynamics. *Phys. Rev. E*, 68:041505, 2003.

[28] P. H.-L. Sit and N. Marzari. Static and dynamical properties of heavy water at ambient conditions from first-principles molecular dynamics. *J. Chem. Phys.*, 122:204510, 2005.

[29] P. Postorino, R. H. Tromp, M. A. Ricci, A. K. Soper, and G. W. Neilson. The interatomic structure of water at supercritical temperatures. *Nature*, 366:668-670, 1993.

[30] A. Botti, F. Bruni, M. A. Ricci, and A. K. Soper. Neutron diffraction study of high density supercritical water. *J. Chem. Phys.*, 109:3180-3184, 1998.

[31] M. C. Bellissent-Funel, T. Tassaing, H. Zhao, D. Beysens, B. Guillot, and Y. Guissani. The structure of supercritical heavy water as studied by neutron diffraction. *J. Chem. Phys.*, 107:2942-2949, 1997.

[32] T. Tassaing, H. Zhao, D. Beysens, B. Guillot, and Y. Guissani. The partial pair correlation functions of dense supercritical water. *Europhys. Lett.*, 42:265-270, 1998.

[33] Y. E. Gorbaty and Y. N. Demianets. The pair-correlation functions of water at a pressure of 1000 bar in the temperature range 25-500 ^{o}C. *Chem. Phys. Lett.*, 100:450-454, 1983.

[34] Y. E. Gorbaty and A. G. Kalinichev. Hydrogen Bonding in Supercritical Water. 1. Experimental Results. *J. Phys. Chem.*, 99:5336-5340, 1995.

[35] M. Nakahara, N. Matubayasi, C. Wakai, and Y. Tsujino. Structure and dynamics of water: from ambient to supercritical. *J. Mol. Liquids*, 90:75-83, 2001.

[36] R. A. Marcus and N. Sutin, Biochem. Electron transfers in chemistry and biology. *Biophys. Acta*, 881:265-322, 1985.

[37] M. D. Newton and N. Sutin. Electron transfer reactions in condensed phases. *Annu. Rev. Phys. Chem.*, 35:437-480, 1984.

[38] V. I. Anisimov, J. Zaanen, and O. K. Andersen. Band theory and Mott insulators: Hubbard U instead of Stoner I. *Phys. Rev. B*, 44:943954, 1991.

[39] A. I. Liechtenstein, V. I. Anisimov, and J. Zaanen. Density-functional theory and strong interactions: Orbital ordering in Mott-Hubbard insulators. *Phys. Rev. B*, 52:R5467R5470, 1995.

[40] P. Hohenberg and W. Kohn. Inhomogeneous electron gas. *Phys. Rev.*, 136:B864, 1964.

[41] M. Levy. Universal variational functionals of electron densities, first-order density matrices, and natural spin-orbitals and solution of the v-representability problem. *Proc. Natl. Acad. Sci. USA*, 76:6062-6065, 1979.

[42] M. Levy. Electron densities in search of Hamiltonians. *Phys. Rev. A*, 26:1200, (1982).

[43] E. H. Lieb. Density functionals for Coulomb systems. *Int. J. Quantum Chem.*, 24:243, (1983).

[44] W. Kohn and L. J. Sham. Self-consistent equations including exchange and correlation effects. *Phys. Rev. A*, 140:A1133, 1965.

[45] U. van Barth and L. Hedin. A local exchange-correlation potential for the spin polarized case. i *J. Phys. C*, 5:1629-1642, 1972.

[46] D. M. Ceperley and B. J. Alder. Ground-state of the electron-gas by a stochastic method. *Phys. Rev. Lett.*, 45:566-569, 1980.

[47] A. D. Becke. Density-functional exchange-energy approximation with correct asymptotic behavior. *Phys. Rev. A*, 38:3098-3100, 1988.

[48] J. P. Perdew and Y. Wang. Accurate and simple analytic representation of the electron-gas correlation energy. *Phys. Rev. B*, 45:13244-13249, 1992.

[49] C. Lee, W. Yang, and R. G. Parr. Development of the Colle-Salvetti correlation-energy formula into a functional of the electron density. *Phys. Rev. B*, 37:785-789, 1988.

[50] B. Miehlich, A. Savin, H. Stoll, and H. Preuss. Results obtained with the correlation energy density functionals of Becke and Lee, Yang and Parr. *Chem. Phys. Lett.*, 157:200-206, 1989.

[51] J. P. Perdew, K. Burke, and M. Ernzerhof. Generalized Gradient Approximation made simple. *Phys. Rev. Lett.*, 77:3865-3868, 1996.

[52] D. R. Hamann, M. Schlter, and C. Chiang. Norm-conserving pseudopotentials. *Phys. Rev. Lett.*, 43:14941497, 1979.

[53] D. Vanderbilt. Soft self-consistent pseudopotentials in a generalized eigenvalue formalism. *Phys. Rev. B*, 41:7892-7895, 1990.

[54] S. Nose. A molecular-dynamics method for simulations in the canonical ensemble. *Mol. Phys.*, 52:255-268, 1984.

[55] S. Nose. An extension of the canonical ensemble molecular-dynamics methods. *Mol. Phys.*, 57:187-191, 1986.

[56] W. G. Hoover. Canonical dynamics: Equilibrium phase-space distributions. *Phys. Rev. A*, 31:1695-1697, 1985.

[57] W. G. Hoover. Constant-pressure equations of motion. *Phys. Rev. A*, 34:2499-2500, 1986.

[58] *Water: A comprehensive Treatise*, edited by F. Franks (Plenum, New York, 1972) Vol 1.

[59] P. H.-L.Sit, M. Cococcioni, and N. Marzari. Realistic, quantitative descriptions of electron-transfer reactions: diabatic free-energy surfaces from first-principles molecular dynamics. (Submitted to *Phys. Rev. Lett.*)

[60] S. Baroni, P. Giannozzi, and A. Testa. Elastic constants of crystals from linear-response theory. *Phys. Rev. Lett.*, 59:2662-2665, 1987.

[61] S. Baroni, A. Dal Corso, S. de Gironcoli, P. Giannozzi, C. Cavazzoni, G. Ballabio, S. Scandolo, G. Chiarotti, P. Focher, A. Pasquarello, K. Laasonen, A. Trave, R. Car, N. Marzari, A. Kokalj, `http://www.pwscf.org/`.

[62] N. Troullier and J. Martins. Efficient pseudopotentials for plane-wave calculations. *Phys. Rev. B*, 43:1993-2006, 1991.

[63] M. Fuchs and M. Scheffler. Ab initio pseudopotentials for electronic structure calculations of poly-atomic systems using density-functional theory. *Comput. Phys. Commun.*, 119:67-98, 1999. Web site: `http://www.fhi-berlin.mpg.de/th/fhi98md/fhi98PP`.

[64] Web site: `http://www.nest.sns.it/~giannozz`

[65] H.pbe-rrkjus.UPF and O.pbe-rrkjus.UPF from the v1.3 pseudopotential table at `http://www.pwscf.org/pseudo.htm`.

[66] M. Sprik, J. Hutter and M. Parrinello. Ab initio molecular dynamics simulation of liquid water: Comparison three gradient-corrected density functionals. *J. Chem. Phys.*, 105:1142-1152 , 1996.

[67] K. Kuchitsu, Y. Morino. *Bull. Chem. Soc. Jpn.*, 38:805-813, 1965.

[68] T. R. Dyke, K. M. Mack and J. S. Muenter. The structure of water dimer from molecular beam electric resonance spectroscopy. *J. Chem. Phys.*, 66:498-510, 1997.

[69] L. A. Curtiss, D. L. Frurip, and M. J. Blander. Studies of molecular association in H_2O and D_2O vapors by measurement of thermal conductivity. *J. Chem. Phys.*, 71:2703-2711, 1979.

[70] R. M. Bentwood, A. J. Barnes, and W. J. Orville Thomas. Studies of intermolecular interactions by matrix isolation vibrational spectroscopy. *J. Mol. Spectrosc.*, 84:391-404, 1980.

[71] E. Schwegler, J. Grossman, F. Gygi, and G. Galli. Towards an assessment of the accuracy of density functional theory for first principles simulations of water. II. *J. Chem. Phys.*, 121:5400-5409, 2004.

[72] D. J. Wilbur, T. Defries, and J. Jonas. Self-diffusion in compressed liquid heavy water. *J. Chem. Phys.*, 65:1783-1786, 1976.

[73] P. Tangney and S. Scandolo. How well do Car-Parrinello simulations reproduce the Born-Oppenheimer surface? Theory and examples. *J. Chem. Phys.*, 116:14-24, 2002.

[74] The use of norm-conserving pseudopotentials requires a larger plane-wave energy cutoff and thus a larger basis set. A smaller fictitious mass and a small timestep are thus required. For extensive discussion, see the above reference.

[75] W. S. Price, H. Ide, Y. Arata, and O. Söderman. Temperature dependence of the self-diffusion of supercooled heavy water to 244 K. *J. Phys. Chem. B*, 104:5874-5976, 2000.

[76] E. Schwegler, G. Galli, and F. Gygi. Water under pressure. *Phys. Rev. Lett.*, 84:2429-2432, 2000.

[77] M. V. Fernández-Serra and E. Artacho. Network equilibration and first-principles liquid water. *J. Chem. Phys.*, 121:11136-11144, 2004.

[78] A. K. Soper, F. Bruni, and M. A. Ricci. Site-site pair correlation functions of water from 25 to 400 degrees C: Revised analysis of new and old diffraction data. *J. Chem. Phys.*, 106:247-254, 1997.

[79] B. Pullmann, editor. *In Intermolecular Forces.* D. Reidel, Dordrecht, 1981.

[80] J. VandeVondele, F. Mohamed, M. Krack, J. Hutter, M. Sprik, and M. Parrinello. The influence of temperature and density functional models in ab initio molecular dynamics simulation of liquid water. *J. Chem. Phys.*, 122:014515, 2005.

[81] D. Marx and M. Parrinello. Ab-initio path-integral molecular-dynamics. *Z. Phys. B (Rapid Note)*, 95:143-144, 1994.

[82] D. Marx and M. Parrinello. Ab initio path integral molecular dynamics: Basic ideas. *J. Chem. Phys.*, 104:4077-4082, 1996.

[83] M. E. Tuckerman, D. Marx, M. L. Klein, and M. Parrinello. Efficient and general algorithms for path integral Car-Parrinello molecular dynamics. *J. Chem. Phys.*, 104:5579-5588, 1996.

[84] D. Marx, M. E. Tuckerman, J. Hutter, and M. Parrinello. The nature of the hydrated excess proton in water. *Nature*, 397:601-604, 1999.

[85] M. E. Tuckerman, D. Marx, and M. Parrinello. The nature and transport mechanism of hydrated hydroxide ions in aqueous solution. *Nature*, 417:925-929, 2002.

[86] M. Allesch, E. Schwegler, F. Gygi, and G. Galli. A first principles simulation of rigid water. *J. Chem. Phys.*, 120:5192-5198, 2004.

[87] R. A. Kuharski and P. J. Rossky. A quantum-mechanical study of structure in liquid H_2O and D_2O. *J. Chem. Phys.*, 82:5164-5177, 1985.

[88] P. Wernet, D. Nordlund, U. Bergmann, M. Cavalleri, M. Odelius, H. Ogasawara, L. A. Näslund, T. K. Hirsch, L. Ojamäe, P. Glatzel, L. G. M. Pettersson, and A. Nilsson. The structure of the first coordination shell in liquid water. *Science* 304:995-999, 2004.

[89] J. D. Smith, C. D. Cappa, K. R. Wilson, B. M. Messer, R. C. Cohen, and R. J. Saykally. Energetics of hydrogen bond network rearrangements in liquid water. *Science*, 306:851-853, 2004.

[90] A. Nilsson, Ph. Wernet, D. Nordlund, U. Bergmann, M. Cavalleri, M. Odelius, H. Ogasawara, L.-A. Näslund, T. K. Hirsch, L. Ojämae, P. Glatzel, and L. G. M. Pettersson. Comment on "Energetics of hydrogen bond network: Rearrangements in liquid water". *Science*, 308:793, 2005.

[91] J. D. Smith, C. D. Cappa, B. M. Messer, R. C. Cohen, and R. J. Saykally. Response to Comment on "Energetics of Hydrogen Bond Network Rearrangements in Liquid Water" *Science*, 308:793, 2005.

[92] D. Prendergast and G. Galli. The electronic structure of liquid water within density-functional theory. *J. Chem. Phys.*, 123:014501, 2005.

[93] M.J. Cooper *et al.*, editor. *X-Ray Compton Scattering*, Oxford University Press, 2004.

[94] E.D. Isaacs, A. Shukla, P.M. Platzman, D.R. Hamann, B. Barbiellini, and C. Tulk. Covalency of the hydrogen bond in ice: A direct x-ray measurement. *Phys. Rev. Lett.*, 82:600-603, 1999.

[95] B. Barbiellini and A. Shukla. Ab initio calculations of the hydrogen bond. *Phys. Rev. B*, 66:235101 2002.

[96] M. Hakala, S. Huotari, K. Hämäläinen, S. Manninen, Ph. Wernet, A. Nilsson, and L. G. M. Pettersson. Compton profiles for water and mixed water-neon clusters: A measure of coordination. *Phys. Rev. B*, 70:125413, 2004.

[97] M. Hakala, K. Nygard, S. Manninen, L. G. M. Pettersson, and K. Hämäläinen. Intra- and intermolecular effects in the Compton profile of water. *Phys. Rev. B*, 73:035432, 2006.

[98] A. Shukla and C. Bellin. European Synchrotron Radiation Facility, France.

[99] J. S. Schwinger, editor. *Selected Papers on Quantum Electrodynamics*, New York, Dover, 1958.

[100] I. G. Kaplan, B. Barbiellini, and A. Bansil. Compton scattering beyond the impulse approximation. *Phys. Rev. B*, 68:235104, 2003.

[101] A. H. Romero, P. L. Silvestrelli, and M. Parrinello. Compton scattering and the character of the hydrogen bond in ice I-h. *J. Chem Phys.*, 115:115-123, 2001.

[102] G. H. Wannier. The structure of electronic excitation levels in insulating crystals. *Phys. Rev.*, 52:191 1937.

[103] N. Marzari and D. Vanderbilt. Maximally localized generalized Wannier functions for composite energy bands. *Phys. Rev. B*, 56:12847-12865, 1997.

[104] J. P. Rychaert, G. Ciccotti, and H. J. C. Berendsen. Numerical integration of the Cartesian equations of motion of a system with constraints: Molecular dynamics of n-alkanes. *J. Comp. Phys.*, 23:237-341, 1977.

[105] W. J. Lamb, G. A. Hoffman, and J. Jonas . Self-diffusion in compressed supercritical water. *J. Chem. Phys.*, 74:6875-6880, 1981.

[106] K. Yoshida, C. Wakai, N. Matubayasi, and M. Nakahara. A new high-temperature multinuclear-magnetic-resonance probe and the self-diffusion of light and heavy water in sub- and supercritical conditions. *J. Chem. Phys.*, 123:164506, 2005.

[107] A. Shukla and C. Bellin. (*private communications*).

[108] R. L. Blumberg, H. E. Stanley, A. Geiger, and P. Mausbach. Connectivity of hydrogen bonds in liquid water. *J. Chem. Phys.*, 80:5230-5241, 1984.

[109] D. Stauffer. *Introduction to Percolation Theory.* Taylor and Francis, London and Philadelphia, 1985.

[110] A. Kuznetsov and J. Ulstrup. *Electron Transfer Processes in Chemistry and Biology.* John Wiley and Sons, London, 1999.

[111] A. Warshel. Bicycle-pedal model for the first step in the vision process. *Nature*, 260:679, 1976.

[112] A. Warshel and J. Hwang. Simulation of the dynamics of electron-transfer reaction in polar-solvents - semiclassical trajectories and dispersed polaron approaches. *J. Chem. Phys.*, 84:4938-4957, 1986.

[113] G. King and A. Warshel. Investigation of the free-energy functions for electron-transfer reactions. *J. Chem. Phys.*, 93:8682-8692, 1990.

[114] R. A. Kuharski, J. S. Bader, D. Chandler, M. Sprik, M. L. Klein, and R. W. Impey. Molecular-model for aqueous ferrous ferric electron-transfer. *J. Chem. Phys.*, 89:3248-3257, 1988.

[115] K. M. Rosso and J. R. Rustad. Ab initio calculation of homogeneous outer sphere electron transfer rates: Application to $M(OH_2)_6^{(3+/2+)}$ redox couples. *J. Phys. Chem. A*, 104:6718-6725, 2000.

[116] R. A. Marcus. Electrostatic free energy and other properties of states having nonequilibrium polarization. I. *J. Chem. Phys.*, 24:979:989, 1956.

[117] R. A. Marcus. Electron transfer reactions in chemistry. Theory and experiment. *Rev. Mod. Phys.*, 65:599-610, 1993.

[118] A. J. Leggett, S. Chakravarty, A. T. Dorsey, M. P. A. Fisher, A. Garg, and W. Zwerger. Dynamics of the dissipative two-state system. *Rev. Mod. Phys.*, 59:1-85 1987.

[119] B.J. Berne, G. Ciccotti and D.F. Coker, editor. *Classical and Quantum Dynamics in Condensed Phase Simulations*, chapter 1-3, pp 1-66. World Sci, Singapore, 1998.

[120] A. Klimkans and S. Larsson. Reorganization energies in benzene, naphthalene, and anthracene. *Chem. Phys.*, 189:25-31, 1994.

[121] S. F. Nelsen, S. C. Blackstock, and Y. Kim. Estimation of inner shell Marcus terms for amino nitrogen compounds by molecular orbital calculations. *J. Am. Chem. Soc.*, 109:677-682, 1987.

[122] G. J. Herman and G. W. Neilson. Ferrous Fe(II) hydration in a 1 modal heavy water solution of iron chloride. *J. Phys.:Condens. Matter*, 4:649-653, 1992.

[123] G. J. Herman and G. W. Neilson. Ferric Fe(III) coordination in concentrated aqueous electrolyte solutions. *J. Phys.:Condens. Matter*, 4:627-638, 1992.

[124] http://www.physics.rutgers.edu/ dhv/uspp/index.html.

[125] G. Makov and M. C. Payne. Periodic boundary conditions in ab initio calculations. *Phys. Rev. B*, 51:4014-4022, 1995.

[126] J. S. Bader and D. Chandler. Computer simulation of photochemically induced electron transfer. *Chem. Phys. Lett.*, 157:501-504 1989.

[127] J. S. Bader and D. Chandler. Computer simulation study of the mean forces between ferrous and ferric ions in water. *J. Phys. Chem.*, 96:6423-6427, 1992.

[128] We note that GGA+U formulation would require a large, unphysical U of the order of $\sim$ 11 eV to recover qualitatively a localization of charge.

[129] D. A. Scherlis, J.-L. Fattebert, F. Gygi, M. Cococcioni and N. Marzari. A unified electrostatic and cavitation model for first-principles molecular dynamics in solution. *J. Chem. Phys.*, 124:074103, 2006.

[130] P. H.-L. Sit and N. Marzari. Electron-transfer diabatic free energy surfaces from first-principles molecular dynamics. *Bull. Am. Phys. Soc.*, p. 1289, 2005.

[131] M. d'Avezac, M. Calandra, and F. Mauri. Density functional theory description of hole-trapping in SiO2: A self-interaction-corrected approach. *Phys. Rev. B*, 71:205210, 2005.

[132] Q. Wu and T. Van Voorhis. Direct optimization method to study constrained systems within density-functional theory. *Phys. Rev. A*, 72:024502, 2005.

[133] W. Kohn. Density functional and density matrix method scaling linearly with the number of atoms. *Phys. Rev. Lett.*, 76:3168-3171, 1996.

[134] E. Prodan and W. Kohn. Nearsightedness of electronic matter. *Proc. Natl. Acad. Sci. U.S.A.*, 102:11635-11638, 2005.

[135] B. L. Tembe, H. L. Friedman, and M. D. Newton. The theory of the $Fe^{2+}Fe^{3+}$ electron exchange in water *J. Chem. Phys.*, 76:1490-1507, 1982.

[136] A. Fouqueau, S. Mer, M. E. Casida, L. M. L. Daku, A. Hauser, T. Mineva, and F. Neese. Comparison of density functionals for energy and structural differences between the high-[T-5(2g):(t(2g))(4)(e(g))(2)] and low-[(1)A(1g):(t(2g))(6)(e(g))(0)] spin states of the hexaquoferrous cation $[Fe(H_2O)_6]^2+$. *J. Chem. Phys.*, 120:9473-9486, 2004.

[137] D. Harris, G. H. Loew, and A. Komornicki. Structure and relative spin-state energetics of $[Fe(H_2O)_6]^{3+}$: A comparison of UHF, Moller-Plesset, nonlocal DFT, and semiempirical INDO/S calculations. *J. Phys. Chem. A*, 101:3959-3965, 1997.

[138] V. I. Anisimov, editor. *Strong Coulomb Correlations in Electronic Structure Calculations*, Gordon and Breach, New York, 2000.

[139] J. Hubbard. Electron correlation in narrow energy bands. *Proc. Roy. Soc. (London) A*, 276:238, 1963.

[140] A. K. McMahan, R. M. Martin, and S. Satpathy. Calculated effective Hamiltonian for La_2CuO_4 and solution in the impurity Anderson approximation. *Phys. Rev. B*, 38:6650-6666, 1988.

[141] M. S. Hybertsen and M. Schlter. Calculation of Coulomb-interaction parameters for La2CuO4 using a constrained-density-functional approach. *Phys. Rev. B*, 39:9028-9041, 1989.

[142] M. T. Czyyk and G. A. Sawatzky. Local-density functional and on-site correlations: The electronic structure of La_2CuO_4 and $LaCuO_3$. *Phys. Rev. B*, 49:14211-14228, 1994.

[143] I. Solovyev, N. Hamada, and K. Terakura. t_{2g} versus all $3d$ localization in $LaMO_3$ perovskites (M=TiCu): First-principles study. *Phys. Rev. B*, 53:7158-7170, 1996.

[144] H. Sawada, Y. Morikawa, K. Terakura, and N. Hamada. Jahn-Teller distortion and magnetic structures in $LaMnO_3$. *Phys. Rev. B*, 56:12154-12160.

[145] M. Cococcioni, A. Dal Corso, and S. de Gironcoli. Structural, electronic, and magnetic properties of Fe2SiO4 fayalite: Comparison of LDA and GGA results. *Phys. Rev. B*, 67:094106, 2003.

[146] M. Cococcioni and S. de Gironcoli. Linear response approach to the calculation of the effective interaction parameters in the LDA+U method. *Phys. Rev. B*, 71:035105, 2005.

[147] J. Perdew, R. Parr, M. Levy, and J. Balduz, Jr. Density-Functional Theory for Fractional Particle Number: Derivative Discontinuities of the Energy. *Phys. Rev. Lett.*, 49:16911694 1982.

[148] D. C. Langreth and H. Suhl, editor. *Many-body Phenomena at Surfaces.* Academic, New York, 1984.

[149] R. O. Jones and O. Gunnarsson. The density functional formalism, its applications and prospects. *Rev. Mod. Phys.*, 61:689746 1989.

[150] F. Zhou, C. A. Marianetti, M. Cococcioni, D. Morgan, and G. Ceder. Phase separation in Li_xFePO_4 induced by correlation effects. *Phys. Rev. B*, 69:201101, 2004.

[151] F. Zhou, M. Cococcioni, C. A. Marianetti, D. Morgan, and G. Ceder. First-principles prediction of redox potentials in transition-metal compounds with LDA+U. *Phys. Rev. B*, 70:235121, 2004.

[152] H. J. Kulik, M. Cococcioni, D. Scherlis, and N. Marzari. Efficiency and accuracy in transition-metal chemistry: a self-consistent GGA+U approach. (submitted to *Phys. Rev. Lett.*).